Virginia Commonwealth University

VCU Scholars Compass

2021

Single Molecule Investigations of Holliday Junction Binding Protein RuvA

Dalton Reed Gibbs
Virginia Commonwealth University

Single Molecule Investigations of Holliday Junction Binding Protein RuvA

A dissertation submitted in partial fulfillment of the requirements for the degree of Doctor of Philosophy from Virginia Commonwealth University

by

Dalton R. Gibbs

B.S. Chemistry, James Madison University, 2016

PI: Dr. Soma Dhakal

Assistant Professor, Dept. of Chemistry

Virginia Commonwealth University

Richmond, Virginia

March 29th, 2021

Acknowledgments

Here at the end of one long road and at the beginning of another I have a few people I need to thank. Firstly, I should thank my advisor, Dr. Soma Dhakal, without his guidance and support I would not have made it this far. He has many times been more understanding, more helpful, and more kind than he had any need to be. For all this, I owe a large debt of gratitude, thank you for everything.

Secondly, I would like to acknowledge the support and input of my Committee members: Dr. Alvarez, Dr. Cropp, Dr. Tibbetts, and Dr. Reiner. Thank you for your advice and support throughout this process.

Next, I would like to thank the faculty and staff of the Chemistry department. Thanks for little moments of guidance and for your assistance and mentorship. Particularly John Arnold and Dr. Amanda Harris.

Penultimately, I would like to thank the other members of the Dhakal lab for their support and friendship over the years. Specifically, I'd like to call attention to Anisa and Ajona, without whose encouragement this dissertation would be much thinner.

Finally, I'll thank my friends, family, and partner. Mother, I would not be here without you, your support meant so much to me. Thank you to Mamaw and Pampaw for believing in me even when I did not believe in myself. Thanks to A.B., Q.S., M.B., A.W., N.F.A., and Z.L.V.M. for always being there. And thanks to my partner Benjii Maust for supporting me through this process and picking me up when I fall.

Table of Contents

List of Figures

X

List of Tables

Abstract

DNA breaks are inevitable as they mainly occur due to cells' own reactive oxygen species (ROS). While DNA breaks can be single-stranded or double-stranded, the double-stranded DNA (dsDNA) breaks are more dangerous. If such damage is not repaired, it can lead to genetic instability and serious health issues including cancers. One way dsDNA breaks can be repaired is via a process called homologous recombination (HR), which involves several DNA-binding proteins. Therefore, to have a better insight into the repair mechanism and origin of repair defects, we need a better understanding of how these proteins interact with DNA itself and DNA intermediates of the HR process such as Holliday junctions (HJs). The HJ is a four-way branched structure formed between two homologous DNA molecules during exchange of nucleotide sequences, which is a central intermediate of the DNA repair via the HR process. The HJs are eventually resolved into regular dsDNA molecules by a set of proteins called HJ resolvases. Therefore, knowledge of the binding interaction of these proteins and HJ can provide critical insights into the origin of diseases and potential treatments.

Although the HR process has been the subject of intensive study for more than three decades, the complex and dynamic nature of protein–protein and protein–DNA interactions during HR present a significant challenge for determining the molecular mechanism(s) of the process. This knowledge gap is largely because of the dynamic interactions between HR proteins and DNA, which is difficult to capture by routine biochemical or structural biology methods. One remedy for this problem is the employment of single molecule techniques such as single-molecule fluorescence microscopy and optical tweezers. These tools provide unique ways of probing these

complex and dynamic interactions at high spatiotemporal resolution, revealing mechanistic insights of the process. However, for single molecule fluorescence microscopy experiments we needed a single molecule total internal reflection fluorescence microscope which we custom built. Using single-molecule fluorescence resonance energy transfer (smFRET) and ensemble analyses, we recently investigated the binding interaction between the HJ and RuvA – a prokaryotic protein that recognizes the HJ and initiates its resolution by forming a resolvase protein complex called RuvABC. Using the HJ labeled with a donor and acceptor fluorophores to enable smFRET, we show that RuvA stably binds to a specific conformation of the HJ, halting its conformational dynamics. Further, the FRET experiments in different ionic environments created by Mg^{2+} ions suggest that RuvA binds to the HJ via electrostatic interaction. These insights led us to a follow up study looking at the mechanical stability of the RuvA-HJ complex.

We have recently developed an optical tweezers-based single-molecule manipulation assay to detect the formation of protein-HJ complexes, which we implemented to study the RuvA-HJ complex and determined its mechanical and thermodynamic properties in a manner that would be impossible with traditional ensemble techniques. We found that the binding of RuvA increases the unfolding force (F_{unfold}) of the HJ by ~2-fold, demonstrating that the RuvA protein stabilizes the junction. Further, the analysis of *F-X* curves. To our surprise, we also observed that RuvA provides stabilization that permits refolding of the HJ at a force higher than the unfolding force of the HJ without protein. This observation suggests that RuvA stays bound to the DNA construct even after unfolding of the HJ motif, may serve as a nucleation site for HJ refolding, and reduces the energy required for HJ refolding. Together, using high-

resolution single-molecule studies we have revealed several molecular insights of the binding interaction between aforementioned proteins and HJ furthering our understating of their roles in the critical HR process. The better the HR process is understood the more likely the scientific community will be able to develop ways of modulating this process for the treatment of recombination related diseases.

Chapter 1 : Introduction

Homologous Recombination (HR)

DNA damage is inevitable. Within a cell thousands of depurination, deamination, and double stranded DNA (dsDNA) breaks occur each day.[1–3] The dsDNA breaks in particular pose a threat to the genome as they can lead to chromosomal translocation or cell death.[4] In order to preserve the integrity of the genome the cell must have a toolkit in place to deal with these errors. Homologous recombination (HR) is one such repair mechanism, with essential roles in both the repair of dsDNA breaks and genetic exchange.[3,5] This is of particular importance as dsDNA breaks can, if left unrepaired, contribute to genetic defects or cancers.[6] Homologous recombination occurs in three phases: pre-synaptic, synaptic, and post-synaptic.[7] Pre-synaptic HR involves the trimming of the dsDNA to generate single stranded DNA sticky overhangs to allow strand exchange and the creation of the synapse, a four-way DNA junction called the Holliday Junction (HJ). During the synaptic phase genetic information is exchanged through the HJ before moving into the post-synaptic phase in which the HJ is resolved back into dsDNA.[3,8]

In prokaryotes the pre-synaptic process begins with RecBCD reciting the dsDNA and loading of a filament of RecA onto the single stranded piece it has just created.[5] RecA then facilitates strand exchange and the creation of the HJ. Entering the synaptic phase RuvA binds to the HJ and recruits RuvB to act as a motor that can pull the homologous DNA through the RuvA-HJ complex (Figure 1.1). Once this synaptic phase is complete the HJ DNA is resolved back into dsDNA buy RuvC and other enzymes.[5,7,9] The early presynaptic stage of homologous recombination has been well studied, but later synaptic and post-synaptic stages still need further investigation. The HJ is a critical intermediate

of HR and it is in that context of the synaptic phase of homologous recombination that understanding the HJ-binding proteins is critical.
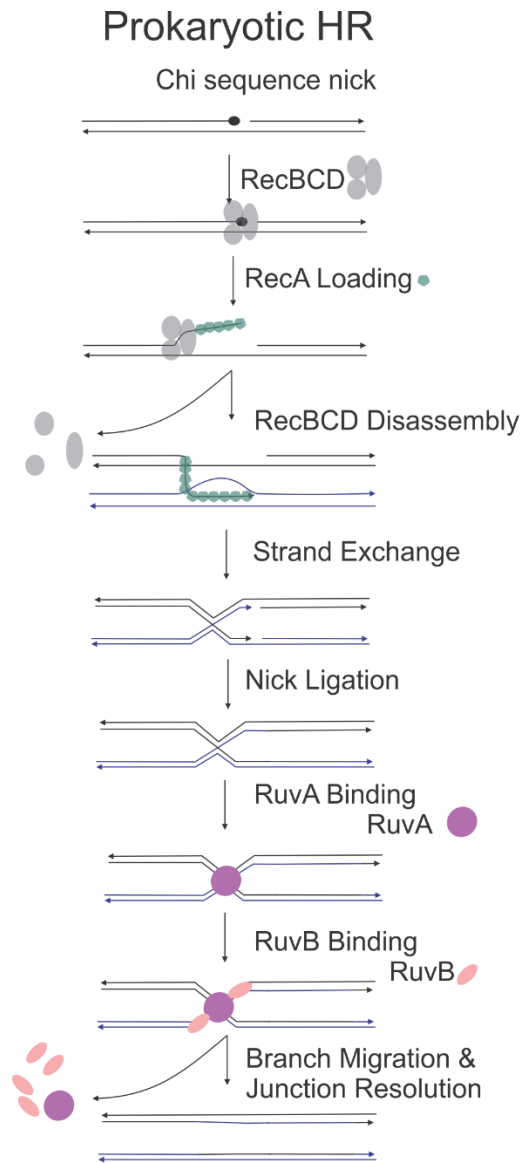
Figure 1.1 Schematic of the stages of prokaryotic homologous recombination.

RuvA Protein

The protein RuvA plays a critical role in the recognition and processing of the HJ in prokaryotes. Without RuvA the processing of homologous DNA and the resolution of the

HJ intermediate would be impaired. Early biochemical studies indicated that RuvA binds preferentially to the HJ[10] and that RuvA serves as the platform that RuvB and RuvC assemble onto to perform their functions.[11,12] Biochemical studies have also revealed that RuvA is a tetrameric protein and that HJ DNA is bound by two such tetramers when undergoing HR.[13] Later crystal structure analyses suggested that the RuvA- HJ complex results in a HJ-bound open cruciform conformation with helix turn helix motifs responsible for binding to the DNA.[14,15] Helix turn helix motifs are common DNA motifs that bind nonspecifically to the major groove of DNA.[16] The RuvA tetramers specificity of the junction is further enhanced by a group of acidic residues that interact with the core nucleotides of the HJ and serve to destabilize the structure of the HJ.[14]

1.3   Single molecule techniques

Single molecule techniques can be powerful tools for teasing out the intricacies of biomolecular interactions.[9] In recent years, fluorescence resonance energy transfer (FRET) and optical tweezers have been heavily used to study biomolecular interactions at the single-molecule level. In FRET techniques a donor-acceptor fluorophore pair with overlapping acceptor excitation and donor emission wavelengths is used. This system when excited with the donor fluorophores excitation wavelength can transfer energy non radiatively to the acceptor fluorophore if the two fluorophores are in close proximity (typically < 10 nm).[17] Therefore, the FRET labeling in conjunction with a prism based total internal reflection fluorescence microscope can be used to study binding interaction between and among biomolecules and it has been employed to study the interaction between RecA and ssDNA[18,19], Rad 51 DNA nucliation[20], Holliday junction binding proteins RuvB[21] and RuvC[22], and other Homologous recombination proteins.

6

Unlike smFRET, optical tweezers is a force based instrument that can measure the forces exerted by single molecules down to picoNewton level. The instrumental details and working principle of optical tweezers have been well established in the literature [23–25]and thus they will not be discussed here. Briefly, this instrument works on the principle of optical trapping, in which highly focused laser light can be used to trap translucent objects. [26] Typically a dual-trap optical tweezers is used for measuring biomolecular interactions. In this case, a biomolecule of interest such as DNA is linked between a pair of trapped particles and force is directly applied to the molecule by keeping one of the laser traps (beads) fixed and moving the second one (bead). The deflection in the laser can be measured as force is exerted on the trapped object and translated into force and this can be used to measure biomechanical systems. Optical tweezers have been used to study Holliday junction branch migration[27] as well as protein folding[28] and other complex biological systems.

Further insight into the RuvABC resolvosome-HJ interaction would come from single molecule techniques. Single molecule techniques would be utilized due to their ability to study individual molecules as they go through biochemical processes. The first studies that evaluated the nature and characteristics of the HJ itself.[29] Before moving onto studies looking at the HJ-RuvABC interaction.[21] These studies utilized single molecule total internal reflectance fluorescence microscopy a technique will be discussed in more detail in Chapter 2. Further research has been done on HJ-RuvABC interactions using optical tweezers, a technique that will be discussed more in Chapter 4.[30,31] This single molecule work served to isolate and observe individual molecules as they were bound to

RuvA, providing insights into the mechanisms of biomolecular processes that more traditional bulk measurements could not.

Chapter 2 : Building a prism-based single molecule fluorescence microscope

Introduction

In this project the microscope layout will be discussed along with on how to assemble the microscope parts and further characterization. Then we will discuss laser alignments, enabling computer control, fluorescence imaging, data processing and safety. With this protocol, we hope to make the instrument assembly simple for future users of prism-based total internal reflection fluorescence (pTIRF) microscopy. Although some objective-type TIRF microscopes are now commercially available, custom-built pTIRF microscopes not only offer a higher signal to noise (S/N) ratio but also allow an easier manipulation and setup of the incident excitation beam(s), providing a greater experimental flexibility and allowing various biophysical studies[32,33]. While the working principle of the pTIRF and single molecule fluorescence resonance energy transfer (smFRET) has been discussed in detail in many publications[34–41], resources and protocols for the assembly of the instrument are very scattered and incomplete. The primary components of this microscope (lasers, optics, inverted microscope, and EMCCD camera, Fig. 2.1) are common in scientific instrumentation. The layout of the instrument is detailed in Figure 2.2 and should be "read" from laser to camera. The instrument is composed of three general sectors: excitation path (Fig. 2.2a); focusing and beam positioning (Fig. 2.2b); and emission path (Fig. 2.2c). We will walk through each of these sections in sufficient detail to explain the logic of component selection, ordering of these parts, assembly, and characterization. All of the microscope parts along with the part description and the quantity needed are compiled in Table 2.1 for a straightforward assembly of the microscope.
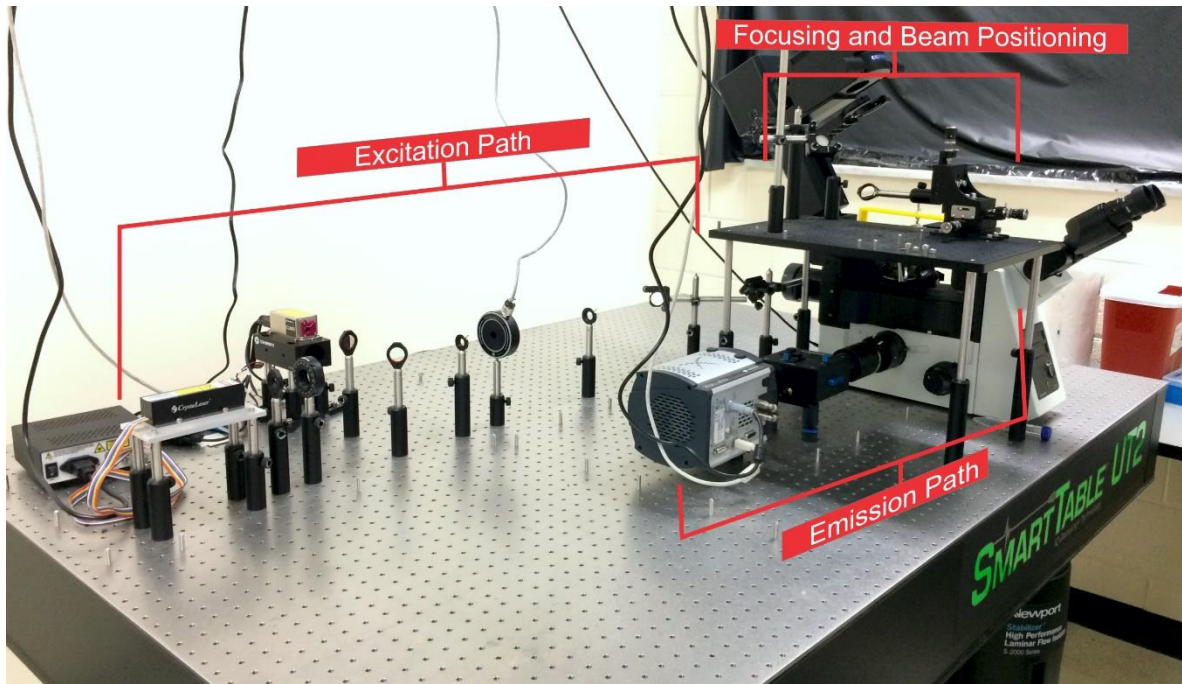
Figure 2.1 Prism-based total internal reflection fluorescence microscope (pTIRF) as it appears on the SMART Table UT2. The excitation path, focusing and beam positioning area, and the emission path are highlighted.
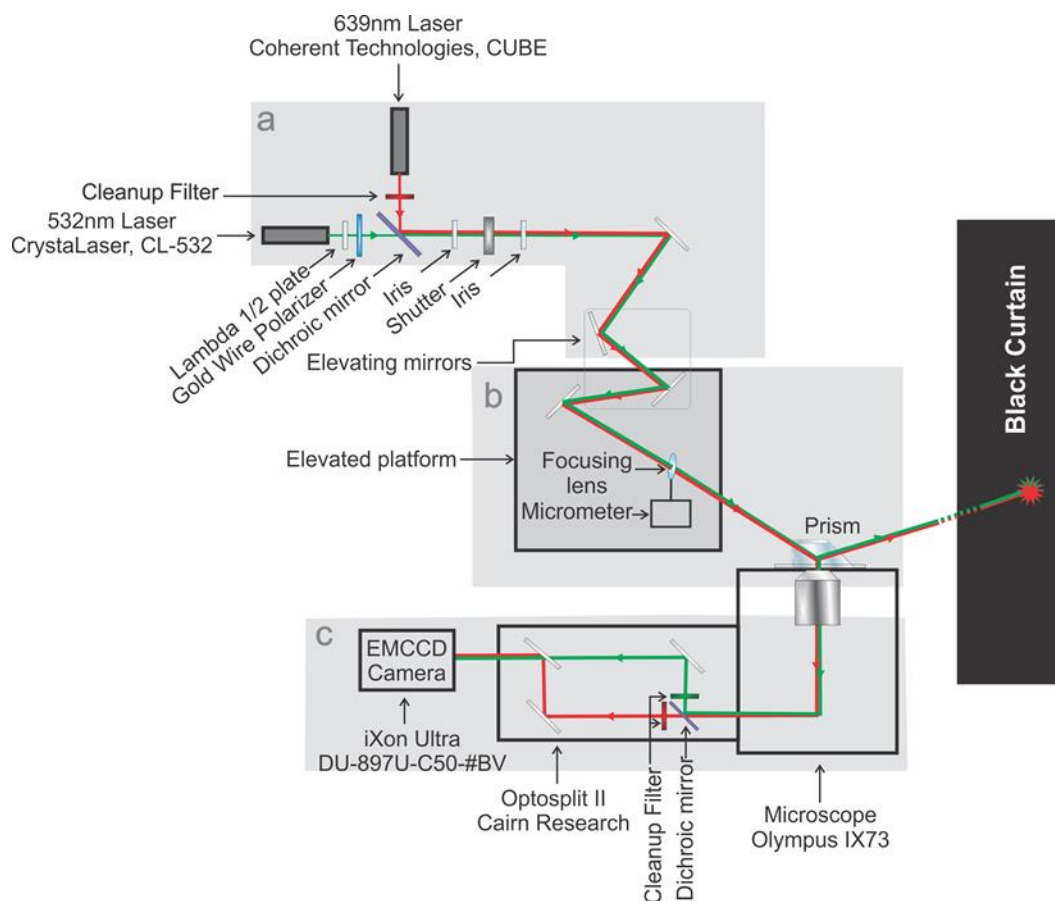
Figure 2.2 Schematic diagram of the pTIRF microscope. The entire setup is split into three parts: (a) the excitation path; (b) the focusing and beam positioning section, containing an elevated section just above the microscope stage; and (c) the emission path. Green and Red lines represent 532 nm and 639 nm lasers.

Excitation light source and filters

The instrument starts at its light sources (typically two of them per user's choice, Figs. 2.2a & 2.3). These lasers serve to excite the fluorophores for later imaging. The first light source is a green (532 nm) laser with a lambda ½ wave plate, which allows for adjustment of polarization when needed[42], and a polarizing filter which serves as a power regulator as this source has no inbuilt power regulation. The second source is a red (639 nm) laser with a cleanup filter to remove any errant light created as a byproduct of laser generation in a range of 630-650 nm (Fig. 2.3). These excitation lasers are mounted 90

degrees to one another with the laser paths directed toward a dichroic mirror that combines the two laser paths by transmitting green and reflecting red wavelengths. This dichroic mirror also serves as a cleanup filter for the green laser as it cuts out light above 565 nm. From this point, the now overlapping laser paths are directed through two irises separated ~30 cm to assist in focusing the instrument. A remotely controlled shutter is placed in the laser path allowing the excitation beam to be shuttered by the operator. The beam then strikes a series of mirrors designed to raise the beam onto an elevated platform. This section serves to generate, cleanup, and co-localize our excitation beam for focusing and beam positioning (Fig. 2.4).
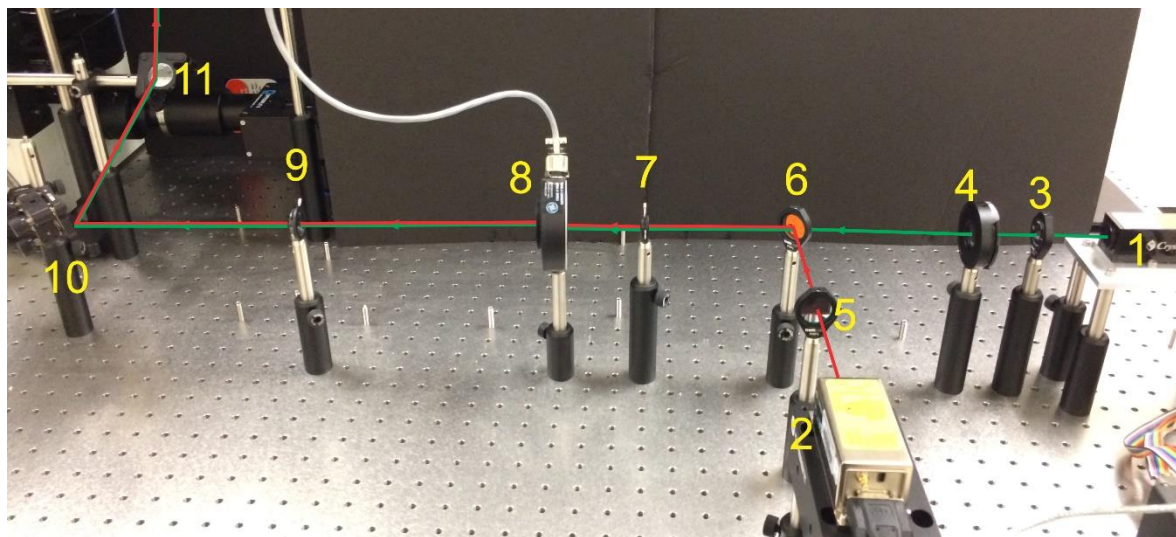
Figure 2.3 Real image of the excitation path of a pTIRF microscope corresponding to the "part a" of Fig. 2. Red and green lines show the path of the lasers. (1-green laser, 2-red laser, 3-half-wave plate, 4-polarizer, 5-clean-up filter, 6-dichroic mirror, 7-iris, 8-shutter, 9-iris, 10-mirror, 11-elevating mirror)

Focusing and beam positioning

In the focusing and beam positioning portion of the instrument (Fig. 2.4a) we follow the beam onto an elevated platform positioned ~3 inches higher than and just to the left of the microscope stage. Mirror #11 in (Fig. 2.3), which is located vertically below mirror

#12 (Fig. 2.4a), is used to reflect the laser beam at 90° to the elevated platform where the final mirror in this section directs the laser through the focusing lens into the prism (Fig. 2.4a). The focusing lens is mounted on a three-axis micrometer, which allows ~1 cm of movement in the x, y, or z directions, thus allowing for fine adjustments to direct the focus of the laser overtop of the objective. A focusing lens with a 200mm focal length (roughly the distance from the mounting point of the lens to the microscope objective) is used to focus the laser more intensely in the usable experimental area. The prism is held in position by a clamp attached to a support arm mounted to the microscope body (see Microscope Assembly section below for detail). This allows total internal reflection of the incident beam, thus producing an evanescent field on the quartz-buffer interface (Fig. 2.4b). It is important to note that a non-fluorescent oil with a refractive index matching that of the quartz slide is used between the prism and the quartz slide.
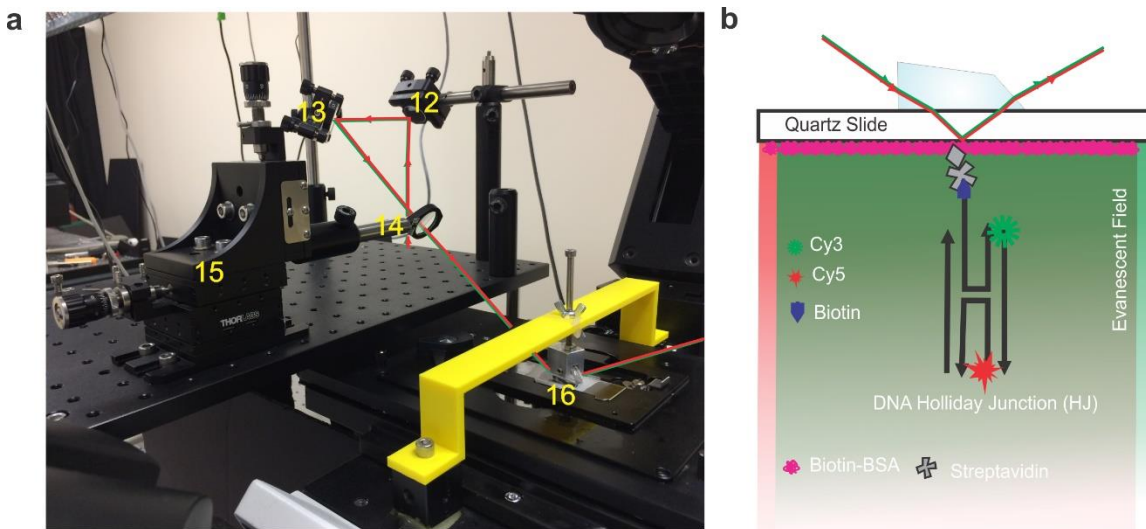
Figure 2.4 (a) Real image of the focusing and beam positioning section of a pTIRF microscope. Red and green lines show the path of the lasers. (12-mirror, 13-mirror, 14-focusing lens, 15-micrometer, 16-prism. The prism is mounted on the clamp that is attached to the prism support-arm (yellow). (b) Schematic of the smFRET setup with DNA Holliday junction (HJ) bound to the surface of a flow cell. An evanescent wave is created

at the quartz/buffer interface by total internal reflection of lasers when passing through the prism (see Technical Notes for detail).

Emission path

The fluorescence emission is captured by an inverted microscope objective (Olympus UPLSAPO 60xW) and directed to the Optosplit-II (commercially available from Cairn) (Fig. 2.5). In the Optosplit-II, the incoming fluorescence emission is separated using a dichroic mirror and a series of mirrors into two beams, one red and one green. These beams are directed through cleanup filters to isolate the light from fluorescent signals and then parallelized and directed into the EMCCD camera[35] where they are fed into a computer for processing (Fig. 2.2c).
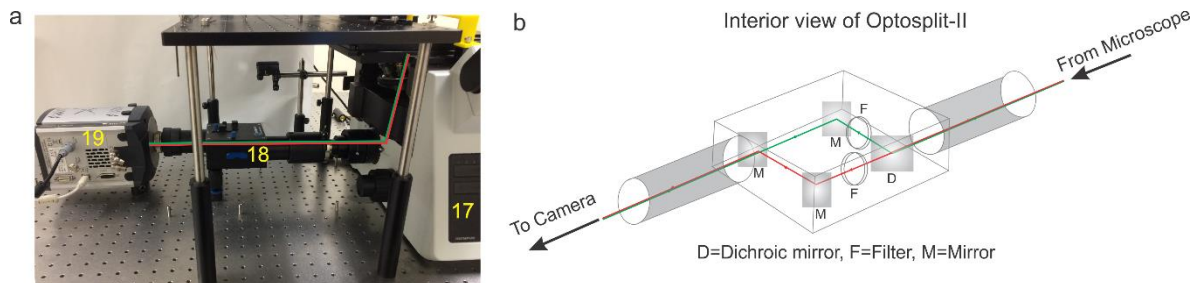
Figure 2.5 (a) Real image of the emission path of a pTIRF microscope. Red and green lines show the path of the lasers (17-Microscope, 18-Optosplit-II, 19-EMCCD Camera). (b) Diagram of Optosplit-II detailing the path of the light coming from the microscope and directed through a dichroic mirror (D), set of filters (F) and a series of mirrors (M) that serve to separate green and red emissions and parallelize the light to allow two color channels to be recorded on one EMCCD camera.

Space Design

Space considerations are necessary before setting up a pTIRF system. It is recommended that a 6 x 4 feet space with easy access to electric outlets should be blocked off for positioning of the vibration isolation table, such as the 1200 x 1800 x 203 mm tune damper UT2 smart table from the Newport company, leaving at least a 2 feet gap along the perimeter for easy clearance access all around the table. A metal rack with

14

installed electrical outlets built and suspended from the ceiling roughly 6 ft above the floor is ideal to provide space for power supplies. Alternatively, a wall- mounted shelf or small table under the isolation table would also suffice. On the table, the microscope alone will take up about 19 x 22 inches of space on the breadboard, leaving the rest for positioning of the optics and camera. Extra space in close proximity to the laser table should be designated for a computer table with room for the PC, monitor, keyboard, and mouse. Ideally the computer table should be situated near the eyepiece of the microscope for ease of operation. Some amount of bench space may also be necessary for sample preparation and storage of materials. Two 5 x 2 feet tables, one designated for the computer set up and the other for extra bench space can provide sufficient room for extra work space. The dimensions we suggest leave ample room for additional optics to be added as necessary for future experiments. However, it should be noted that it is certainly possible to condense the pTIRF microscope set up to a 4 x 3 feet vibration isolation table. Even a greater area can be conserved if creative optics solutions are utilized (e.g. fiberoptic runs).

Safety considerations must be taken while planning a space for the microscope. The microscope area must be completely enclosed to avoid any laser hazard and the stray room-light from reaching the camera during fluorescence measurements. Any open space such as windows or doorways should be blocked off using a black laser curtain to avoid accidental injury from scattered or reflected laser light. While in use, a "Laser in Use" sign is recommended to make anyone outside of the laser area aware to take necessary precautions before entering the area. While in the area, laser safety goggles should always be worn by all personnel (see Safety Considerations Section below).

Table 2.1. Extensive list of microscope parts along with the catalog numbers, parts descriptions and the vendors from which we bought the parts to build our microscope. The numbers in the rightmost column correspond to the optics numbering used in Figures 2.3-2.5.

Catalog/Item#	Item Description	Quantity	Vendor	Optics #
p/n 325-1206	p/n 325-1206 UV FS Pellin-Broca Prism 11x20x6.4 mm	2	Altos Photonics, Inc.	16
	Laser Barrier 150" wide X 92" long	1	Beamstop'r	
16212	Immersion Oil Type FF (4 Fl. Oz.)	2	Cargille	
zet640/20x	magnetron bandpass clean-up filter (excitation path), 0-5 deg aoi	1	Chroma Technology Corp	5
t565spxxr-uf3	magnetron shortpass dichroic, 45 deg aoi	1	Chroma Technology Corp	6
1069417	SYS: CUBE 640-40 CIRCULAR: 640nm: 40mW	1	Coherent Inc.	2
1073840	ASSY: HEAT SINK: ACCESSORY: CUBE	1	Coherent Inc.	
1214333	Productivity Plus Bronze - CUBE	3	Coherent Inc.	
EW-06419-01	Tygon Microbore Autoanalysis Tubing, 0.020" x 0.060"OD, 100 ft/roll	4	Cole-Parmer	
CL532-050-L	532nm Central Wavelength 50mW CW Power	1	CyrstaLaser	1
4001	Hardman DOUBLE/BUBBLE Extra-Fast Set Epoxy Red Package 3.5 g Packet	3	Ellsworth Adhesive Systems	
KBH-5503	Laser Protective Eyewear for HeNe Alignment and KTP Alignment applications	2	Kentek Corporation	
9470	15ft USB 3.0 A Male to A Female Active Extension Cable	2	Monoprice	
5010	Cat6 24AWG UTP Ethernet Network Patch Cable, 20ft Gray	2	Monoprice	
2067	USB to RS232 DB9 male(Serial) / DB25 male Converter Cable	1	Monoprice	
U-R380	IX3-D6RES;6-POSITION IX NOSEPIECE CODED,DIC	1	Olympus America Inc.	
U-V111C	U-TV1XC;C-MOUNT CAMERA ADAPTER, CENTERABLE	1	Olympus America Inc.	
9-U734	45FR; 45MM FROSTED DIFFUSION FILTER, IX3	1	Olympus America Inc.	
UYCP-11	UYCP-11;US STYLE 3-PRONG POWER CORD	1	Olympus America Inc.	
5-UR403	IX3-RFA;STRAIGHT ILLUMINATOR	1	Olympus America Inc.	17
5-UR416-1	IX3-RFACS-1-2; CODED IX3FLUORESCENCE TURRET	1	Olympus America Inc.	17
OCT-TD7BX3	TRF59907-OL3; Dual-band ET-532/640nm laser TIRF set	1	Olympus America Inc.	
OAT-DU-897U-CS0-#BV	DU-897U-CS0-#BV;IXON ULTRA897 EMCCD, 56FPS,512X512,16 UM,USB	1	Olympus America Inc.	19
OAT-TR-EMFS-F06	532/640 EM SPLITTING 3 PART FILTER SET FOR DPC&OPTOSPLIT	1	Olympus America Inc.	
OAT-TR-DCIS-CA1-00	DUAL CAM CASSETTE. REQ(TR-EMF S-F)	1	Olympus America Inc.	

O89-OptoIILS	OptoSplit II LS–1.0x; Optosplit II system w/cubes and diaphragm	1	Olympus America Inc.	18
OMT-010	MT-010;LOGO CLOTH DUSTCOVER 11X25X26", ANTI-STATIC BX, IX	1	Olympus America Inc.	
OVP-MSTUT2468	M-ST-UT2-46-8; Tuned-Damped Table, 1200x1800x203mm, M6 Holes	1	Olympus America Inc.	
OVP-S2000A428	S-2000A-428; 28" Isolators w/Auto Leveling, Set of 4	1	Olympus America Inc.	
OVP-ACWS	ACWS; Air Compressor, Low Noise, 110V	1	Olympus America Inc.	
HPZ440WIN7-2	2805181;HP Z440,2X1TBHD,RAID1,32GB DDR3,WIN764,SERIAL,MS OFC	1	Olympus America Inc.	
D-M27FPW2	718668226; 27-INCH 16:9 RATIO FLAT PANEL,4K UHD, HDMI,D PORT	1	Olympus America Inc.	
DIB-551.00	Diamond Coated "Stick" Drills, DIB-551.00	10	Shor International	
TR6-P5	Ø1/2" Optical Post, SS, 8-32 Setscrew, 1/4"-20 Tap, L = 6", 5 Pack	3	Thorlabs, Inc.	
MB1218	Aluminum Breadboard 12" x 18" x 1/2", 1/4"-20 Taps	1	Thorlabs, Inc.	
SH8S050	8-32 Stainless Steel Cap Screw, 1/2" Long	1	Thorlabs, Inc.	
TR12	Ø1/2" Optical Post, SS, 8-32 Setscrew, 1/4"-20 Tap, L = 12"	6	Thorlabs, Inc.	
SH25S038	1/4"-20 Stainless Steel Cap Screw, 3/8" Long	1	Thorlabs, Inc.	
RA90	Right-Angle Clamp for Ø1/2" Posts, 3/16" Hex	8	Thorlabs, Inc.	
TR6	Ø1/2" Optical Post, SS, 8-32 Setscrew, 1/4"-20 Tap, L = 6"	1	Thorlabs, Inc.	
TR075	Ø1/2" Optical Post, SS, 8-32 Setscrew, 1/4"-20 Tap, L = 0.75"	2	Thorlabs, Inc.	
SS25S075	1/4"-20 Stainless Steel Setscrew, 3/4" Long, Pack of 25	1	Thorlabs, Inc.	
SH25S075	1/4"-20 Stainless Steel Cap Screw, 3/4" Long, Pack of 25	1	Thorlabs, Inc.	
B3648F	36" x 48" x 2.4" Imperial Breadboard, 128 x 98 x 23 cm	1	Thorlabs, Inc.	
PSY313	900 x 1200mm Full Under Shelf, 146 x 95 x 6 cm	1	Thorlabs, Inc.	
PTA512	Air Compressor - 110/115 V - 60 Hz, US Power Plug, 45 x 38 x 46 cm	1	Thorlabs, Inc.	
RSP1	Rotation Stage For 1" Optics 2.2"OD 1.062-20 ID	1	Thorlabs, Inc.	
TR3-P5	1/2" Dia . x 3" Length: Pack of 5 Post	3	Thorlabs, Inc.	
SS6MS25	M6-1.0 X 25mm Set Screw, 25 Pack	2	Thorlabs, Inc.	
SS6MS12	M6 X 1.0 Stainless Steel Set Screw 12mm Long Pack of (25)	1	Thorlabs, Inc.	
FMP1-P5	Fixed Ø1" Optical Mount 5-Pack	2	Thorlabs, Inc.	
WP25M-VIS	Mounted Ø25.0 mm Wire Grid Polarizer, 420-700 nM	1	Thorlabs, Inc.	4
ID8	Mounted Standard Iris, 8.0.mm max. Aper.	1	Thorlabs, Inc.	7
ID12	Iris Diaphragm 1/2"	1	Thorlabs, Inc.	
ID15	Mounted Standard Iris, 15.0.mm max. Aper.	1	Thorlabs, Inc.	9
WPMH05M-532	Mounted Multi Order 1/2 Waveplate 532nm	1	Thorlabs, Inc.	3

BB1-E02	Ø25.4mm Mirror, Broadband 400-750nm	4	Thorlabs, Inc.	10-13
LB1904-A-ML	Mounted N-BK7 Bi-Convex Lens, Ø1" , f = 125mm, -A	1	Thorlabs, Inc.	
LB1437-A-ML	Mounted N-BK7 Bi-Convex Lens, Ø1" , f = 150mm, -A	1	Thorlabs, Inc.	
LB1945-A-ML	Mounted N-BK7 Bi-Convex Lens, Ø1" , f = 200mm, -A	1	Thorlabs, Inc.	14
ESK01	MOUNTING SUPPORTS ESSENTIALS KIT #1	1	Thorlabs, Inc.	
LG1	Laser Glasses, 190-400nm, 808-1090nm	1	Thorlabs, Inc.	
ADB-10	Pellin Broca Prism 10 mm BK7	1	Thorlabs, Inc.	16
MT3A/M	XYZ Metric Translator Stage	1	Thorlabs, Inc.	15
KS1	Lockable Kinematic 1" Optic Mount	4	Thorlabs, Inc.	
SDA90120S	Standing Height Active Science Desk to suit 900x1200mm	1	Thorlabs, Inc.	
LS6S2T0	Uni-stabled housed Shutter	1	Vincent Associates	8
VCM-D1	Shutter Driver	1	Vincent Associates	

2.3 Safety Considerations

It is very important to enclose the laser area to avoid safety hazards and keep everyone safe, thus it is necessary to:

- Block the surroundings using black laser curtains.

- Use the sign 'laser in use' to warn outsiders so that they may take necessary precautions before entering the area.

- Wear the appropriate laser safety goggles when using the laser and entering the laser area.

- Keep the shutter closed when the laser source is not required.

- Never look directly into the light path when the shutter is open.

Microscope assembly

Optics Installation

1. Assemble optics on the laser table in a straight line along a single plane as specified
[2.4] in the instrument optical diagram.

CRITICAL STEP Later steps will require that the lasers are aligned such that the beams are traveling co-linear. Ensuring that the lasers, emitters, and optics are mounted level with one another can prevent headaches down the line.

2. Build the elevated platform 90° to the end of the optical path next to the area intended for the microscope.

3. The lasers must be adjusted so that both beams pass through both irises. The iris closest to the laser is first narrowed, taking care not to close the iris completely, and the lasers readjusted so that both beams pass through its center. This step is then repeated with the second iris which is narrowed and the lasers adjusted so that the beams now pass through the center of both irises.[43]

Note: This process may take several repeated steps of narrowing one or both irises and adjusting the lasers to achieve total centering of the beams. Fine tuning of the leveling can be accomplished by allowing the lasers to leave the laser table and making minute adjustments to ensure that the points cast by both lasers hit at the same point on a wall. From this point onwards, the optics should not be adjusted unless something comes out of alignment.

4. Position the first mirror to direct the beam toward the elevated platform. The next two mirrors are placed in the line of the laser at roughly 45 degrees relative to the plane of

the table and used to guide the beam toward the elevated stage and lift it to a level above the micrometer. The final mirror is used to direct the laser path through the focusing lens with 200 mm focal length (mounted on the micrometer) and into the prism, all adjusted so that the laser path enters into the prism at the appropriate angle to induce total internal reflection (in the case of our setup ~35°, calculated according to method detailed below in the Technical Note section).

CRITICAL STEP It will be necessary to adjust the mirrors such that the focus is not elongated.

5. The microscope should be situated to the right of the elevated platform in such a way that the laser can be aimed through the optics and still maintain both the angle of total internal reflection and be within the focusing distance of the focusing lens.

6. The prism should be mounted in place over the flow cell by a clamping device affixed to the support arm which is screwed onto mounting hardware fixed to the upper body of the microscope.

Note: Our prism clamp and support arm were custom manufactured by machining of aluminum and 3D printing respectively (see Technical Note section below for details). For a given microscope, the dimensions of the support arm and relative height of the prism will change, however the central principle of the design remains the same: to fix the position of the prism directly over the objective. So long as this is accomplished the design can be modified in many ways to accommodate various microscope brands and configurations.

7. Install the Optosplit-II (Carin Research, UK) into the imaging port and install the dichroic mirror and filters cube into the Optosplit-II. The aperture of the optosplit can then be tuned using the aperture adjustors to size the incoming light down to fit onto half of the EMCCD camera's field of view and adjusted to split the channels to show parallel images (see Figs 2.5 and 2.6). This can be accomplished by using a slide with some mm sized details (such as etched writing) to align the two channels in a parallel fashion for analysis by some smFRET program.

Note: The Optosplit-II manual contains a more in-depth description of this process.

8. Install Single.exe, a program that is made available by the TJ Ha group designed to record single molecule fluorescence data (see Data Acquisition and Analysis section below. Instructions on how to configure the EMCCD camera can be found in the Single.exe reference manual but can be summarized as finding the appropriate "atmcd32d.dll" file for the selected camera model and overwriting the existing file in the Single.exe program directory. This .dll can be found in the driver install software package that accompanies Andor camera's (https://cplc.illinois.edu/software/).

Note: In all cases we used a x64 Windows PC to run this software. OSX or Linux versions may not be compatible/available for all mentioned software.

9. OPTIONAL STEP Set up computer control of one or both lasers. In our case, we used a 639 nm Coherent CUBE Diode Laser (part#1069417) which comes equipped for computer control with an accompanying computer program Coherent Connection (http://cohrdownloads.blob.core.windows.net/file/CUBE%20Connection.zip). This laser's

serial cable connection was routed to our modern computer using a serial to USB connector.

Note: When connecting an item to the processing computer with a serial cable, some configuration may be necessary to ensure that the coherent connection is monitoring the same serial port that the USB adaptor is feeding to.
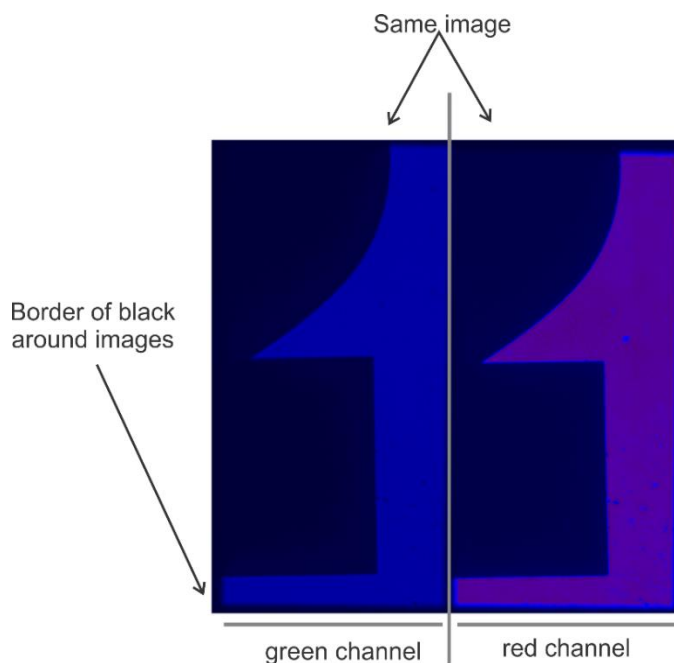
Figure 2.6 Image of a properly adjusted optosplit. Image of silkscreen printed "2" on a glass slide was captured using the program called Single.exe (see Data Acquisition section for details). Note that if one uses Single.exe to acquire smFRET data, the green channel must be on the left and the red channel on the right. For proper alignments of the channels, the image size is adjusted to take up approximately half of the available space and that the images are well separated with a black border running around and between them.

Laser alignment and focusing

The alignment process, as outlined in the microscope assembly section, should roughly focus the laser onto the flow cell through the prism, but the largest portion of the laser alignment is the fine tuning.

22

1. The first step in fine-tuning the laser alignment is to ensure that the laser lands immediately over the microscope objective. This can be aided by using a small piece of Scotch magic tape (preferably white in color) affixed on a glass slide to more easily visualize the location of the focus.

CRITICAL STEP. It is essential to get the beam as close to the center of the objective lenses as possible as this will save time in adjusting the micrometer later on.

2. A flow cell filled with water should be placed onto the microscope, a drop of immersion oil should be placed on the top surface of the flow cell and the prism support arm assembly screwed into place.

Note: It is important that the flow cell be assembled using a quartz slide as using glass will result in an unusable background signal.

3. The micrometers should be used to adjust the position of the focus on the X and Y-axis until it is centered in the field of view through the eyepiece in the lowest objective. Once done, the Single.exe program can be used to track the intensity of the light coming off the focus.

4. The Z-axis is then adjusted either up or down to increase the intensity of the light, during which some X and Y adjustment needs to take place to keep the focus at the center of the field of view. This Z axis adjustment should be carried out until the intensity of the signal reaching the camera is at its maximum.

Note: The center of the microscope field of view may be offset from the cameras field of view, so adjustments should be made accordingly.

Flow cell design and construction for pTIRF experiments

Cleaning procedure

2.5 The cleaning procedure was followed from a published protocol. [44]

1. Briefly, wash the slides in warm soapy water and then scrub thoroughly with a thick paste of Alconox, follow by rinsing the slides in deionized water, acetone and ethanol successively.

2. Then flame the slides for 30 seconds on each side using a propane torch and immediately transfer them to a boiling base-piranha bath (Solution of 4% hydrogen peroxide and ammonia) for about 15 minutes and flame again on each side for 30 seconds with propane torch.

Design the flow cell

1. Take a pre-cleaned standard quartz slide (75 × 26 × 1 mm) with two diagonally drilled holes (drilled using a diamond-coated drill bit (1 mm in diameter) in a Dremel multitool purchased from Walmart) and add parafilm overtop.

2. Create a sample chamber by cutting the parafilm diagonally to encompass the drilled holes.

3. Cover the sample chamber with a glass coverslip (24 x 60 mm, Fisher Scientific) and heat the whole assembly to 120˚C for 5 min on a hot plate in order to melt the parafilm, thus sealing the glass coverslip to the microscope slide.

4. Cut two 200 µL plastic pipette tips to about an inch long, insert into the holes and plume

with tubing (0.02 in. ID, 0.06 in. OD, Cole-Palmer) using Double Bubble Quick-Set epoxy

from Hardman Adhesives.

Note: The physical obstructions of the pluming in this flow cell design limit the usable

space for the experiment to ~1/5 of the slides total surface area.
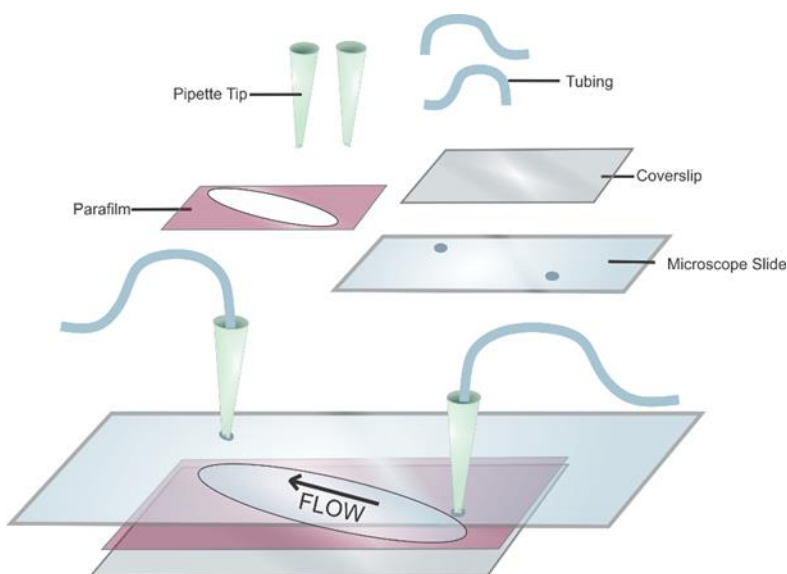
Figure 2.7 Schematic of a flow cell. The quartz microscope slide is shown with pipet tips
and tubing to allow for buffer exchange. The sample chamber consists of a parafilm
sandwiched between a microscope slide and the glass coverslip. The arrow shows the
direction of the buffer flow.

Surface-functionalization of flow cell

1. Functionalize the flow cell by sequential incubation of 1 mg/mL biotinylated BSA and

0.2 mg/mL streptavidin for 5 min and 2 min, respectively. [45]

2. Then flush the flow cell with ~300 µL of 1×TAE-Mg buffer (40mM tris, 2mM EDTA,

20mM acetic acid, 12mM MgCl$_2$).

Validation of the pTIRF setup via typical smFRET experiment

Typical smFRET data were gathered from monitoring the dynamics of the Holliday junction (HJ)[44,46–48]. The HJ is a central part of the double stranded DNA break repair mechanism and as such, its resolution has been seen as a possible target for drug therapy[3,8,49–56]. FRET data can be analyzed and interpreted in various ways[57–60], we used a simple efficiency analysis (equation 2.1).   The Holliday junction is a four way DNA junction formed from 4 single-strand DNA (ssDNA). Inherent to this structure is the tendency to switch between two stacked conformation, called herein Iso-I and Iso-II (Fig. 2.8) [29,48]. The frequency of this structural switching is dependent on the concentration of a divalent cation such as magnesium ion in the solution. For this experiment a biotinBSA/streptavidin-functionalized flow cell is treated with a biotin-functionalized, dual fluorophore labeled HJ as described in our previous work[61]. Briefly, the HJs were immersed in an imaging buffer (300 mM Mg^{2+}, 40 mM Tris, 10 mM acetic acid, 1 mM EDTA, 10mM PCA, 50 nM PCD, and 5mM Trolox), injected into the flow cell, incubated for surface immobilization, and movies were recorded by Single.exe at a 50 ms frame rate while the green laser (532 nm) is on. The PCA, PCD and Trolox make an oxygen scavenging system (OSS) which is necessary to retard photobleaching of the fluorophores[62–65]. Typical intensity-time traces of dynamic HJ switching between iso-I and iso-II are depicted in Figure 8, showing the anti-correlation of the red and green signals typical of a FRET pair switching between a short to longer distance from one another. This is also reflected in the FRET trace calculated using equation 1 [62,66,67].

$$FRET\ Efficiency\ (E_{FRET}) = \frac{I_{\text{acceptor}}}{I_{donor} + I_{\text{acceptor}}} \qquad (eqn\ 2.1)$$

Where FRET efficiency is calculated using the intensities of the donor (Idonor) and acceptor (Iacceptor) fluorophores. In this experiment the donor is Cy3 and the acceptor is Cy5.
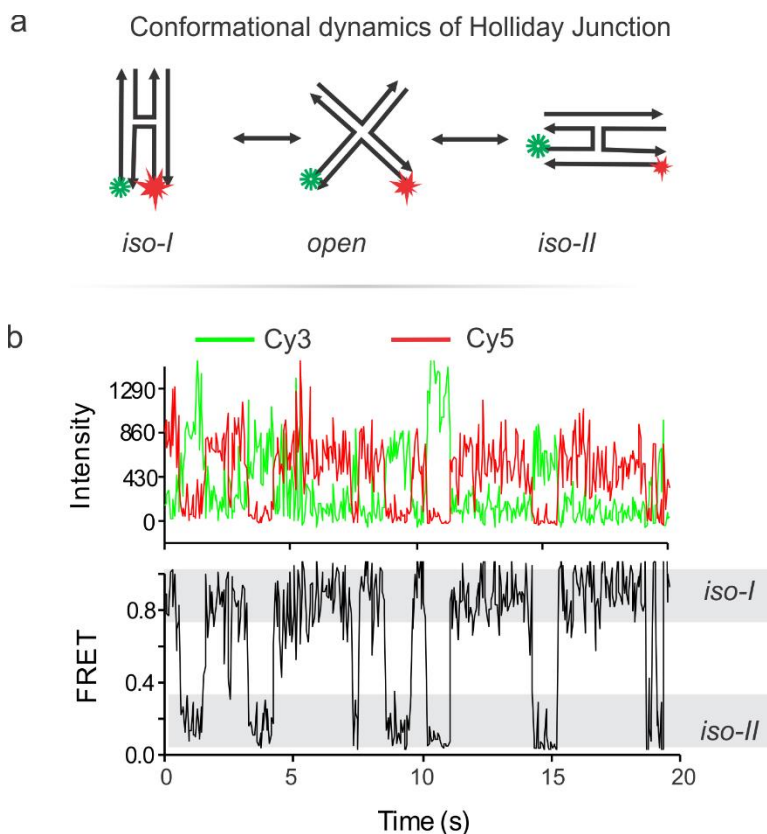
Figure 2.8 Characterization of the instrument with a typical experiment. (a) Conformational switching of the synthetic Holliday junction (HJ) labeled with a Cy3-Cy5 fluorophore pair. (b) Representative single molecule fluorescence-time traces from our smFRET experiment on the HJ. Note that the junction switches between the Iso-I and Iso-II conformations. Adapted with permission from Ref 46. Copyright 2018 American Chemical Society.

Data Acquisition and Analysis

Data acquisition and analysis codes were readily available for smFRET data and were acquired upon request from the Center for the Physics of Living Cells (https://cplc.illinois.edu/software/). This package contains the data acquisition application, Single.exe which records fluorescence signal acquired by the EMCCD for

each movie as a .pma file. The package also includes custom written scripts for IDL and MATLAB which can be used to generate and process single molecule FRET traces from acquired .pma files. The MATLAB and IDL programs are commercially available. The IDL program scripts pair molecules exhibiting fluorescence from the donor and acceptor channels and track their intensities over time. These traces can be viewed in a user friendly manner using the MATLAB program scripts available through this package. Additional MATLAB scripts for processing traces are available from various sources. We especially use scripts geared toward compiling and truncating saved molecule traces available from Fu et al,[66] which can then be graphed as FRET histograms in commercially available graphing software such as OriginPro. For more complicated data processing, particularly in cases where molecules exhibit multiple FRET states, hidden Markov Model analysis can be a useful tool to elucidate the number of states exhibited, the interconversion rates between each state, and the time spent in each state[17,68]. Hidden Markov Model analysis is available for use through the program HaMMy available from http://bio.physics.uiuc.edu/HaMMy.html.

2.8

Technical Notes

Prism angle calculation

The trapezoidal prism is positioned above the specimen chamber and the objective. The prism directs the incoming laser beam to the quartz/water TIRF interface slightly larger than the so called critical angle at which the light will be completely reflected and total internal reflection (TIR) occurs. Hence, an evanescent field is created with the same frequency as the incident light, but the intensity decays exponentially with penetration

such that only fluorophores within the evanescent field are excited by the electromagnetic field and fluorescence is produced.
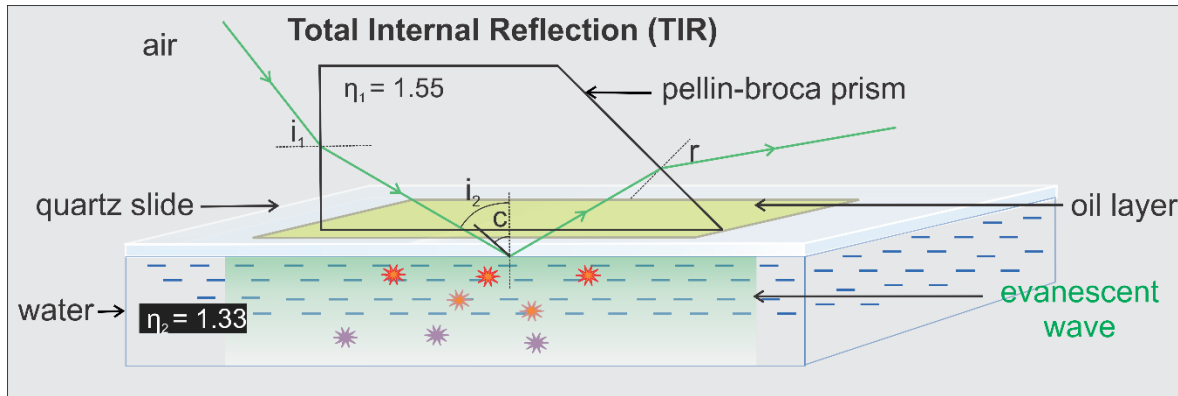
Figure 2.9 Schematic of the light path at the interface between two media in TIRFM imaging system. Refracted light at an angle of incident (i2) larger than the critical angle (c) undergoing total internal reflection, leading to the formation of evanescent wave.

Snell's law: $\eta_1 \sin i_a = \eta_2 \sin i_b$ [67]

Where η_1 and η_2 are the refractive indices of the medium 1 & 2 respectively. i_a & i_b are the angle of incident beam and the angle of refracted beam at the air/quartz prism interface. c is the critical angle.

$$c = Sin^{-1} \left(\frac{n_2}{n_1}\right) = Sin^{-1} \left(\frac{1.33}{1.55}\right) = 59.1°$$

According to Snell's law, for TIR to occur at the quartz slide/ water interface, the i_2 should be greater or equal to 59.1° which is the critical angle for the quartz slide/ water interface. The creation of the evanescent wave allows selective excitation of fluorophores that are on or close (typically ~100 nm from the surface)[42,69,70] to the surface.

Our actual setup corresponds to Fig. 2.9b, where i_1 is ~35° and the calculated value of i_2 is 68°, which is greater than the critical angle (59.1°) allowing TIR at the quartz-water

29

interface. The depths of penetration (d) calculated using the equation[42,69,70] below are 78 and 94 nm for the green (λ = 532 nm) and red (λ = 639nm) lasers, respectively.

$$d = \frac{\lambda}{4\pi}(\eta_1^2 sin^2 i_2 - \eta_2^2)^{-1/2}$$

where λ is the wavelength of the incident light in vacuum. The depth of penetration relies on i_2 (ultimately i_1), wavelength of the incident light, and refractive indices of the mediums, however it has been demonstrated that it is independent of the polarization of the incident light[42].

Prism clamp

The basic function of the prism clamp is to hold the prism in place and to provide a way to mount it to the prism support arm (described below). Our design has proven very reliable but any device which can accomplish the task would be suitable. Our prism clamp was designed in house and the design of the clamp is detailed in Figure 2.10. Our clamp was machined out of aluminum in Virginia Commonwealth University's on-campus machining shop. Off the shelf 8-32 machine screws from a hardware store were used to tighten the prism into place. It is important to remember that our clamp is dimensioned to a specific prism (part#:325-1206 UV FS Pellin-Broca Prism 11x20x6.4 mm), the design would need to be adapted for any other size of prism. While we chose to make the clamp out of aluminum for durability a 3D printed part with some modifications to insert nuts into the sidewalls of the clamp would also be a viable design.
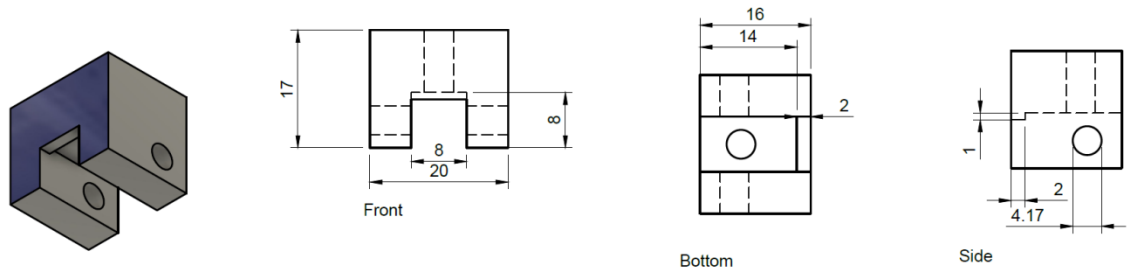
Figure 2.10 Dimensions of prism clamp from three directions. The sides are mirrored and the holes taped with 8-32 machine threading. All of the dimensions are in millimeter (mm).

Prism support arm

The prism support arm provides a mount for the prism clamp, we designed ours to work with our microscope but the dimensions could be altered to suit others. Our arm was printed out of PLA plastic on a MakerBot replicator (5th generation), .stl files will be made available upon request. Due to dimensional limitations of our printer the support arm was printed in two pieces and then glued together. We would recommend producing the arm as a single piece for durability if large enough printer is available or if machining the arm out of metal. It is also ideal to print the part in a matte black material to avoid potential laser scattering. The exact placement and size of the square center hole needed for the screw shaft to mount the prism clamp is dependent on the dimensions of the set up and where the prism needs to be mounted to achieve TIR. It is advised to use a long thin rectangular channel allowing space for the prism holder to be adjusted closer and further from the focusing lens.
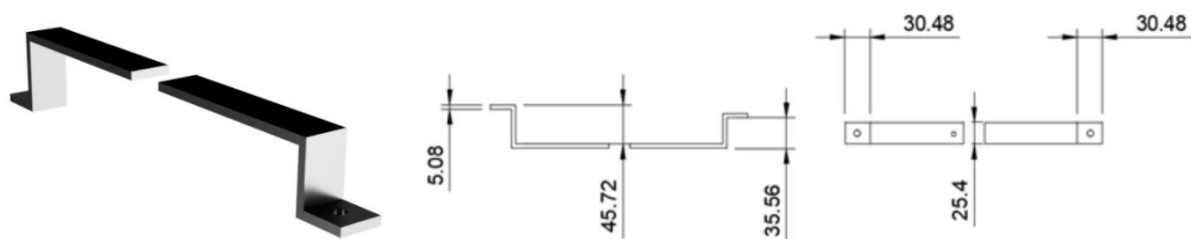
Figure 2.11 Dimensioned drawing of prism support arm from 3D printer file. Left, a 3D rendering of the finished item; Middle, side view; Right, top view. Units are in mm, round holes are 7.6 mm wide, square hole is 5 mm.

2.9 Conclusions

Here we describe the detail guidelines for building the prism-based TIRF microscope using commercially available microscope parts. Splitting the microscope setup procedure into three sections, (a) excitation path(s), (b) focusing and beam positioning, and (c) emission path, we presented stepwise instructions on building and characterizing a pTIRF instrument incorporating necessary precautions whenever necessary. Once the instrument is ready, in order to check its operation, we outlined flow cell design and its surface-functionalization, followed by conducting a representative pTIRF experiment using a dual-labeled DNA Holliday Junction. After data acquisition and analysis with the aid of MATLAB scripts and OriginPro, we saw clear conformation switching of Holliday Junction, thus demonstrating successful designing and functioning of our pTIRF microscopy. Although we tested our instrument with the Holliday Junction, this instrument is equally applicable to reveal dynamics, kinetics, and other structure/conformation related information of other biomolecules, such as RNA and proteins.

Chapter 3 : Single-molecule imaging of the conformational manipulation of Holliday junction DNA by the junction processing protein RuvA

3.1 Introduction

Homologous recombination (HR) plays a critical role in regulating genetic diversity and in repairing DNA double-stranded breaks (DSBs), and thus guards the genome against carcinogenic instability.[3,8,49] Evidence has accumulated over the past 30 years that the recombinational repair is conserved and the fundamental HR mechanism is similar across all organisms known to date. Since *E. coli* is better understood mechanistically than its eukaryotic counterparts, *E. coli* serves as a model system to investigate the currently outstanding questions regarding the mechanisms of recombinational repair. The entire HR process in *E. coli* can be generally divided into the early- and the late-stage HR (Figure 3.1a).[11,71] The HR events are initiated by an enzyme system called RecBCD (comprised of RecB, RecC, and RecD),[47,72–75] followed by the strand-exchange reactions catalyzed by RecA, leading to the formation of a cross-strand intermediate called the Holliday junction (HJ).[76–79] In the late stages of HR, the HJ is resolved into mature recombinant double-stranded DNA molecules by another enzyme system called RuvABC (Figure 3.1a).[14,80–84] While early stages of HR involving RecBCD have been studied down to single-molecule level[74,75,85], there remain substantial gaps in our understanding of the protein-DNA interactions at the late-stages of HR.
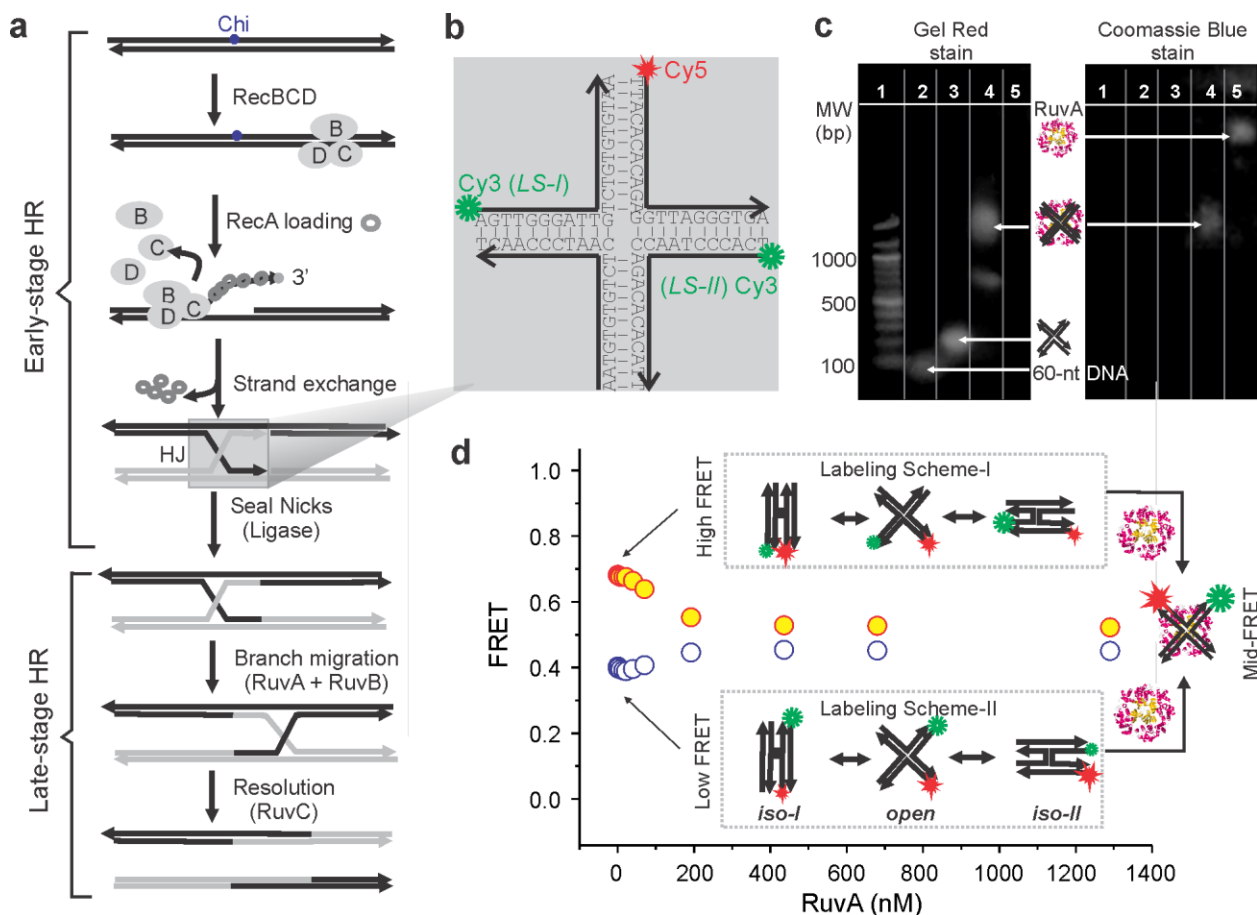
Figure 3.1 Experimental design and the bulk characterization of the interaction between RuvA and HJ. (a) Schematic of the RecBCD/RuvABC pathway in *E. coli* homologous recombination (HR). Early and late stages of HR are highlighted. (b) Schematic illustration of the HJ used in this study. Donor (Cy3) and acceptor (Cy5) fluorophores are shown in green and red respectively. While the Cy5 fluorophore is unchanged, the labeling position of the Cy3 fluorophore was different for different labeling schemes (LS-I in Scheme-I and LS-II in Scheme-II). (c) Native agarose gel characterization of the HJ and the RuvA-HJ complex using a native electrophoretic mobility-shift assay (native-EMSA). Left – gel red-stained agarose gel for detecting DNA; right – the same gel stained with coomassie brilliant blue for detecting RuvA. Lane 1: DNA molecular weight (MW) marker; Lane 2: 60nt ssDNA; Lane 3: HJ DNA; Lane 4: RuvA-HJ complex; and Lane 5: RuvA. (d) Bulk FRET analysis of RuvA binding to the HJ. Two labeling schemes of the HJ (Scheme-I and Scheme-II) were separately titrated with RuvA for the concentration range of 0 to 1.3 μM. The FRET analyses were performed in 1× TAE buffer (pH 7.4) containing 12 mM Mg^{2+}. Although it does not change our experimental goals, it is important to note that EDTA, a component of TAE buffer, is a chelating agent and will reduce the effective Mg^{2+} concentration by ~1 mM. Images of the RuvA tetramer in Figures 1c and 1d were taken from Protein Data Bank (PDB).

34

Single molecule dissection of the binding interaction is important to develop our understanding on how repair proteins recognize and process the junction. In vitro studies have shown that the RuvA protein recognizes and binds to the HJ with high affinity (affinity for HJ is >20 fold than for dsDNA) to which it recruits a helicase protein RuvB forming an ATP-dependent motor called RuvAB.[86–88] In the presence of ATP, the RuvAB motor promotes branch migration of the HJ in which the DNA is pumped out through the protein complex.[14,80–84] Several structural, mutational and biochemical analyses have provided evidence that the formation of RuvA-HJ complex is the first critical step in the RuvABC-mediated resolution of the HJ.[14,15,88] However, the mechanistic detail of the binding interaction between RuvA and the HJ has remained elusive. Further, recent studies suggested that the HJs are highly dynamic with structural fluctuations between stacked X conformers of iso-I and iso-II and an open square-planer conformation (Figures 3.1).[47,48,69] It raises an important question – how will the dynamic characteristics of the junction be affected by the interaction between RuvA and the HJ? Using smFRET we demonstrated, for the first time, the conformational manipulation of the HJ by RuvA at the single molecule level.

Because of its central role in the HR process, the HJ has also been seen as a potential target in therapeutics.[50–56] For example, HJ is believed to play a vital role in the alternative lengthening of telomeres (ALT) in cancer cells.[50,55] However, the therapeutic application of HJ is still premature. The successful implementation of the HJs in therapeutics would not only require better understanding of their interactions with junction resolving proteins, but also need to carry out an extensive study regarding how and to what extent DNA modifying drugs impact such interactions. Given that the protein-DNA interactions are

highly sensitive to many factors such as DNA sequences, topology, and other microenvironments, it is expected that the interaction between RuvA and the HJ is disrupted by the formation of drug-DNA adducts. Since there is no report that directly addresses this outstanding knowledge gap, using cisplatin as a proof-of-concept chemotherapeutic drug, we investigated the effect of drug-DNA adduct on the binding interaction between RuvA and HJ.

In this study, we employed smFRET and ensemble fluorescence analyses to visualize and characterize the binding interaction between RuvA and HJ. Using complementary fluorescence labeling of the HJ, we first visualized the conformational dynamics of the junction. Our HJ showed a strong bias toward one of its stacked X isomers. Using the same junction, we show that the binding of RuvA halts the conformational dynamics of the HJ at physiologically relevant concentrations of Mg^{2+}, however, the binding is interrupted at high mM concentration of Mg^{2+}. These results reinforce that the electrostatic interaction between DNA and RuvA is the key stabilizing factor for the RuvA-HJ complex. In addition, introducing the widely used chemotherapeutic drug cisplatin,[89–93] we found that RuvA binds to the cisplatin-modified HJ as efficiently as to the regular HJ. These results imply that RuvA accommodates for the cisplatin-introduced charges/topological changes on the HJ. Taken together, through our systematic single-molecule and ensemble analyses, we have revealed several key factors governing the interactions between RuvA and the HJ. These findings have the potential to trigger quests for new drugs to manipulate of HR process by selective targeting of the HJ.

Materials and Methods

Chemicals.

Tris(hydroxymethyl)-aminomethane (tris), acetic acid, KCl, EDTA and agarose were purchased from Fisher Scientific. Magnesium chloride hexahydrate, 6-hydroxy-2,5,7,8-tetramethylchroman-2-carboxylic acid (trolox), and 30% ammonia water were purchased from Arcos Organics. Sodium chloride, coomassie brilliant blue, streptavidin, protocatechuic acid and hydrogen peroxide were purchased from VWR. Bovine serum albumin (BSA) was purchased from New England Biolabs (NEB). Protocatechuate 3,4-dioxygenase (PCD) was purchased from MP Biomedicals, and suspended in a pH 8.0 PCD Buffer (100 mM Tris-HCl, 50 mM KCl, 1 mM EDTA, 50% glycerol) at 0.2 µM, sterile filtered, and stored at -20ºC. Biotin-modified BSA was purchased from Peirce, dissolved in sterile H_2O at 1 mg/mL, sterile filtered and stored at -20ºC. Cisplatin was purchased from VWR and freshly dissolved in PBS buffer (137 mM NaCl, 2.7 mM KCl, 10 mM Na_2HPO_4, 1.8 mM KH_2PO_4) at pH 7.0 as needed.

DNA constructs and enzyme.

All of the modified and unmodified oligos were purchased from Integrated DNA Technologies (IDT DNA) and stored at -20ºC. DNA constructs containing HJ with the labeling schemes I & II (Figure 3.2) were constructed by thermal annealing of the constituent ssDNA oligos (Table 3.1) at 1 µM concentrations in 1× TAE-Mg buffer, pH 7.4 (40 mM Tris, 20 mM acetic acid, 1 mM EDTA, 12 mM Mg^{2+}). The thermal annealing was carried out by ramping the temperature of the solution from 95°C to 4°C in a thermal cycler (Table 3.2). Active *E. coli* RuvA was purchased from Abcam (Cambridge, MA) and stored at -20ºC.
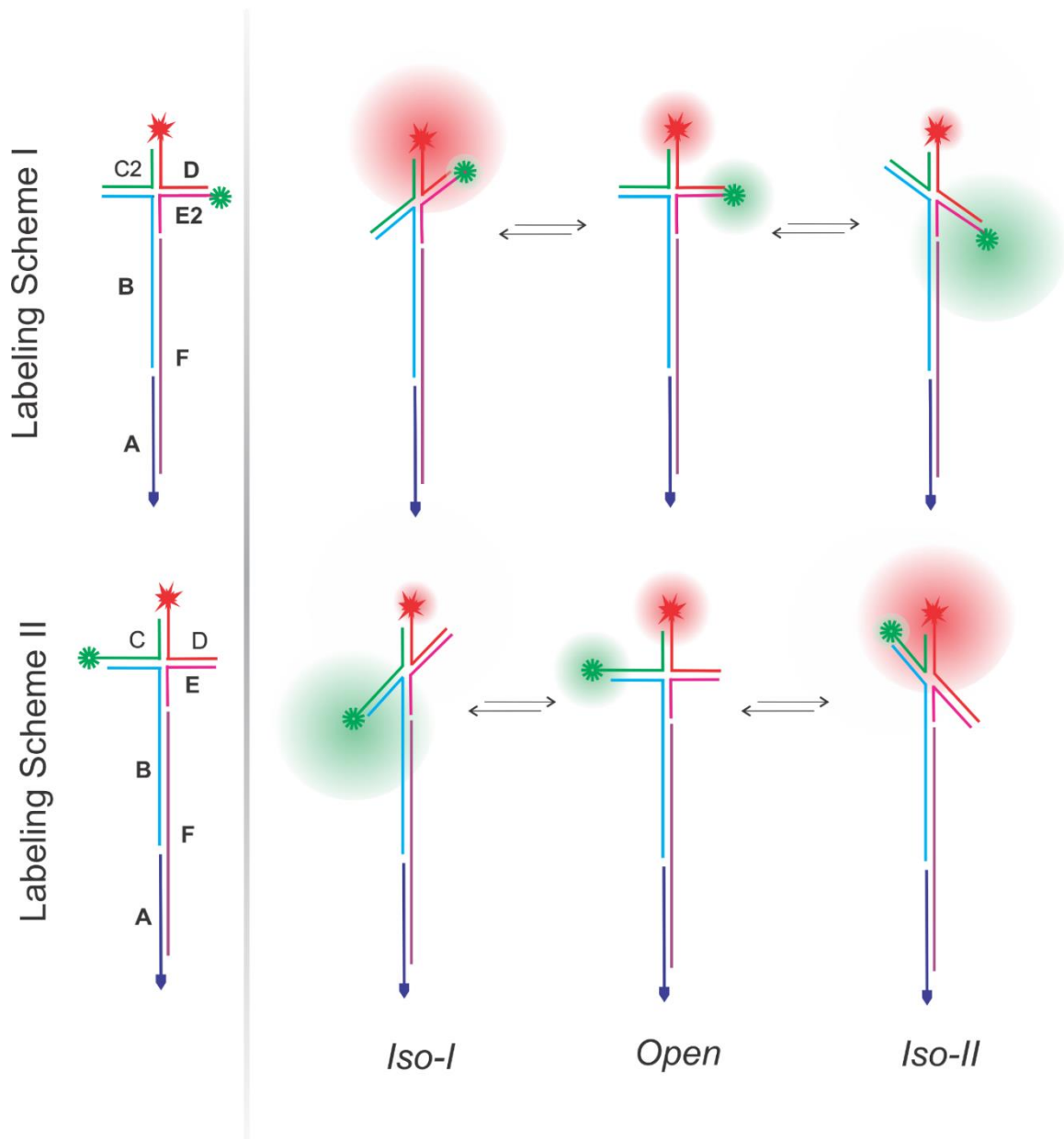
Figure 3.2 Holliday junction (HJ) construct with labeling scheme-I (top) and II (bottom). The left panel highlights the HJ construct with fluorophore labeling schemes. The right panel shows the expected conformational switch between stacked X isomers I & II via the open unstacked conformation. The FRET efficiency is indicated with a bloom of color with more red indicating higher efficiency. Sequences of the DNA strands (strand A to F) used to assemble the HJ construct are provided in Table S1. Strand A was biotin modified to enable surface immobilization of the HJ construct.

Table 3.1 Sequences for all the oligonucleotides used in constructing biotin, Cy3, and Cy5 labeled HJs. All of the biotin- and fluorophore-modified DNA oligos were purchased HPLC purified.

Strand Name	Sequence (5′-3′)
A	/biotin/-ACGCGCTGGGCTACGTCTTGCTGGCCGCAT
B	CTGTGCGGTATTTCACACCGTTAGCTCAGGTTTTAATGTG TGTCTCAATCCCAACT
C	/Cy3/AGTTGGGATTGTCTGTGTGTAA
C2	AGTTGGGATTGTCTGTGTGTAA
D	/Cy5/TTACACACAGAGGTTAGGGTGA
E	TCACCCTAACCAGACACACATT
E2	/Cy3/TCACCCTAACCAGACACACATT
F	CCTGAGCTAACGGTGTGAAATACCGCACAGATGCGGCCA GCAAGACGTAGCCCAGCGCGT

Table 3.2. Thermal annealing program for the HJ DNA constructs.

Temperature (^{0}C)	Time (min)
95	5
93	5
90	5
88	5

86	5
84	5
82	5
80	5
78	5
76	5
72	5
68	5
64	5
60	5
56	5
52	5
48	5
44	5
40	5
36	5
32	5
28	5
24	5
4	hold

Electrophoretic Mobility Shift Assay (EMSA)

RuvA-HJ Interaction: A 2% agarose gel was cast and immersed in a buffer system consisting of 2 mM $MgCl_2$, 1× TAE, 69 mM NaCl at pH 7.4. RuvA and HJ were incubated in the gel running buffer at a 1.2:1 molar ratio (RuvA : HJ :: 10 : 8.33 µM) for 15 min before being run in the gel along with oligo F (60nt-long ssDNA control), the HJ construct, the RuvA-HJ complex, and an RuvA control (Figure 3.1c). The 100 base-pair ladder was used as a molecular weight (MW) marker. The gel apparatus was run in an ice bath at 65

V for 120 min before being stained with 3× Gel Red (Bioteum) and imaged using UV transilluminator (254 nm). To visualize the RuvA, the gel was then stained with coomassie brilliant blue, de-stained in water overnight at room temperature and imaged (Figure 3.1c).

Cisplatin activity: A 2-kbp fragment of DNA was acquired through polymerase chain reaction (PCR) of plasmid pBR322 and incubated in PBS buffer in the presence and absence of 50 μM cisplatin for 24 hrs. A 1% agarose gel was cast and immersed in 1× TAE buffer at pH 7.4. These samples were loaded onto the gel and run at 80 V for 1.5 hrs.

Bulk Fluorescence Assays

The bulk fluorescence assays were carried out using a fluorometer (Denovix, F11) at 50 nM HJ in 1× TAE-Mg buffer (pH 7.4) using a Denovix FX-11 fluorimeter set to excite at 525 nm and to collect intensities at 565 - 650 nm and 665 - 740 nm for green and red emissions, respectively. To retard photobleaching of the fluorophores, a protocatechuate-3,4-dioxygenase(PCD)-based oxygen scavenging system (1 μM PCD, 100 mM protocatechuic acid and 2mM Trolox) was used.[62,69,94] In addition, 0.2 mg/mL of bovine serum albumin (BSA) was added to the buffer to reduce non-specific binding of the HJ and protein to the microtubes. In magnesium titration, the concentration of $MgCl_2$ was varied in the buffer. Similarly, the RuvA titration study was carried out by varying the concentration of RuvA from 0 to 1.3 μM. From those samples, the fluorescence intensities for donor (Cy3) and acceptor (Cy5) channel were collected when the solution was illuminated using green excitation. The FRET efficiency was calculated as $I_A/(I_D + I_A)$, where I_A and I_D stand for the background-corrected intensities of acceptor and donor, respectively. In the experiments involving cisplatin, the HJ is incubated with 50 μM

cisplatin for 24 hrs before incubating with RuvA. All bulk fluorescence assays were performed at room temperature (23°C).

Single Molecule Fluorescence Microscopy

The flow cell consists of a standard sized quartz slide (75 × 26 × 1 mm) was drilled diagonally (using a diamond coated drill bit of 1 mm in diameter in a Dremel multitool) through the face of the slide to obtain two holes (Figure 2.7). The slides were cleaned using published protocol[72,75]. Briefly, slides were washed in warm soapy water and then scrubbed thoroughly in a thick paste of Alconox and water, and rinsed clean in warm water, deionized water ethanol and acetone successively before being immersed in a boiling solution of 4% hydrogen peroxide and ammonia water for 5 min. The slides were then flamed for 2 min on both sides using propane torch.

To assemble a flow cell, an oblong chamber was cut into parafilm and placed on the microscope slide, a glass coverslip (24 x 60 mm, Fisher Scientific) was placed over the parafilm and then the whole assembly was heated to 120°C for 5 min on a hot plate. About an inch long pipet tips (200 μL plastic pipet tips) were cut, inserted into the holes and plumed with tubing (0.02 in. ID, 0.06 in. OD, Cole-Palmer) using Double Bubble Quick-Set epoxy from Hardman Adhesives. For the single molecule experiments, the flow cells are functionalized by sequential incubation with 1 mg/mL biotinylated BSA for 5 min and 0.2 mg/mL streptavidin for 2 min. The flow cells were then flushed with ~300 μL of 1× TAE-Mg buffer before and after incubating with streptavidin.

Single molecule sample preparation and imaging. The functionalized flow cell was incubated with 20 pM HJ (dispersed in 1× TAE-Mg buffer) for ~1 min before being flushed

with the same buffer to remove the unbound HJ. The imaging buffer consisted of 1× TAE

buffer and 1× OSS (40 mM PCA, 50 nM PCD, 5 mM Trolox) and desired concentration of

RuvA (400 nM, 1 μM or 5 μM) and $MgCl_2$. In the experiments involving cisplatin, the HJ

was incubated with 50 μM cisplatin for 30 min before injecting into the microscope slide.

The movies were recorded after 5 min incubation of the slide with imaging buffer

containing OSS. Cy3 fluorophore was continuously excited using a 532 nm HeNe laser.

Fluorescence emission from Cy3 and Cy5 fluorophores was simultaneously recorded for

the green and red channels (512 × 256 pixels) using EMCCD camera (iXON 897, Andor)

at 50 ms (for 300 mM Mg^{2+}) or 100 ms (for 2mM Mg^{2+}) time resolution. We used our

custom-built prism-based total internal reflection fluorescence (pTIRF) microscope for all

of the single-molecule experiments (Figure 2.2). The microscope setup is similar to

previously described prism-based TIRF microscopes.[63,66,70,95,96] Briefly, the microscope

consists of a red 639 nm excitation, 40 mW laser, (Coherent technologies, CUBE laser)

and a green 532 nm, 50 mW laser (Crystalaser, CL-532). Both lasers are designed to

focus though an optical quality glass pellin-broca prism onto the focus of an inverted light

microscope (Olympus, IX73; 60X/1.2W objective), thereby creating an evanescent field

on the microscope slide by total internal reflection of the laser beam (Figure 3.4). The

fluorescence emission of the sample collected by the objective is split off through an

Optosplit II (Cairn Research) and split into red and green channels before being routed

to an EMCCD camera (IXON Ultra, DU-897U-C50-#BV). The presence of an active FRET

pair was confirmed at the end of each experiment by the excitation with a 639 nm red

laser. Experimental concentration of RuvA and Mg^{2+} are indicated in each figure or in the

figure captions wherever applicable. All single molecule experiments were performed at room temperature (23°C).

Single Molecule Data Analysis

Movies from the single molecule experiments were processed into trace files using IDL and MatLab scripts acquired from the smFRET data acquisition and analysis package available from TJ Ha Lab (https://cplc.illinois.edu/software/). Briefly, the single molecule intensity traces generated by running these scripts were manually selected for subsequent analysis based on the following expected features: (i) single-step photobleaching; (ii) total fluorescence of Cy3 and Cy5 exceeding 200 counts per frame; and (iii) evidence of both Cy3 and Cy5 signals. The FRET histograms of smFRET traces were prepared for the first 10 to 20 s observation time depending on the movies. Gaussian fittings of visually apparent populations were accomplished in Origin 2017.

Hidden Markov Model (HMM) analysis.

HMM analysis was performed using HaMMy[68,97] to calculate the rate of transitions between two FRET levels (from iso-I to iso-II in this study). Single molecule FRET traces at 300 mM Mg^{2+} were analyzed for the interconversion rates of the isomers for both labeling schemes I & II. A truncated 50 sec window of the HMM analysis for each labeling scheme is shown in Supporting Information.

3.3

Results and Discussion

RuvA manipulates the conformational dynamics of the HJ.

The sequence design and construction of our HJ is based on previous reports (Figure 3.1b).46 Single-stranded DNA (ssDNA) oligomers were used to form the HJ with 11-base

pair (bp) arms (see Tables 3.1 and 3.2 for sequence detail and thermal annealing protocol, respectively). Donor (Cy3) and acceptor (Cy5) fluorophores were incorporated into the HJ to allow monitoring of the conformational dynamics of the junction using FRET (Figures 3.1 and 3.2). The formation of the HJ was confirmed by running a native 2% agarose gel (Figure 3.1c). Compared to the control 60-nt DNA strand, the native gel showed a slower migration for the HJ construct indicating the successful assembly of the junction. After incubating the HJ with a slight excess of RuvA (1.2:1 molar ratio of RuvA:HJ), a band with a significantly slower migration was observed, suggesting the formation of RuvA-HJ complex (Figure 3.1c, lane 4). The formation of the complex was then confirmed by coomassie brilliant blue staining of the same gel, which showed co-localized RuvA and HJ bands. Further, the faster migration of the RuvA-HJ complex compared to RuvA itself (Figure 3.1c, lane 5) suggests that the negative charge on DNA increased the electrophoretic mobility of the RuvA.

HJs are known to undergo spontaneous conformational switching between stacked X-isomers (isomer-I and –II) via an open unstacked conformation (Figure 3.1d).[27-29] Our experimental conditions rule out the possibility that the FRET fluctuation is due to binding/unbinding of molecules as we washed off the unbound molecules before imaging (see Materials and Methods) Previous reports have shown that the distribution of isomers relies on the preferential stacking of nucleotide bases at the junction.[47,48,82,98,99] To visualize the binding of RuvA to the dynamic HJ, we performed bulk FRET measurements in which the concentration of RuvA was varied from 0 to 1.3 µM (Figure 3.1d) while the concentration of HJ was kept at 30 nM (low concentration of fluorophore-labeled HJ was necessary to keep the background low). Interestingly, the FRET efficiency of the HJ was

45

gradually decreased from 0.68 to 0.52 and leveled off after ~200 nM RuvA (Labeling Scheme-I). The FRET values at high RuvA concentrations were consistent with what is expected for an open unstacked HJ. These results suggested that the binding of RuvA halts the conformational switching of the HJ and clamps the open, unstacked conformation.[14,15] This observation was further confirmed by using a complementary labeling scheme (Labeling Scheme-II) of the same HJ where the low- FRET isomer now becomes a high-FRET isomer. As expected, the FRET efficiency in this case was gradually increased from 0.40 to 0.45 with no change in FRET past 200 nM RuvA (Figure 3.1d). Fitting of the bulk FRET data with the hill equation (Figure 3.3) yielded similar binding constants (Kd of 106 nM and 97 nM for labeling schemes I & II respectively). The binding constant determined here is ~2 fold higher than the literature reported value for *E. coli* RuvA in a different buffer condition.[95] We reason that the higher Kd of RuvA in our experiment is due to Mg^{2+}, resulting a slightly weaker interaction between RuvA and the junction (see Mg^{2+} titration experiment in later section). Under our experimental conditions, we estimated the free energy change (*ΔG*) of RuvA binding to be ~2.5-fold higher than the reported maximum energy barrier (~15 kJ mol-1) for the HJ going from the stacked to open conformation (Figure 3.1),[29] meaning that the binding of RuvA should sufficiently stabilize the open conformation of the junction.
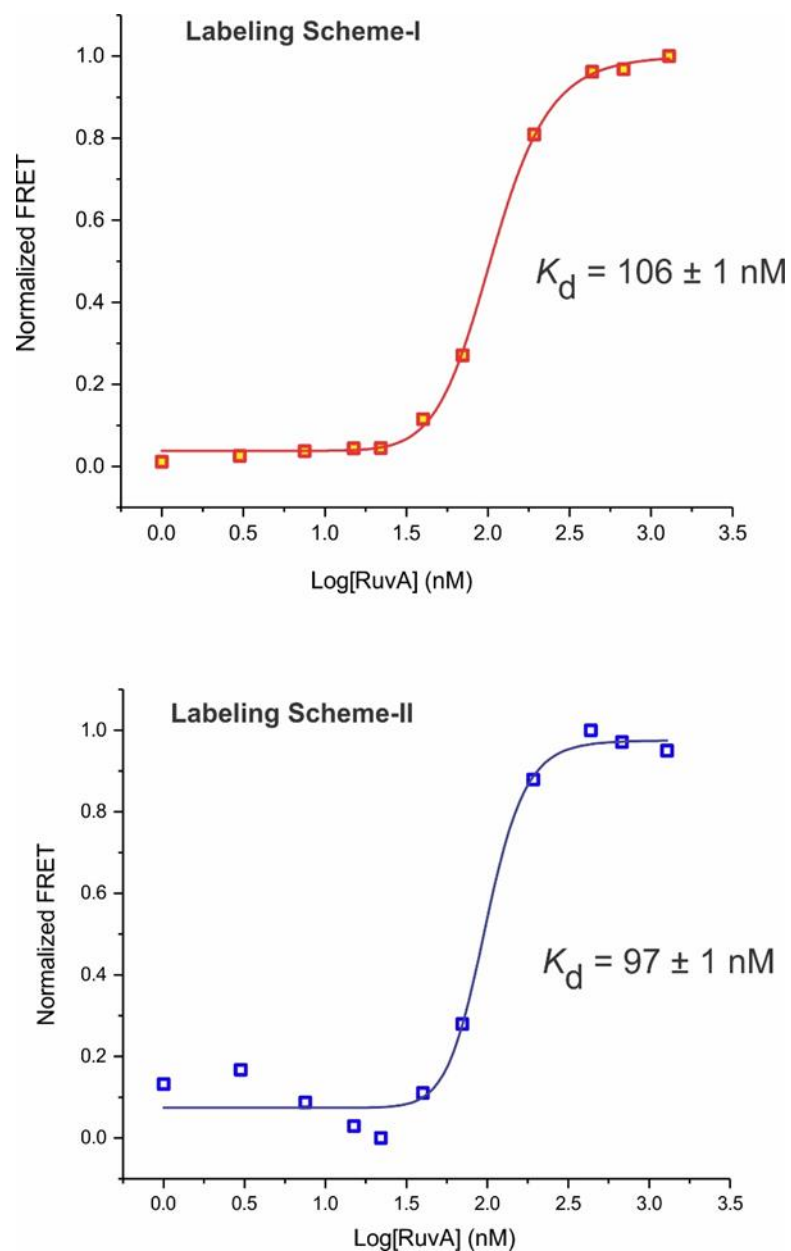
Figure 3.3 Bulk FRET analysis of binding (data from Fig. 1d). A 30 nM solution of HJ with either the labeling scheme-I or the labeling scheme-II was titrated with RuvA. The background-corrected FRET data were normalized between the FRET values of 0 to 1 and fitted with the standard binding isotherm (hill equation) in Origin to determine Kd. This analysis yielded Kd values of 106 ± 1 nM and 97 ± 1 nM for the labeling Scheme -I (top panel) and Scheme-II (bottom panel), respectively. The average ΔG of RuvA binding, defined as -RTlnKd, from the labeling Scheme-I and labeling Scheme-II is estimated to be ~39 kJ mol-1 at room temperature (23°C).

Although we observed an obvious change in the FRET level upon binding of RuvA to the HJ (Figure 3.1d), due to the inability to track conformational dynamics of the junction in bulk solution, the dynamic aspect of the RuvA-HJ interaction was missing. The dynamic characteristics of the junction are important in understanding how different enzymes recognize and process the junction. Therefore, we turned to single-molecule FRET (smFRET) for the quantitative analysis of HJ dynamics and its binding interaction with RuvA. The basic setup of the smFRET experiments used in this study is shown in Figure 3.4a. Our custom-built fluorescence microscope which is similar to previously published setups[63,66,70,95,96] is shown in Figure 2.2 The biotin-modified HJ was surface immobilized on the biotin-BSA/streptavidin coated quartz slide (see Methods and Figures 2.7 and 2.2 for details). An oxygen scavenging system (OSS) was added to retard photobleaching of the fluorophores[62,69,94]. Since the HJs interconvert between the stacked X-structures with a lifetime of a few milliseconds,[47,48] such transitions are too fast to be captured in our fluorescence microscope without slowing down the interconversion rates.
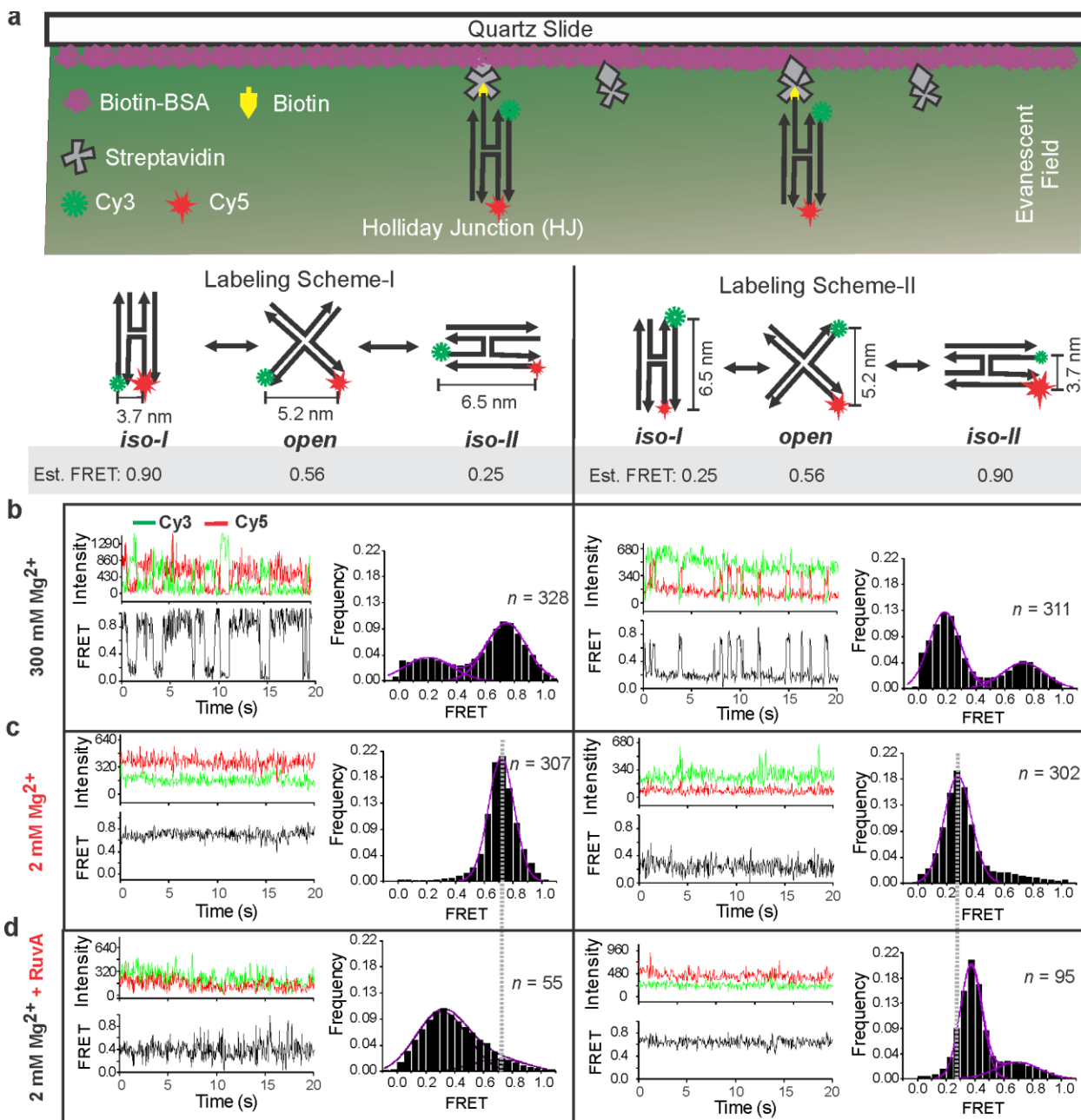
Figure 3.4 Single-molecule characterization of the interaction between RuvA and the HJ. (a) Top panel: Experimental setup for the smFRET analysis of the HJ. The biotin-labeled HJ is surface immobilized on a biotinylated-BSA (bBSA)/streptavidin coated quartz slide. Bottom panel: Complementary fluorophore-labeling schemes (Scheme-I, left panel & Scheme-II, right panel). The estimated inter-dye distances and the corresponding FRET efficiencies ("Est. FRET") are shown for the HJ isomers for both labeling schemes (see Table S3 for detail calculation). It is important to note that the inter-dye distances and FRET values are estimated without considering dye linkers and other local microenvironments, which may underestimate the inter-dye distances and overestimate the FRET values. The smFRET results are shown in Figures b-d. (b) smFRET analysis

of the HJ at 300 mM Mg^{2+} in 1×TAE buffer, pH 7.4. (c) Same experiment as in (b) except at 2 mM Mg^{2+}. (d) smFRET measurements at 2 mM Mg^{2+} in the presence of RuvA. The vertical dotted lines and the horizontal arrows are used to guide the FRET shift due to RuvA binding. Typical smFRET-time traces for each set of experiments are shown to the left of the corresponding histograms. All histograms were fitted with one- or two-peak Gaussian function to determine the mean FRET values and their corresponding populations. The n values depict the number of smFRET traces used in each histogram. The FRET vs time data (~1,000 data points corresponding to the first 10 s observation time) from the smFRET traces for the given experimental condition were combined without averaging and the data were binned to a 0.05 FRET value before plotting the histogram.

Taking advantage of previous single-molecule studies that showed that the electrostatic stabilization of the stacked structures dictates the interconversion rates,[48] we performed smFRET experiments at 300 mM (Figure 3.4b) to investigate the switching behavior of the HJ. The smFRET analysis of Labeling Scheme-I showed an obvious switching between a low- and a high-FRET conformations yielding the populations with mean FRET values of 0.22 (34% population) and 0.72 (66% population) (Figure 3.4b, left panel). As expected, the population distribution was reversed in the complementary labeling scheme of the same HJ (Labeling Scheme-II, Figure 3.4b, right panel). These results suggest that the HJ exhibits two isomers, iso-I and iso-II with a strong bias toward iso-I.[100] Since the HJ passes through the open conformation quickly without any dwell time, we did not see it even in our slowed HJ.[47,48,69] Further, as expected the interconversion rates obtained by Hidden Markov Model (HMM) analysis[68,97] of the FRET traces for both labeling schemes were self-consistent (Figure 3.5). The free energy difference (ΔG) between iso-I and iso-II, defined as -RTln kI-II/kII-I, is calculated to be 2.5 kJ mol^{-1}. The calculated ΔG is consistent with the literature reported value of ~3.0 kJ mol^{-1}.[29]
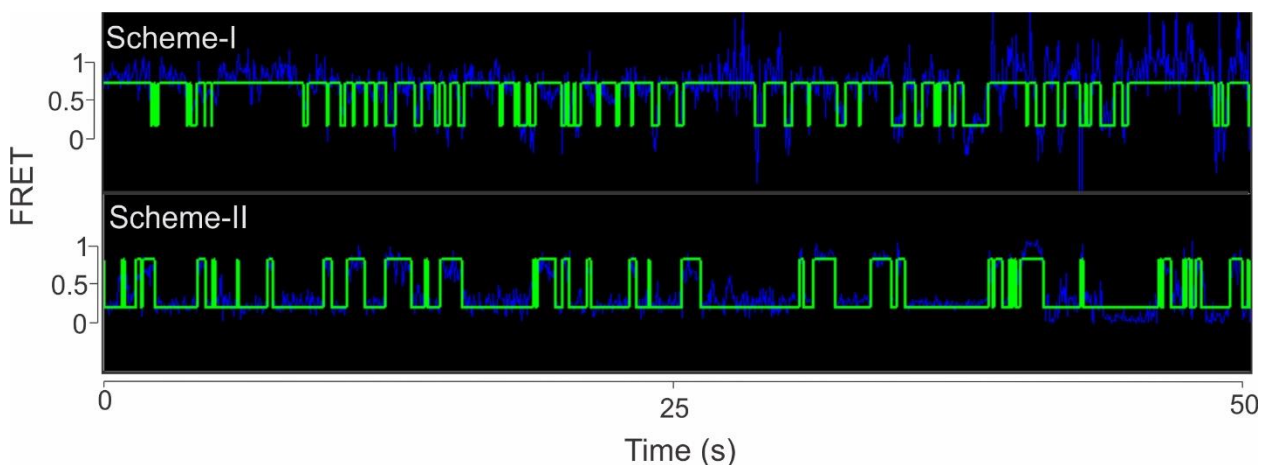
Figure 3.5 HMM analysis of the HJ with labeling scheme-I & II. Only small sections of the entire concatenated single molecule traces (blue) are shown. Please note that scheme-I spends more time in the high FRET state (~0.72) and scheme-II spends more time in the low FRET state (~0.22). Rates of interconversion between the states obtained from the HMM analyses (green traces) for both labeling schemes (listed on the table below) were identical as a result of their identical sequence.

Labeling Scheme	iso-I → iso-II ($k_{I\text{-}II}$)	iso-II → iso-I ($k_{II\text{-}I}$)
I	0.738 s^{-1}	2.01 s^{-1}
II	0.738 s^{-1}	2.01 s^{-1}

Next, we performed smFRET analyses of the same HJ under a physiologically relevant concentration of Mg^{2+} at +/- RuvA (Figures3.4c and 3.4d). Our choice of Mg^{2+} as an electrostatic stabilizer of the HJ is highly relevant as Mg^{2+} serves as a co-factor for hundreds of enzymatic reactions and critically stabilizes many enzymes.[85,100] Interestingly, in 2 mM Mg^{2+}, the smFRET analyses showed a single population with a mean FRET value of 0.72 for the labeling Scheme-I and 0.28 for the labeling Scheme-II (Figure 3.4c). We reason that the interconversion rate of the isomers in 2 mM Mg^{2+} is faster than the camera integration time (50 ms) thereby yielding an average FRET state. These results are in accordance with the previous findings that the Mg^{2+} ions decelerate

the interconversion between iso-I and iso-II.[48] More importantly, we performed smFRET

analyses of the HJ in the presence of RuvA under the same buffer conditions as in Figure

3.4c. In labeling Scheme-I, there was an obvious decrease in the mean FRET value from

0.72 to 0.38 (83% population) at 1.0 µM RuvA (Figure 3.4d, left panel). Similar

experiments for labeling Scheme-II shifted the mean FRET value from 0.28 to 0.37

(Figure 3.4d, right panel). These values differ slightly from the FRET values of 0.52 and

0.47 determined from the bulk RuvA titration (Fig. 3.1d). This is due to the nature of the

single-molecule experiments allowing us to select those molecules that are fully formed

with both fluorophores present. As the expected FRET shift is tiny for the labeling scheme-

II, we used a much larger excess of RuvA (5.0 µM) to confirm the formation of RuvA-HJ

complex beyond doubt. Overall, an emergence of a mid-FRET population in the presence

of RuvA in bulk (Figure 3.1d) as well as in smFRET (Figure 3.4d) unequivocally

demonstrated that RuvA clamps the open conformation of the HJ, halting its dynamics.

In addition, the smFRET traces show static FRET traces for the entire observation time

in the presence of RuvA suggesting that the RuvA-HJ complex is highly stable once

formed. To our knowledge, this is the first FRET-based visualization of the conformational

manipulation of HJ by RuvA at the single-molecule level.

Mg^{2+} shields the interaction between RuvA and the HJ.

Previous experimental and computational analyses of the RuvA-HJ complex

proposed that the binding occurs via electrostatic interaction[15,88] but the specificity comes

from the acid pins (two key amino acids: Glu55 and Asp56)[71] present on the DNA binding

site of RuvA. However, there is no systematic study on how the ionic environments

modulate the binding. Therefore, we went on to systematically investigate the effect of

the ionic environments in the formation of the RuvA-HJ complex. Here, and in all subsequent experiments, we used the HJ with labeling Scheme-I as it provides a more obvious shift in the FRET levels at +/- RuvA (Figures 3.4c & 3.4d, right panels) allowing an easier detection. In this regard, using bulk FRET measurements of the HJ sample in which Mg^{2+} was added before incubating with RuvA, we observed that the FRET is increased with increased concentration of Mg^{2+}. Based on the FRET levels, we assigned the overall titration data into three categories (shaded areas in Figure 3.6a): the intact RuvA-HJ complex ('Bound'), bound-to-unbound transition ('T'), and the dissociation of RuvA ('Unbound'). These semi-quantitative analyses showed that the RuvA-HJ interaction is favorable up to ~25 mM Mg^{2+} and disrupted afterwards. We attributed this observation to the electrostatic shielding of negatively charged DNA by Mg^{2+} ions, thereby preventing the HJ from interacting with RuvA. Our smFRET analysis at 150 mM Mg^{2+} showed nearly identical FRET histograms at +/- RuvA (Figure 3.6a, inset) further confirming that the RuvA-HJ interaction was completely abolished at this concentration of Mg^{2+}. Overall, with the Mg^{2+} titration experiment we demonstrated that the interaction between RuvA and the HJ is predominantly electrostatic.
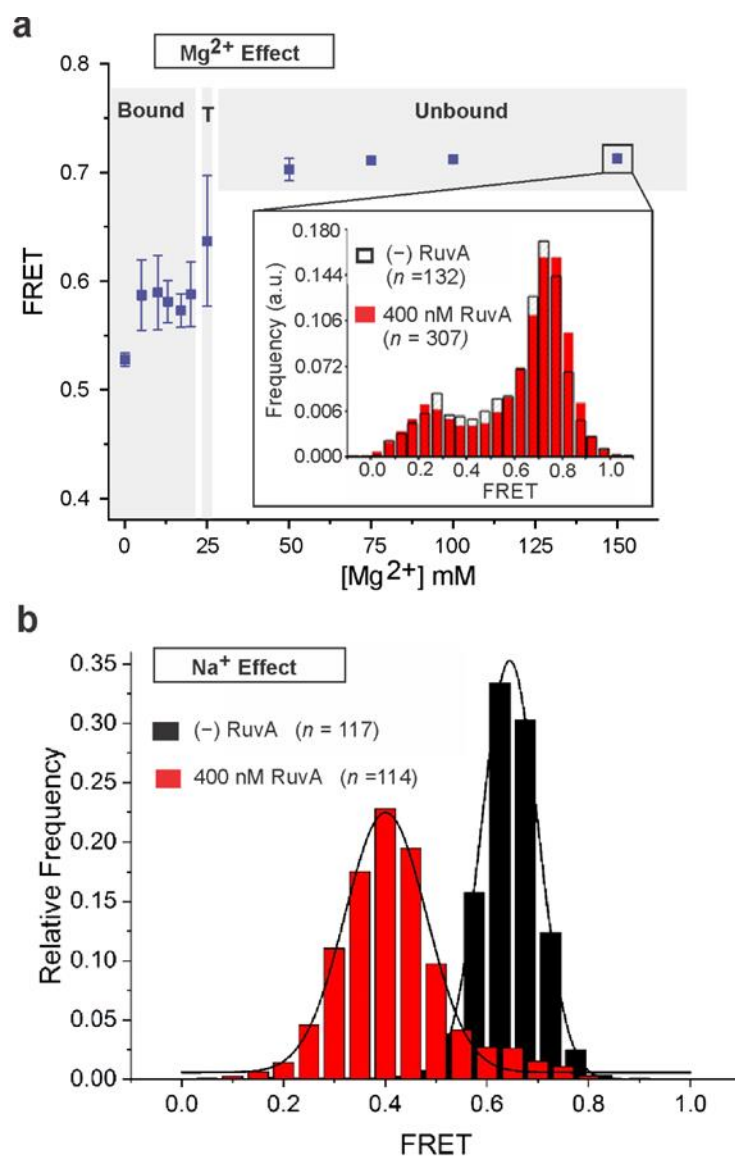
Figure 3.6 Effect of Mg^{+2} and Na^+ ions in binding interaction between RuvA and the HJ. (a) Bulk FRET at different concentrations of Mg^{2+} in 1× TAE buffer (pH 7.4). Shaded regions highlight the intact RuvA-HJ complex ('Bound'), bound-to-unbound transition ('T'), and the dissociation of RuvA from the HJ ('Unbound'). Error bars represent standard deviation from three replicate experiments. Inset, smFRET histograms from +/- RuvA at 150 mM Mg^{2+} in the same buffer. (b) smFRET histograms at +/- RuvA in 1× TAE buffer at 2 mM Mg^{2+} and 137 mM Na^+. The HJ with Labeling Scheme-I was used. The n values depict the number of single molecule traces in each histogram.

Since proteins are known to function better in saline buffer, we examined the binding after adding 137 mM NaCl to our existing 1× TAE buffer. Interestingly, the binding of RuvA

is 100% even at relatively lower concentration of RuvA (400 nM instead of 1.0 µM in Figure 3.4d) as observed by the shift in the mean FRET level from 0.65 to 0.40 (Figure 3.6b). This observation suggested a more efficient binding of RuvA to the HJ in the presence of Na^+. An efficient binding of RuvA in the presence of Na^+ ions was also persistent with narrow histograms in Figure 3.6b than that in Figure 2d. Taken together, the Mg^{2+} titration and the smFRET measurements using a physiologically relevant concentration of Mg^{2+} and Na^+, we demonstrated that the interaction between RuvA and the HJ is electrostatic in nature and the interaction is sensitive to microenvironments.

RuvA binds efficiently to the cisplatin-modified HJ.

After the recent realization that many cancers are associated with HR repair deficiency, manipulation of the HR process has been seen as a potential therapeutic tool in cancer therapy.[50–56] Although identifying protein inhibitors that can selectively modulate the HR process is preferred in therapy, this approach is extremely challenging as the functions of proteins significantly overlap in different subpathways of HR. Therefore, exploiting chemotherapeutic drugs to manipulate the HR repair process is quite promising to overcome this challenge. While most cancer drugs lead to cell apoptosis via binding to DNA and thus altering the cell biology, little is known about how DNA repair enzymes function with drug-modified DNA. In this regard, we used a cisplatin-modified HJ as a model system to answer this outstanding question.[89–93] Cisplatin is known to cross-link DNA bases, introduce bending by 32˚- 40˚, and widen the minor groove (Figure 3.7a).[90,101]Contrary to our initial hypothesis that the charge/topological changes of DNA double-helix would disfavor the interaction between RuvA and HJ, through bulk titration under a clinically relevant concentration of cisplatin,[102–104] we observed no difference in

the FRET value at +/- cisplatin (Figure 3.7b). These results strongly suggest that the binding was not compromised by cisplatin-modification of the HJ. As a precaution, to verify that the cisplatin stock was active under our experimental conditions, we examined the formation of cisplatin-DNA adduct using a 2-kb DNA obtained from the polymerase chain reaction (PCR) of a plasmid DNA pBR322.[105,106] The slower electrophoretic mobility of the cisplatin-treated DNA than that of untreated DNA (Figure 3.8) confirmed that our cisplatin stock was active.[107,108] We further performed smFRET experiments of the cisplatin-treated HJ at +/- RuvA (Figure 3.7c). The mean FRET values of cisplatin-treated HJ at +/- RuvA were essentially similar to the FRET values obtained for the untreated HJ (Figures 3.4c & 3.4d), validating our conclusion from Figure 3.7b that the binding of RuvA is unaffected by the formation of cisplatin-DNA adduct.
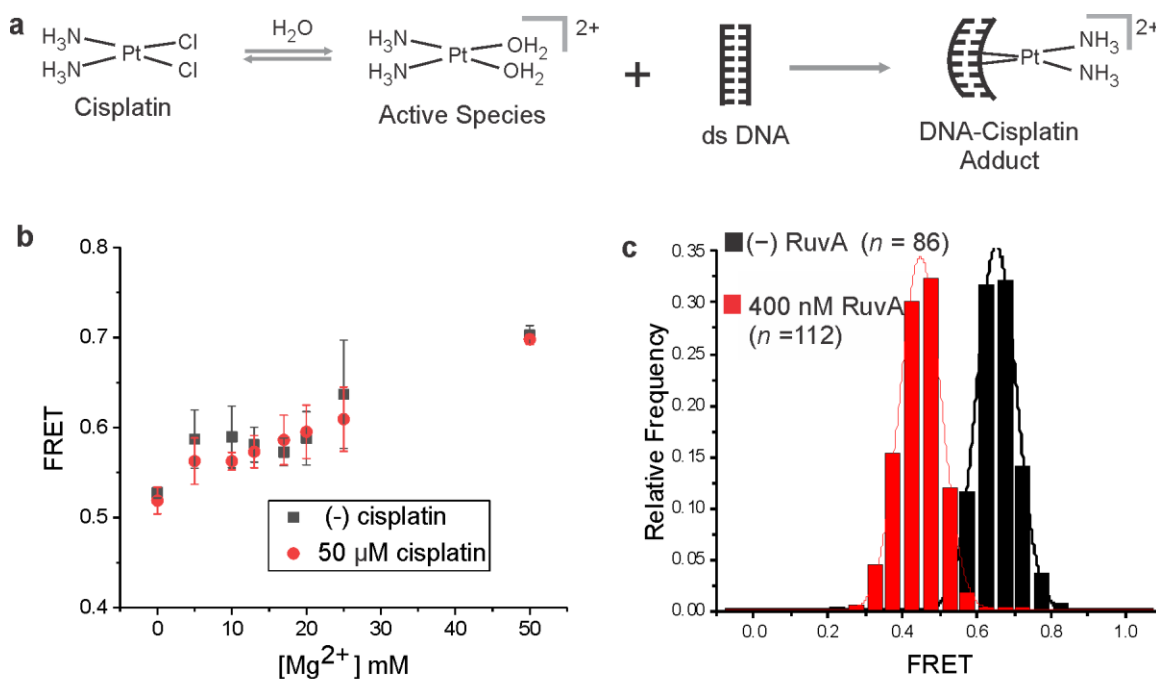
Figure 3.7 Probing the binding of RuvA to the cisplatin-modified HJ. (a) Formation of cisplatin-dsDNA adduct. (b) Bulk FRET at various concentrations of cisplatin. Mg^{2+} titration data from Figure 3 (0 – 50 mM range) were reused for direct comparison with the cisplatin data. Error bars represent standard deviation from three replicate experiments.

(c) smFRET histograms in 50 µM cisplatin under +/- RuvA in 1× TAE buffer (pH 7.4) at 2 mM Mg^{2+} and 137 mM Na^+. The HJ with Labeling Scheme-I was used. The n values in (c) depict the number of single molecule traces in each histogram.
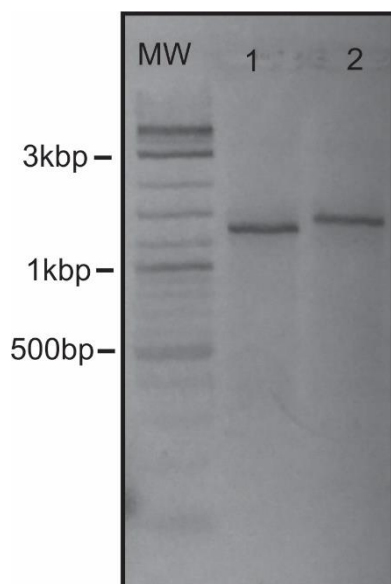
Figure 3.8 Native electrophoretic mobility shift assay (native-EMSA) of the cisplatin-DNA adduct. Lane 1: DNA molecular weight (MW) marker; Lane 2: 1.6-kbp DNA acquired from the polymerase chain reaction (PCR) of pBR322 plasmid DNA8,9; Lane 3: Same DNA as in lane 2 except after incubating with 50 µM cisplatin for 24 hrs.
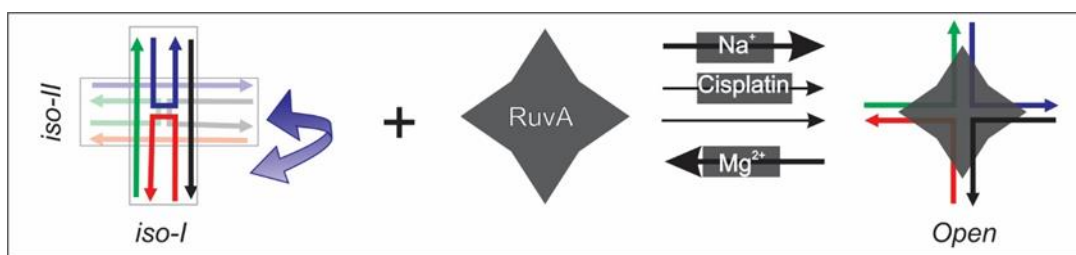
Figure 3.9 Summary of the conformational manipulation and microenvironment-dependent interaction between RuvA and HJ. RuvA halts the conformational dynamics of the HJ and stably clamps its open unstacked conformation. The formation of the RuvA-HJ complex is favored at low concentration of $Mg^{2+.}$ Although the binding interaction is enhanced at high mM concentrations of Na^+, Mg^{2+} provides an opposite effect due to electrostatic shielding. The cisplatin modification of the HJ has no observable effect in the binding interaction between RuvA and HJ.

Conclusions

3.4   In this study, we exploited the unique ability of smFRET to visualize the conformational manipulation of the HJ by the junction processing protein RuvA. Through single molecule and ensemble analyses of the HJ and RuvA-HJ complex, we have revealed several key factors governing the interaction and stability of the complex (Figure 3.9). First, RuvA brings the conformational dynamics of the HJ to a halt upon formation of the RuvA-HJ complex. Our finding provides mechanistic understanding of the previously overlooked molecular details of the binding interaction between the dynamic HJ and RuvA. In general, considering the dynamic characteristics of the junction are critically important in understanding how other HR enzymes interact with the junction. Toward determining the primary mode of interaction, our Mg^{2+} titration experiment reinforced that the RuvA binds to the HJ through electrostatic interaction. In addition, the higher binding efficiency of RuvA to the HJ in the presence of Na^+ suggests that RuvA-mediated recombination is highly sensitive to ionic environments (Figure 3.9).

Because the HJ is a potent target for therapeutic applications, we investigated the binding interaction between RuvA and HJ using a commonly used chemotherapeutic drug cisplatin. Since cisplatin introduces positive charges on DNA and changes its topology,[90,101] we expected that the binding of RuvA would be disrupted upon formation of the cisplatin-HJ adduct. Our finding that the binding is not interrupted by the formation of cisplatin-DNA adduct suggests that RuvA accommodates for the cisplatin-introduced charges/topological changes on the HJ. In the future, it will be interesting to study how therapeutically relevant compounds (such as peptides) interfere with the HJ dynamics as a way to develop antimicrobial drugs. Therefore, our study has the potential to open a

quest for new drugs that can selectively inhibit the HR process by selective targeting of the HJ.

Reprint authorization

Chapter 4 : Direct unfolding of RuvA-HJ complex at the single-molecule level

4.1 Introduction

As described in previous chapters, homologous recombination (HR) is a well conserved pathway that cells use to repair double stranded DNA breaks that has been discussed at length in previous chapters.[109,110] In the late states of HR, the HJ is resolved – by RuvAB-catalyzed branch migration and RuvC-catalyzed cleavage – into mature recombinant double-stranded DNA (dsDNA) molecules.[111,112] Since this repair machinery manipulates DNA during HR, determining the mechanical properties of these enzymes is critical for in-depth understanding of the repair mechanism. While early stages of HR involving RecBCD have been studied in great detail[71,113–115], the mechanical stability and mechanism(s) of late-stage HR are poorly understood.

In the late-stage of HR, RuvA binds and stabilizes the junction during the exchange of nucleotides between DNA strands and prepares it for branch migration (BM); powering the BM process by recruiting RuvB to form an ATP-dependent motor, RuvAB.[21,31,61,111,116] The binding of RuvA to the HJ has been demonstrated before using both bulk biochemical[10] and single-molecule methods.[61] The X-ray analysis of the RuvA-HJ complex showed that RuvA assembles into a tetramer complex which then binds to the HJ with a possibility of two tetramers sandwiching the HJ and creating an octameric shell.[15] The formation of dual tetramer complexes has also been reported in other studies including biochemical and electron microscopy methods.[13,117] Using fluorescence resonance energy transfer (FRET)-based single-molecule analysis of an immobile HJ that was labeled with a FRET pair, we previously showed that the protein clamps the HJ into

a planar conformation, which is otherwise dynamic.[61] Although the stacked (X) conformations of the HJ are the predominant species under physiological ionic conditions[47,118,119], the open form of the junction appears to be the one involved in almost every aspect of the junction processing by resolvases[119] – making the mechanistic analysis of the RuvA-HJ complex highly relevant. Force-based single molecule studies have studied either a bare double-hairpin structure (also called cruciform) alone[120] or the BM process by RuvAB[27,111], not the binding of the enzymes themselves to the HJs.[30] Herein, using dual-trap optical tweezers, we report the first mechanochemical study of the RuvA-HJ complex.

Using optical-tweezers based mechanical manipulation, we were able to unfold a double hairpin motif (DHM, as this is analogous to HJ we will refer to as HJ hereafter) with and without the RuvA protein at the single-molecule level. By stretching the RuvA-HJ complex in solution, we observed that the HJ requires a significantly higher force to unfold. To our surprise, we also observed that RuvA provides stabilization that permits refolding of the HJ at a force higher than the unfolding force of the HJ without protein. This observation suggests that RuvA stays bound to the DNA construct even after unfolding of the HJ motif, may serve as a nucleation site for HJ refolding, and reduces the energy required for HJ refolding. Such mechanistic information that we derived from single-molecule analysis could not be acquired using traditional ensemble methods such as X-ray crystallography and bulk biochemical approaches. Further, the single-molecule platform that we employed for studying the HJ-RuvA system can be easily used to investigate other HJ-binding proteins such as Rad51B, Gen1, and Mus81, providing unprecedented mechanistic insights into the critical DNA repair process.

Materials and Methods

Materials.

All of the DNA oligonucleotides used in this study were purchased from Integrated DNA Technologies (IDT, Coralville, IA), enzymes (Phusion Taq polymerase and T4 DNA ligase) were purchased from New England Biolabs (NEB, Ipswich, MA), chemicals (>95% in purity) were purchased from VWR (West Chester, PA) and Fisher. Glass capillaries for the flow cell were purchased from King Precision Glass (Claremont, CA). The surface functionalized beads for the single-molecule experiments were obtained from Spherotech (Lake Forest, IL). RuvA from *E. coli* was purchased from abcam (Cambridge, MA) and diluted to the desired concentration for experimentation.

Preparation of dsDNA handles.

The two dsDNA fragments that sandwich the HJ segment were prepared via autosticky polymerase chain reaction (PCR) (30) of pBR322 using the Phusion High Fidelity Polymerase (New England BioLabs, Ipswich, MA), which enabled each fragment to retain a 15 nucleotide (nt) single-stranded sticky end. The detailed sequences are provided in Table S1. Fragment 1 (2405 bp) was prepared using the Fragment-1 primer to introduce a sticky end and end-labeled with digoxigenin using a 5′-digoxigenin modified primer (Dig Primer). Fragment 2 (1806 bp) was prepared using the Fragment-2 primer to introduce the sticky end and end-labeled with biotin using a 5′-end biotinylated primer (Biotin Primer). The PCR preparations for both handles were subjected to a cleanup process using the Qiagen PCR purification kit. The fragment preparations were verified by a 1% native agarose gel, which was prepared and run for 60 min at 85V in a 1× TAE (40 mM Tris, 20 mM acetic acid, 1 mM EDTA) running buffer.

Construct annealing and ligation.

The central portion (top and bottom strands of either the HJ or the dsDNA control) was slow annealed (95°C to 4°C) at a final concentration of 10 µM in 1× TAE with 12 mM MgCl$_2$. The sequence detail is provided in the Supplementary Information (Table 4.1). Further, the fully annealed center portion and the two PCR fragments were thermally annealed (50°C to 4°C) at a 1:1:1 molar ratio in 1× ligase buffer (New England BioLabs, Ipswich, MA) to allow the sticky ends of the handles to hybridize with their complementary overhangs on the center portion. The middle portion of the DNA construct was ligated to the DNA handles with T4 DNA ligase and 1 mM ATP by incubating the mixture at 16 ℃ for 16 hrs. A 1% agarose gel was run to verify the success of the ligation as stated previously.

Table 4.1 Sequences for all of the DNA oligonucleotides (oligos) used in assembling the DNA constructs for optical tweezers. All biotin and digoxigenin labeled DNA oligos were purchased HPLC purified. Autosticky PCR generated sticky ends and their complementary sequences are highlighted in cyan (Fragment 1) and red (Fragment 2). The stem part of the HJ sequences are underlined and the loop regions are bolded. Please see Supplementary Figure 1 for example attachments. (TEG = triethylene glycol used as a linker and idSp = internal abasic site, HP = hairpin)

Name	Sequence (5' → 3')
Fragment1 Primer	/5Phos/CTT GCG TAG TAG CTG /idSp/GAT TTT GGT CAT GAG ATT ATC AAA AAG G
Fragment2 Primer	/5Phos/CTT CGT ACG TTA GCC /idSp/GGA TTT TGG TCA TGA GAT TAT CAA AAA GG
Biotin Primer	/5BiotinTEG/CAT TAG GAA GCA GCC CAG TAG TAG G
Dig Primer	/5DigN/CAG ACA AGG TAT AGG GCG GCG CCT AC
HJ Top	/5Phos/GGC TAA CGT ACG AAG CGA ATG TGT GTC T<u>CA ATC CCA ACT TCA ATC CCA ACT T</u>**TT TTT**<u>AAG TTG GGA TTG AAG TTG GGA TTG</u> TCT GTG TGT AAG C
HJ Bottom	/5Phos/CAG CTA CTA CGC AAG GCT TAC ACA CAG A<u>GG TTA GGG TGA GGT TAG GGT GA A</u>**TT TTT**<u>TTC ACC CTA ACC TTC ACC CTA ACC</u> AGA CAC ACA TTC G
dsDNA Top	/5Phos/GGC TAA CGT ACG AAG GCT ACA GAC GGA GAC GCG CTG GC
dsDNA Bottom	/5Phos/CAG CTA CTA CGC AAG GCC AGC GCG TCT CCG TCT GTA GC
HP Top (single HP)	/5Phos/GGC TAA CGT ACG AAG <u>CAA TCC CAA CTT CAA TCC CAA CTT</u> **TTT TT**<u>A AGT TGG GAT TGA AGT TGG GAT TGC</u> GAA TGT GTG TCT GCT AGC TCT GTG TGT AAG C
HP Top – Staple	/5Phos/CAG CTA CTA CGC AAG GCT TAC ACA CAG AGC TAG CAG ACA CAC ATT CG

Flow cell preparation for optical tweezers experiment.

A flow cell is composed of a pre-cleaned standard glass slide (75 × 26 × 1 mm) with

three holes drilled at each shorter edge using a diamond tipped drill bit, a glass coverslip

64

(24 x 60 mm, Fisher Scientific), capillary tubes (20 μm inner diameter), parafilm, pipette tips (200 μL capacity), and tubing (0.02 inch ID, 0.06 inch OD, Cole-Palmer, Vernon Hills, IL). The drilled slides were scrubbed using a thick paste of Alconox and water, rinsed with deionized water, acetone, and ethanol successively before using. The flow cell was then assembled by cutting out three channels into parafilm, where each channel can encompass two opposing drilled holes (Figure 4.1). Two ~1 cm long capillary tubes were placed at ~45° angles to connect the outer sample channels to the central buffer channel such that solutions from the outer channels would flow into the central channel in a controlled manner (Figure 4.1). The channels were then covered with a coverslip and the flow cell was heated at 95℃ for 5 min on both faces to seal the cell. Pipette tips cut to ~1 cm each were inserted into each of the drilled holes and plumed with ~40 cm long tubing. The tips and the tubing were secured using Double Bubble Quick-Set epoxy from Hardman Adhesives.
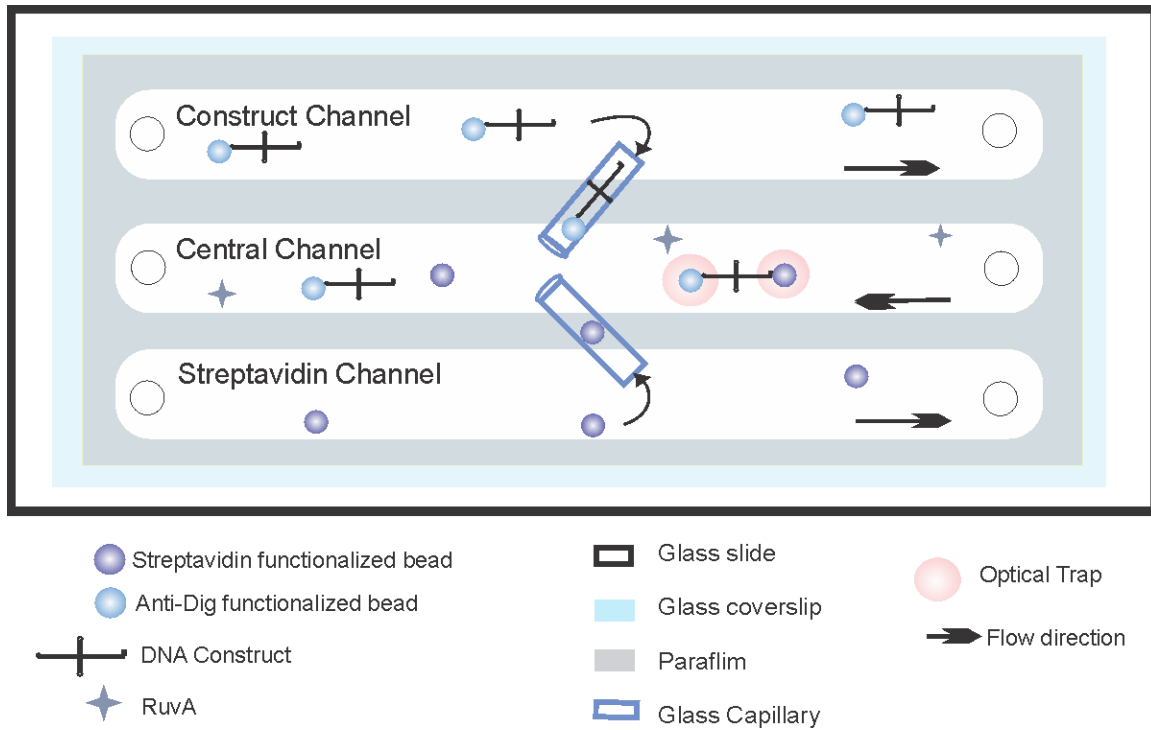
Figure 4.1 Assembly of the three-channel flow cell for optical tweezers experiments: glass slide in black (note the holes in the slide where tubing are inserted), with a glass coverslip in blue, sandwiched between these layers is a parafilm layer with channels cut to allow the flow of buffer and beads. Note the direction of flow is staggered and the capillary tubes are positioned diagonally. The DNA construct bound to Anti-Dig antibody coated beads were suspended in the buffer of the construct channel, streptavidin-coated beads were suspended in the streptavidin channel, and RuvA was dissolved in the central channel. Optical traps were used to pick one of each type of bead and bring them in close proximity to facilitate binding of the construct to the streptavidin bead. Manipulation experiments were then carried out in the central channel in an area free of other beads.

Optical Tweezers Experiments.

All experiments were conducted using a dual-beam optical tweezers setup (NanoTracker-2) purchased from JPK Instruments, Santa Barbara, CA. A 1064 nm continuous wave, 3W, laser beam was split to create two optical traps with an adjustable power ratio, one of these traps is movable using a steerable mirror while the other is fixed. In order to acquire data, the fully ligated DNA construct was first immobilized onto anti-digoxigenin antibody coated polystyrene beads (diameter of ~2 µm, Spherotech) in 1×

PBS via antibody/antigen interaction. The complex was allowed to form by gently tapping the solution for 5 min followed by a 10 min incubation at room temperature before injecting into the flow cell. Separately, a solution of streptavidin coated polystyrene beads (diameter of ~3 µm, Spherotech) was also prepared in the same buffer and injected into the second sample channel. Each bead was separately trapped in individual optical traps in the central buffer channel and calibrated separately for the trap stiffness using the JPK built-in single-button calibration procedure. Then the beads were brought into close proximity to tether the DNA construct to the streptavidin bead via biotin/streptavidin interaction. Once tethered, the mobile trap was used to stretch the DNA at a constant pulling rate of 38 nm/s (~13 pN/s) while the displacement of the beads was monitored by a quadrant photodiode (QPD). The buffer channel contained either 1× PBS buffer for experiments without RuvA or 1× PBS along with RuvA (30 nM) for protein binding experiments. Protein concentration was kept lower than its dissociation constant (Kd) to minimize possible non-specific binding to DNA handles. *F-X* curves were collected across various molecules and on various days for each experiment. The change in Gibbs free energy of unfolding (*ΔG*<area>) was determined by measuring the area under the rupture event (plateau) of the *F-X* curves using the built-in area-under-the-curve (AUC) analysis program on the JPK software. All uncertainties presented are population standard deviations from the mean.

4.3

Results and Discussion

In this study, we first designed and then prepared a DNA construct suitable for optical tweezers. This construct is composed of a HJ analog consisting of a double hairpin motif (DHM, which we call HJ for simplicity hereafter) flanked by dsDNA handles. To enable

67

the mechanical stability analysis of the RuvA-HJ complex on a simpler platform, we used an immobile junction created by the use of non-identical sequences in the opposite arms to avoid possible complication by branch migration (movement of the crossover point along the DNA axis). The handles were end-functionalized with a biotin on one end and a digoxigenin on the other for tethering between a pair of surface-functionalized beads (Figure 4.2 A) to enable manipulation on the optical tweezers. This construct was prepared through polymerase chain reaction (PCR) of the pBR322 plasmid using biotin and digoxigenin-modified primers. The primers were designed to generate single-stranded sticky ends (15 nt in length) without the use of restriction enzymes via a process called auto-sticky PCR.[121] Briefly, using a primer with 2 abasic sites in-between the primer sequence and the sticky-end sequence and a more sensitive error checking polymerase, the auto-sticky PCR allows generating a single-stranded sticky end. The dsDNA handles generated were then ligated with a HJ central portion assembled by thermal annealing of synthetic DNA strands (Figure 4.2 A). The HJ was designed to have poly-thymine loops (TTTT) to allow for repeated pulling of the same DNA molecule on the optical tweezers (Figure 4.3). The formation of DNA handles as well as the desired final DNA construct was confirmed by running an agarose gel. The slower migration of the DNA band obtained after three-piece ligation (two PCR fragments and a central HJ portion) confirmed the formation of the DNA construct (Figure 4.2 B). A control construct without the HJ was prepared similarly using three-piece ligation of the same PCR fragments after replacing the HJ portion with a dsDNA fragment.
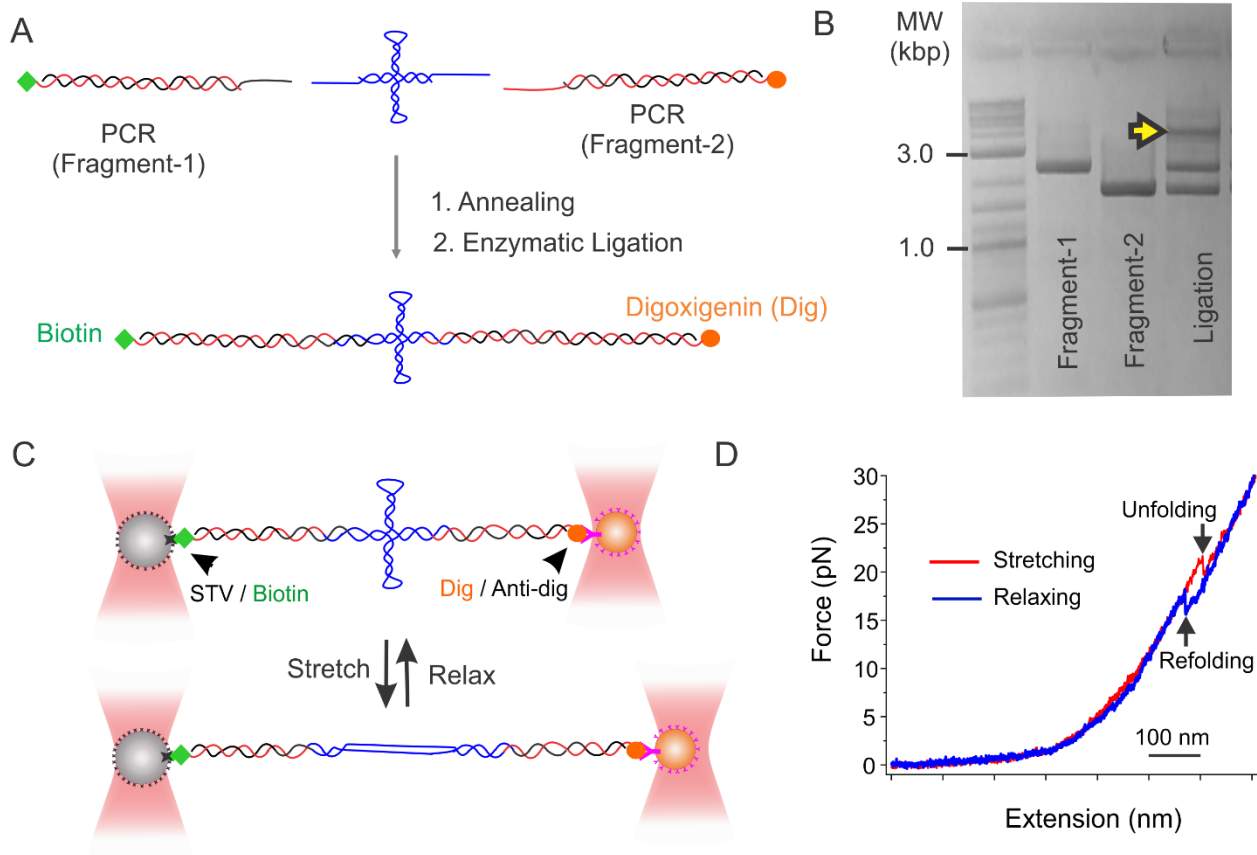
Figure 4.2. Preparation and characterization of DNA construct. (A) Flow chart illustrating the key steps involved in the making of the DNA constructs, which includes generation of two DNA fragments via PCR and annealing and ligation of these fragments with immobile HJ central portion obtained by annealing of synthetic ssDNAs. Biotin and digoxigenin were incorporated to the opposite ends of the DNA construct via modified primers. (B) Agarose gel characterization of the full-length DNA construct (4305bp). The DNA fragments from purified PCR are shown in lanes 1 and 2 and the product of the three-piece ligation (two PCR fragments along with HJ central portion) using T4 DNA ligase is shown in lane 3. The ligated product is highlighted with an arrow. (C) Schematic of optical tweezers set up. The DNA is tethered between the two surface-functionalized beads via streptavidin/biotin linkage on one end and digoxigenin /anti-digoxigenin antibody on the other. The HJ analog is highlighted in purple, which can reversibly unfold/refold during mechanical stretch/relax cycle. (D) Typical force vs extension (*F-X*) curve for the HJ construct with the HJ unfolding/refolding events. Note the unfolding and refolding events, which correspond to the melting and rehybridization of the HJ, indicated with arrows.

HJ Top

ATC GGCTAACGTACGAAGCGAATGTGTGTCT TCTGCGCGCAAGCCTTGCGTAGTAGCTG--GGA

TAG--CCGATTGCATGCTTCGCTTACACACAGA AGACGCGCGTTCGGAACGCATCATCGAC CCT
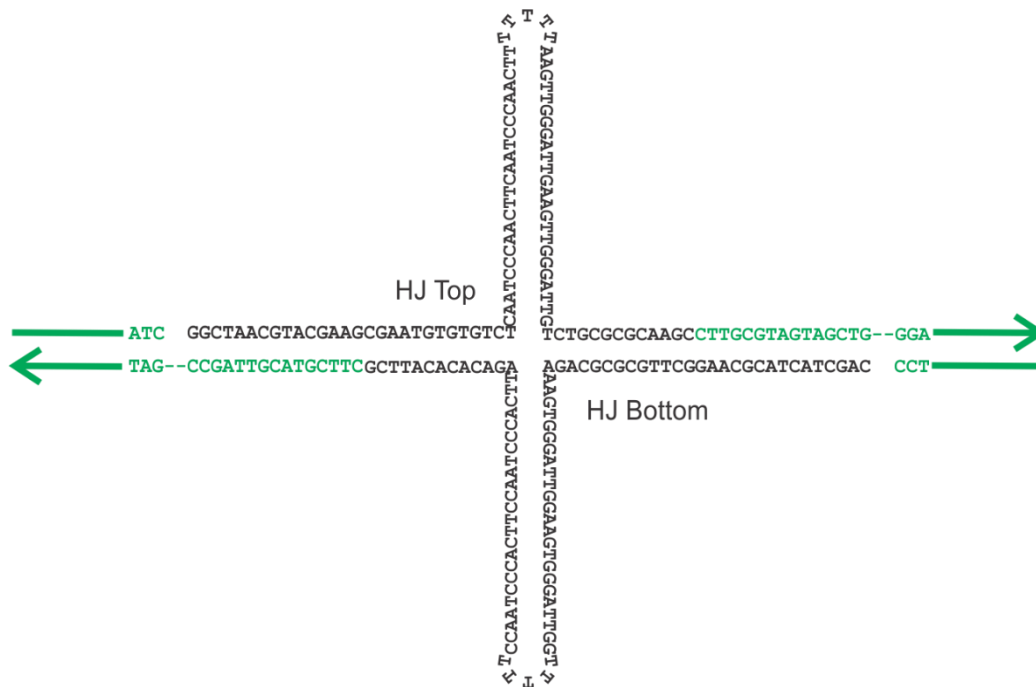
HJ Bottom

Figure 4.3 Assembly of HJ analogous double hairpin motif (DHM) from strands HJ Top and HJ Bottom (Supplementary Table S1). DNA fragments from autosticky PCR are depicted in green. Note that non-homologous sequences were used to generate immobile HJ. A poly-T (5′-TTTTT) loop was incorporated in both the top and bottom strands to enable repeated pulling of the DNA molecule.

Prior to optical tweezers experiments, the DNA construct was incubated with anti-digoxigenin functionalized polystyrene beads (Spherotech, Lake Forest, IL) for 15 min, resulting in surface immobilization of DNA constructs onto the beads. These beads as well as streptavidin-functionalized beads were injected into the flow cell via separate channels, which merge into a central channel via a small (~120 μm in diameter) glass capillary to direct the beads in a controlled manner. The two types of beads were trapped individually in two separate optical traps (Figure 4.2 C). The trapped beads were then brought into close proximity to allow the free biotin end of DNA construct to bind to the streptavidin-functionalized bead. This setup allowed us to manipulate the individual HJ constructs in a highly controlled manner, which we performed both in the presence and absence of RuvA.

70

Using tweezers, we first manipulated the HJ constructs (Figure 4.2 D) and a dsDNA control (Figure 4.4). The dsDNA control was identical to the HJ construct in terms of length and sequence except that the HJ part was replaced with a dsDNA fragment. All experiments were carried out in PBS buffer (137 mM NaCl, 2.7 mM KCl, 10mM Na_2HPO_4, 1.8 mM KH_2PO_4) at room temperature at a pulling rate of 38 nm s-1 ($\approx$ 13 pN s-1), which falls well within the range of commonly used rates.[122–125] Stretching of the dsDNA control gave *F-X* curves with no feature of note, with dsDNA melting occurring at ~65 pN (Fig. 4.4), the observation of a plateau at ~65 pN represents the force-induced melting of a single molecule of dsDNA.[126,127] When the HJ construct was manipulated, we observed a very distinct unfolding event at ~20 pN similar to that of a hairpin unfolding (Fig. 4.2 D).[128] When the HJ DNA molecule was relaxed, there was a clear refolding event with a small hysteresis on the *F-X* curve. We also prepared and tested another control construct containing a single hairpin DNA(Fig. 4.5). Typical *F-X* curves obtained from this experiment are shown in Fig. S4. As expected, an unfolding event was observed at ~8-10 pN range, which is approximately half of the unfolding force observed for the HJ. The analysis of those *F-X* curves showed that the hairpin undergoes a dynamic switching between the folded and unfolded state at around 8-10 pN force, however it was difficult to accurately determine the *ΔL* due to the dynamics. We observed a *ΔL* of ~23 nm in some curves with a relatively large unfolding event, which is close to the expected *ΔL* value for a 54-nt hairpin (~27 nm assuming the contour length of 0.5 nm per nucleotide). Together, these results support that the rupture event observed at ~20 pN (~ twice the *F*unfold of the hairpin) when using the HJ construct is due to the unfolding of the HJ.
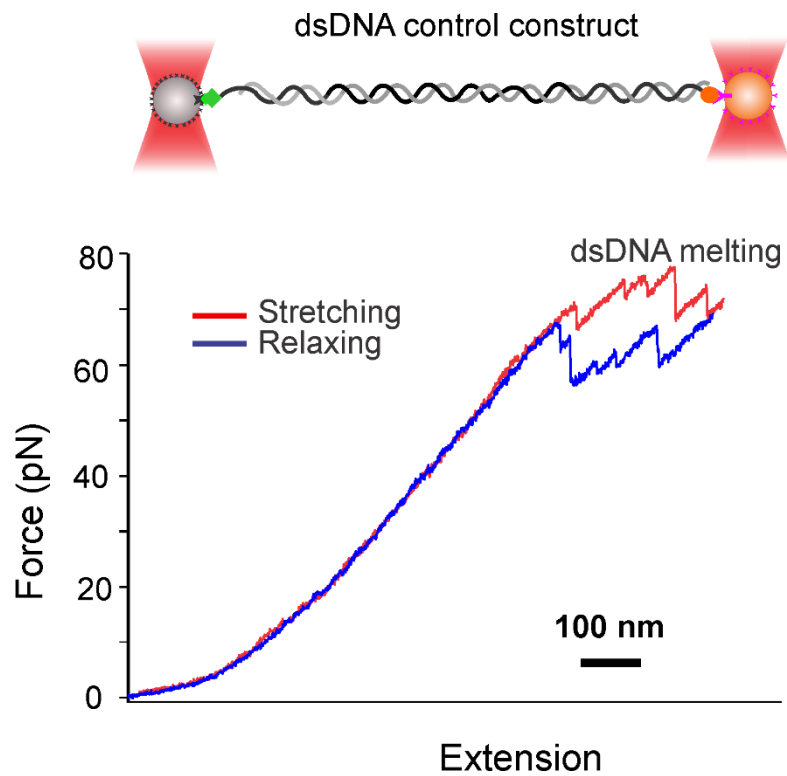
Figure 4.4 Typical *F-X* curve for dsDNA control without HJ. Note that the DNA melting occurs at ~65 pN. Small jumps represent local melting of small sections of DNA, which reanneal upon relaxing the DNA molecule.
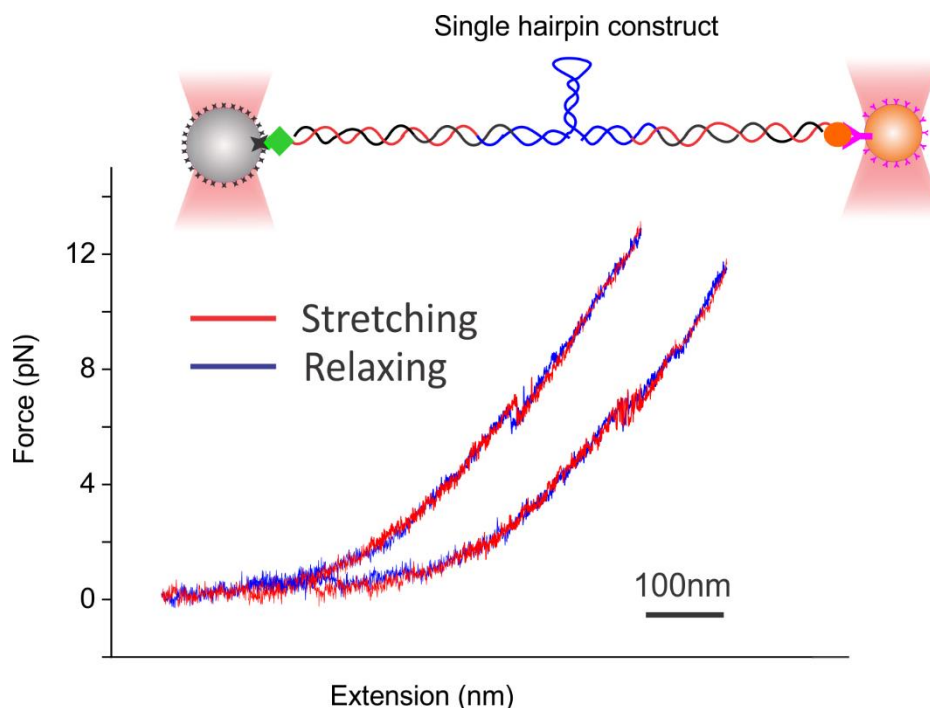
Figure 4.5 Typical *F-X* curves for the single hairpin construct. Note the unfolding feature at ~8-10 pN with either a clear unfolding event (left curve) or dynamic switching around the unfolding force (right curve).

Inspired by this observation, we repeated the stretching of the HJ construct to collect many *F-X* curves from several single-molecules. The unfolding/refolding behavior of the HJ was highly reproducible (Fig. 4.6 A). When RuvA (30 nM) was added to the buffer and optical tweezers experiments were repeated, interestingly, we mainly observed two-step unfolding (Fig. 4.6 B), which is contrary to the one-step unfolding of the HJ in the absence of protein. While the first small unfolding event occurred at around the unfolding force of HJ alone, the second unfolding event was very distinct and shifted to a higher force (~39 pN) (Fig. 4.6 B). Similarly, the relaxing curve showed two-step refolding events one at around 36 pN and another at around 12 pN. Further, none of these features were observed when using a dsDNA construct (control) in the presence of RuvA (30 nM) (Fig. 4.7). The *F-X* curves showing such two-step unfolding/refolding features in the presence

of RuvA make up ~90% of the total curves. The remaining 10% of curves showed either unfolding/refolding feature similar to HJ without RuvA (unbound population) or unfolding at ~39 pN but refolding occurred at a much lower force (~10-15 pN, further discussed later). Although the *F-X* curves in the presence of RuvA are noisier than those without (we believe this may be due to transient binding to the dsDNA arms of the construct though RuvA has at least 20-fold higher affinity to the HJ than to dsDNA)[86,88], the unfolding features were clear to determine extension due to unfolding of the RuvA-HJ complex. Specifically, the *F-X* curves with unfolding/refolding transitions forming a clear hysteresis between the stretching and relaxing curves were selected for further analysis. This criterion is justified as the hysteresis observed in the presence of RuvA were different from HJ-alone experiment and there was no hysteresis in the control dsDNA construct with and without RuvA (Figs. 4.4 and 4.7). The low-force refolding event was also clear in ~40% of the total curves collected, and hence the curves exhibiting clear low-force unfolding features were used in Fig. 4.8.
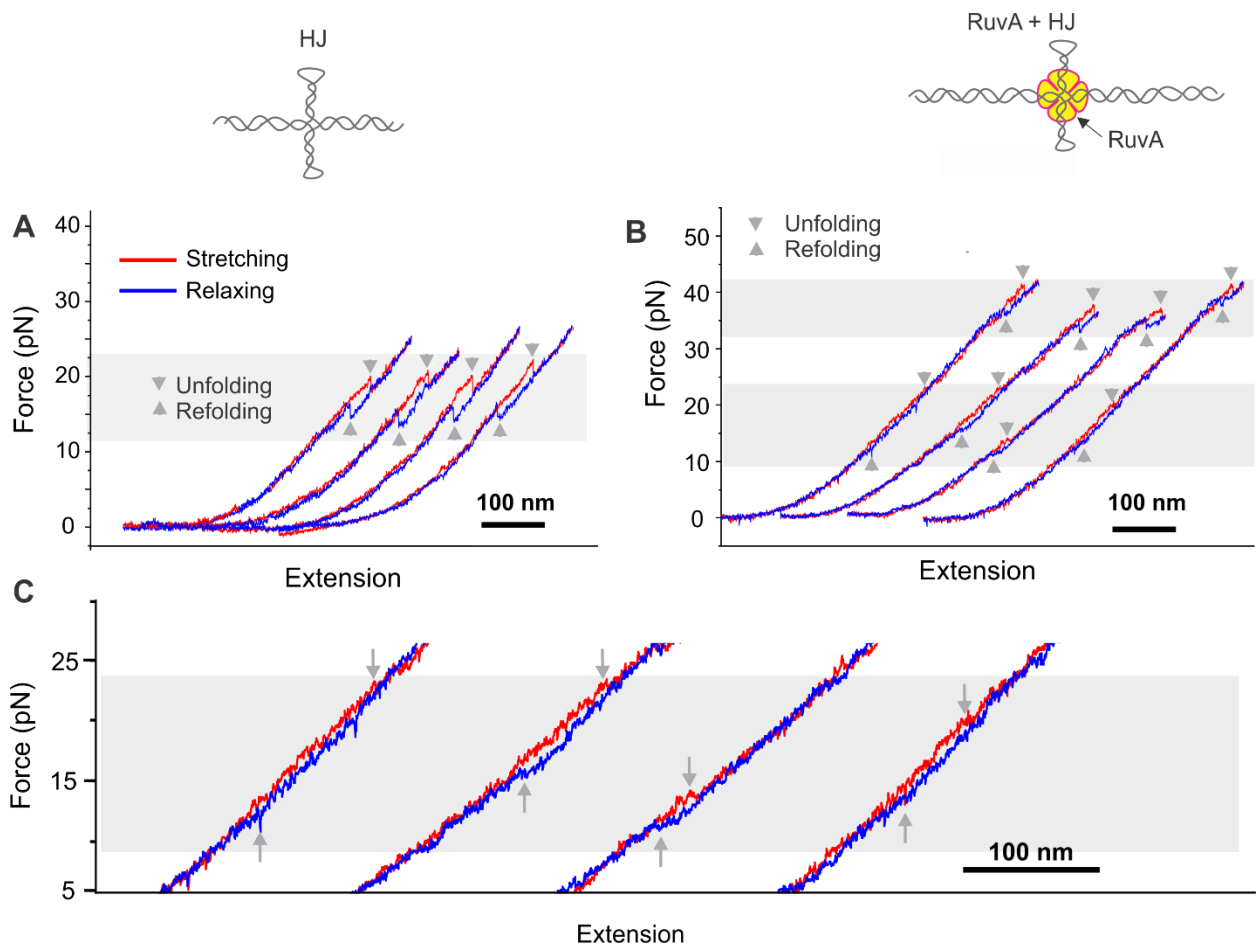
Figure 4.6 Typical force-extension (*F-X*) curves for the HJ alone (A) and for the HJ in the presence of RuvA (B). Several curves are shown to demonstrate the reproducibility of observation. The *F-X* curves are shifted horizontally for clarity. The unfolding/refolding portion of the curves is highlighted with a shaded-grey background. The *F-X* curves for RuvA-HJ showed two unfolding events, one small feature at around 10-22 pN range and another more obvious unfolding feature at around 40 pN. The smaller feature is highlighted in a zoomed-in view (C). The observation of a clear hysteresis due to the unfolding and refolding events between the stretching and relaxing curve respectively allowed us to visually pick these transitions.
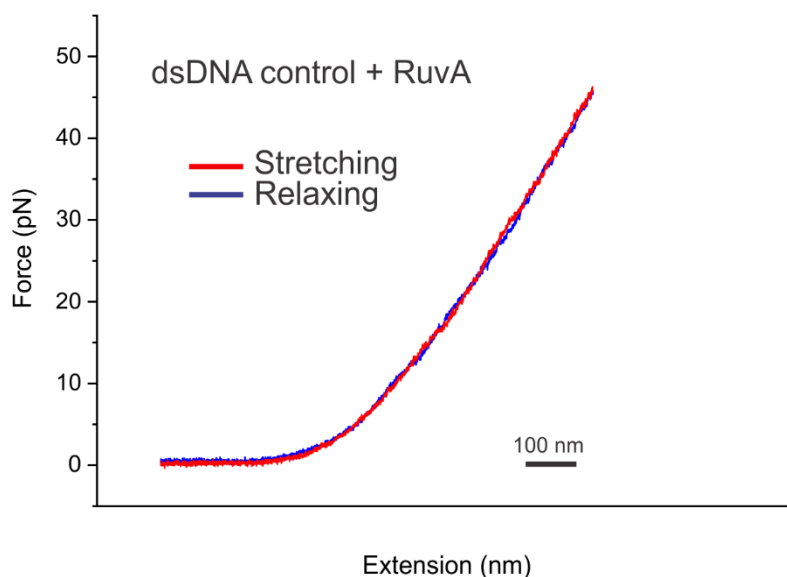
Figure 4.7 A typical *F-X* curve for the dsDNA + RuvA (30 nM) control experiment. Note that there is a lack of any distinct features.

When we plotted the histogram for the F_{unfold} of HJ (n = 130 pulls), it showed a Gaussian distribution with the mean F_{unfold} of 19.9 ± 2.5 pN and F_{Refold} of 10.8 ± 3.6 pN (Fig. 4.8 A). Similar analysis of the data for RuvA-HJ experiments (n = 50 pulls) showed that the mean unfolding and refolding force for the major populations resided on 39.0 ± 2.6 pN and 36.9 ± 3.9 pN, respectively (Fig. 4.8 B). The pattern of behavior observed in the *F-X* curves was endemic of the stabilization of the HJ by the RuvA tetramer(s). Altogether, the stretching/relaxing *F-X* curves acquired in the presence of RuvA showed a few interesting details about the RuvA-HJ interactions. Firstly, the two unfolding events were clear from the force histograms. And, the small unfolding event occurring near the HJ-unfolding force suggests that RuvA does not significantly alter the stability of the inner part of the HJ but stabilizes its outer part.[129–131]
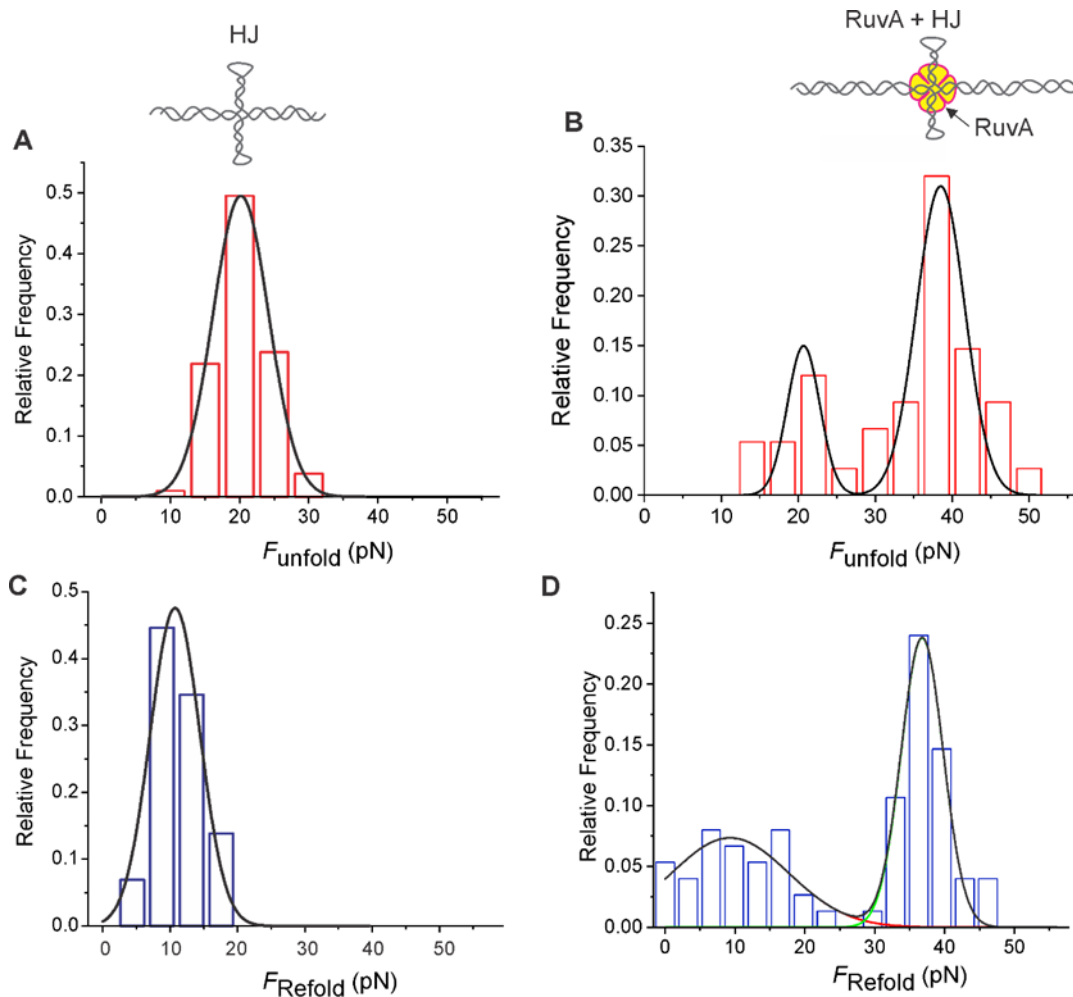
Figure 4.8 Force histograms. (A) Unfolding (top) and refolding (bottom) force histogram for HJ only (n = 130). (B) Unfolding (top) and refolding force histograms in the presence of RuvA (30 nM, n = 50). The value of 'n' represents the total number of *F-X* curves used in this data set. The number of single molecules used for the analysis of HJ and RuvA-HJ complex were 31 and 11, respectively with a maximum of 8 unfolding/refolding events per molecule. The black curve represents Gaussian fitting of the data.

It is noteworthy that the distribution of this low-force population is quite broad. After the detailed analysis of unfolding force and associated extension due to unfolding (discussed later), we surmised that the low-force population is comprised of both RuvA-bound and unbound molecules. This is expected due to the stochastic nature of single-molecules with a small fraction of RuvA-unbound molecules. Second, the F_{unfold} of about ~39 pN, which is about 2-fold higher than that of the HJ alone, demonstrated that the

77

RuvA protein stabilizes the HJ through its interactions with the double helical arms. Although our experiment does not provide the structural details of binding interactions, it can be imagined that the HJ either slips through RuvA or the RuvA tetramer(s) fully dissociate at high force.

The resulting extension (Δx) at a given force was then converted to the change-in-contour length (*ΔL*) using the Worm-Like-Chain (WLC) model. Though we have some non-dsDNA character in our construct, the use of the extensible WLC (Eq 4.1) is well established for constructs with secondary structure that is much shorter than the dsDNA handles (<5%).[132–134] Further the use of this approximation is justified for DNA stretching with high-force unfolding features.

$$\frac{\Delta x}{\Delta L} = 1 - \frac{1}{2}\left(\frac{k_B T}{FP}\right)^{\frac{1}{2}} + \frac{F}{S} \ldots\ldots\ldots\ldots(4.1)$$

Where *ΔL* represents the apparent change in contour length at F = 0 pN, kB is the Boltzmann constant, T is the absolute temperature, F is the force, P is the persistence length (46 ± 9 nm) and S is the elastic stretch modulus (1466 ± 54 pN).[133–135] Persistence length and elastic stretch modulus were determined by fitting of typical curves using an extensible WLC model (Figure 4.9). Before applying the WLC model, all of the *F-X* curves were corrected for the bead-to-bead distance that accounts for the optical tweezers stiffness. The *ΔL* histogram for HJ showed a Gaussian distribution with a mean *ΔL* of 21.6 ± 2.7 nm (Fig. 4.10 A). For HJ + RuvA change in contour length was determined by adding *ΔL*s for high force and low force events on an individual curve, these events showed Gaussian distribution with a mean *ΔL* of 24.9 ± 3.1 nm (Fig. 4.10 B). From these

histograms, it is clear that there is a broad distribution of both the low- and high-force ΔLs

in the presence of RuvA.
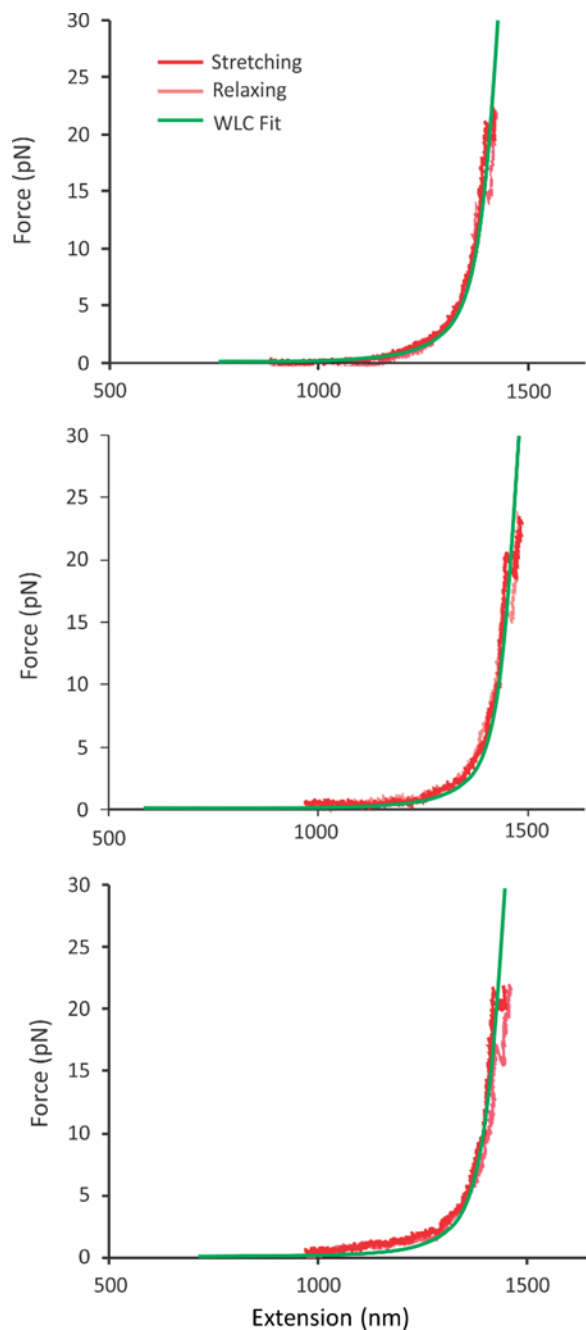
Figure 4.9 Representative WLC-fitted curves with the corrected bead-to-bead distance for the HJ DNA construct. The stretching curves were fitted. The parameters obtained from the extensible WLC fitting were as follows: DNA contour length (Lo) = 1456 ± 16 nm, persistence length (P) = 46 ± 9 nm, and stretch modulus (S) = 1466 ± 54 pN. The Lo value is consistent with the expected contour length for 4305 bp DNA construct and the

S and P values are consistent with the literature reported parameters for the given ion strength.

These results suggest that, rather than a simple HJ unfolding event, some multi-step process involving partial breaking of RuvAs binding to the HJ is occurring. Potentially, the first step is the unzipping of the arms of the junction perpendicular to the direction of pull and then the second event results from the pull through of the remaining portion of the hairpins disrupting the RuvA-HJ interaction. Such two-step unfolding has been observed before for the Cas12a-R-loop complex.[136] The broad distribution of ΔLs also suggests that the number of base pairs that would open at low force varies from molecule to molecule, followed by the unfolding of the remaining base-pairs at high force. This argument is supported by the fact that the sum of the low- and high-force ΔLs of individual molecules (24.9 ± 3.1 nm) with clear and measurable two-step unfolding agrees well with the mean ΔL of HJ alone (Fig. 4.10 B). The observed ΔL falls within the expected range of unfolded HJ motif. The exact extension due to unfolding of the HJ cannot be estimated purely in terms of the length of the ssDNA strands that will result when the hairpins are melted as there are two strands running parallel to one another after unfolding. Therefore, the estimated length of the 53 bp linear section that makes up the unfolded HJ motif was calculated using standard contour length of 0.34 nm/bp in dsDNA and maximum contour length of ~0.69 nm/nucleotide in ssDNA. This range of values (18 to 37 nm) was taken to be the potential range of extension possible based on the physical makeup of the HJ. A slightly higher ΔL for the protein binding experiment may be attributed to melting of the stretched dsDNA arms (handle side) with the partially bound RuvA. Further investigations will be required to clarify this hypothesis.
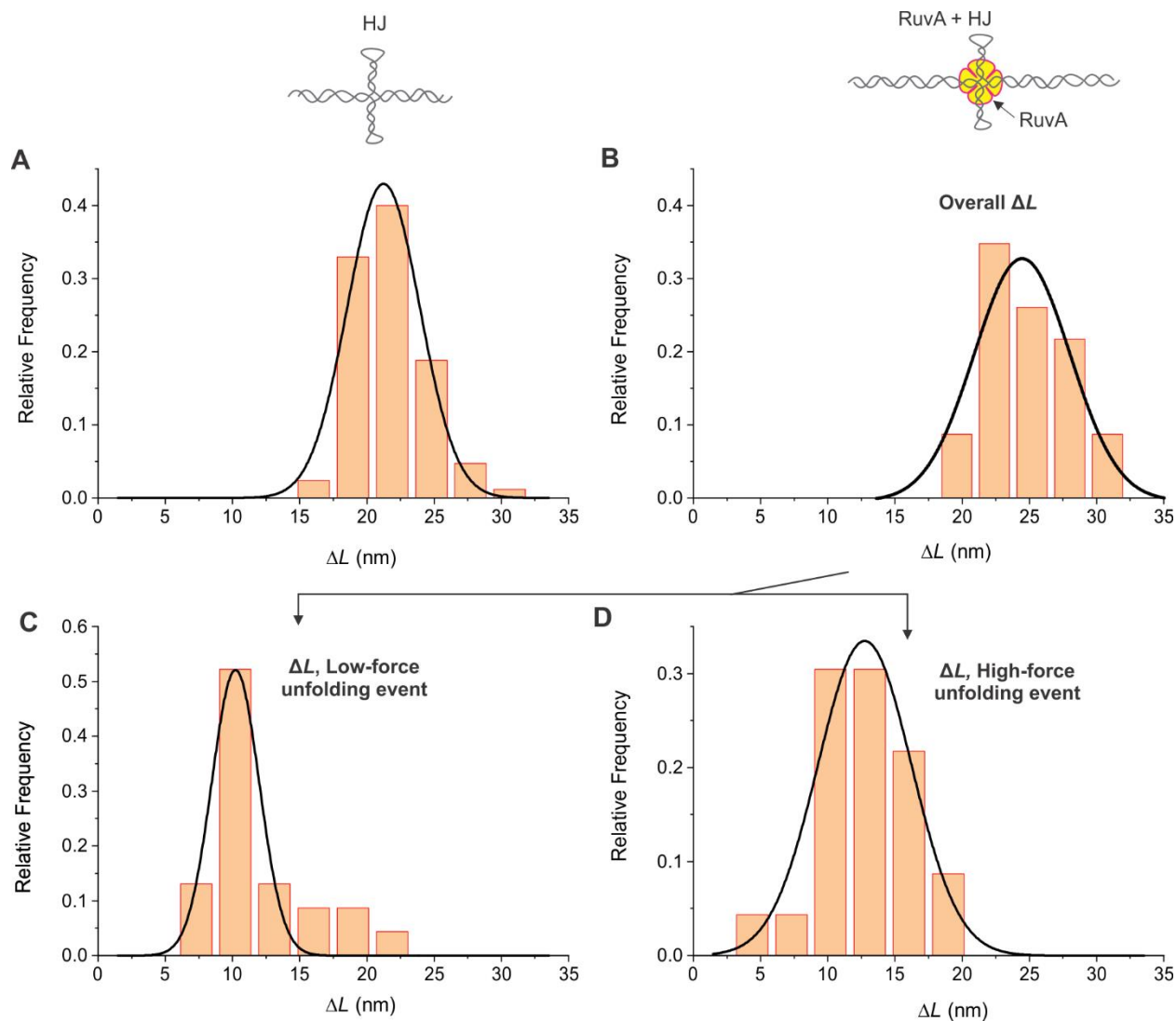
Figure 4.10 Change in contour length (*ΔL*) due to unfolding of HJ alone (n = 86) (A) or in the presence of RuvA (n = 25) (B, C, & D). (B) is the total of the individual *ΔL* values of the two unfolding events on each +RuvA *F-X* curve. These individual event values are separated into low-force (C) and high-force (D) histograms. The *ΔL* value was obtained from the change-in-extension (Δx) due to unfolding of the HJ at a given force using equation 1. The black curves represent Gaussian fit of the data.

We then determined the change in Gibbs free energy of unfolding for the bound and unbound states by measuring the area under the unfolding plateau (*ΔG*<area>, Figure 4.11) as described before.[137–139] These analyses showed that the rupturing of the HJ had a *ΔG*<area> of 54 kcal/mol. This number agrees well with the predicted stability of the HJ as determined by mFold (*ΔG*mfold = 58 kcal mol-1, Figure 4.12) [140]. In order to estimate

the free energy change of unfolding (ΔG_{unfold}) of the HJ, we determined the ΔG of the individual hairpin portions that make up the double hairpin motif using mFold (UNA-fold) at experimental concentration of Na$^+$ ion (137 mM). These hairpins are the underlined and bolded portions of HJ Top and HJ Bottom sequence in the Table 4.1 . The individual ΔG values add up to 58 kcal/mol. The experimental ΔG value derived from the area under the rupture event measured directly on the *F-X* curves is in agreement with the mFold-estimated ΔG In the presence of RuvA, the ΔG<area> was increased to 101 kcal/mol demonstrating that RuvA stabilizes the junction by ~2-fold (Table 4.2).
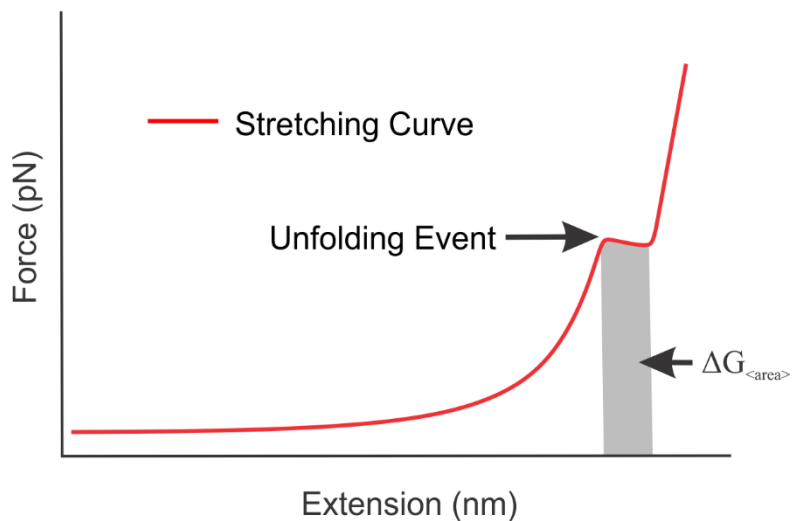
Figure 4.11 Visualization of the way the ΔG<area> was determined. The red curve represents a stretching curve with an unfolding event occurring as a plateau. The gray area under the unfolding event represents the area under the curve (AUC) selected to represent the ΔG<area>.
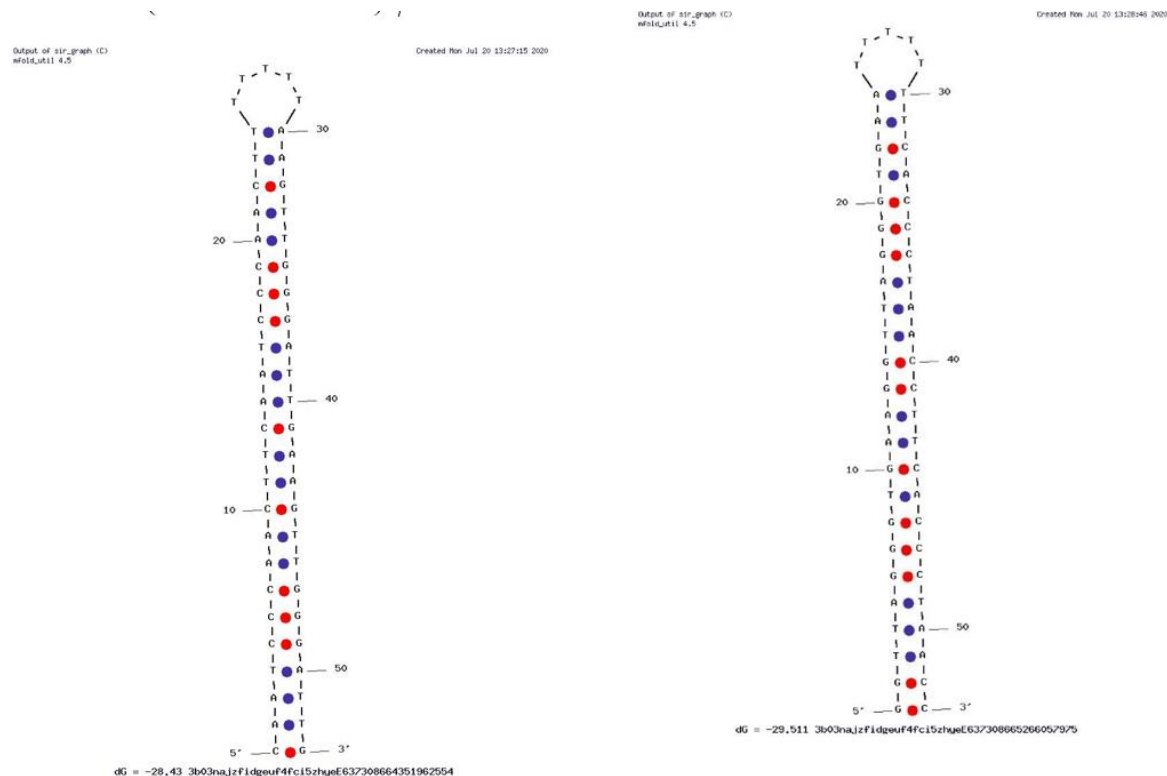
$\Delta G = 28.43$ kcal/mol $\Delta G = 29.51$ kcal/mol

Figure 4.12 mFold predicted hairpins and the corresponding *ΔG* values. Left: mfold predicted hairpin for the HJ Top (*ΔG* = 28.43 kcal/mol), Right: mfold predicted hairpin for the HJ Bottom (*ΔG* = 29.51 kcal/mol). The sequence detail for the HJ is depicted in Supplementary Figure S1.

Table 4.2 Summary of unfolding force (F_{unfold}), *ΔL*, and free energy change of unfolding (*ΔG*) of HJ alone (n = 86) and RuvA-bound HJ (n = 25). F1 and F2 represent the mean unfolding force for the low- and high-force unfolding events in the presence of RuvA. Values in parenthesis represent standard deviations. N/A = Not Applicable.

Species	*F unfold* (*F, pN*)		*ΔL* (*L, nm*)	*ΔG$_{<area>}$* (*kcal mol^{-1}*)	*ΔG$_{mFold}$* (*kcal mol^{-1}*)
HJ	*19.9 (±2.5)*		*21.6 (±2.7)*	*54 (±13)*	*58*
RuvA + HJ	*F$_1$*	*F$_2$*	*L$_{Total}$*	*ΔG$_{<area>}$*	*N/A*
	19.1 (±3.9)	*39.0 (±2.6)*	*24.9 (±3.1)*	*101 (±20)*	*N/A*

Our observation that the HJ undergoes force-induced melting and refolding at high force for ~90% of the molecules suggests that RuvA remains bound to the construct and assists refolding of the HJ (Type-I, Figure 4.13 B). A small fraction of F-X curves in the presence of RuvA showed unfolding at a high force and refolding at a low force suggesting a complete dissociation of RuvA (Type-II, Figure 4.13 B).
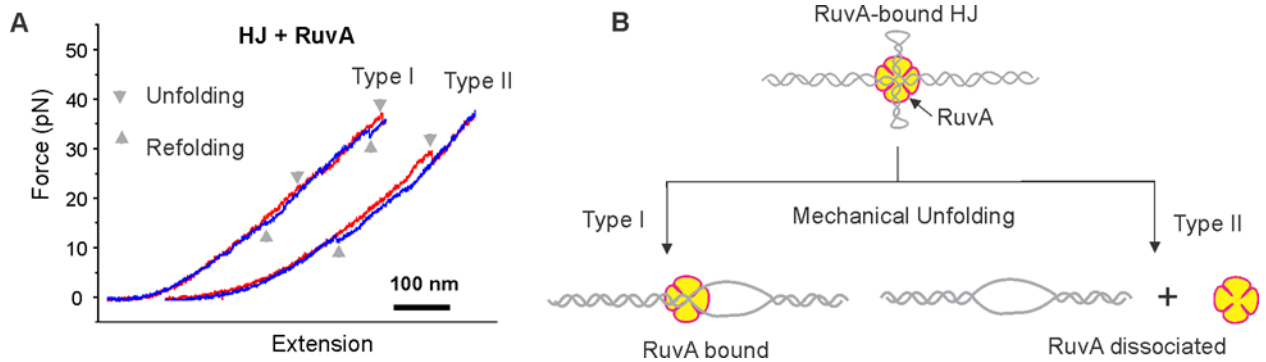
Figure 4.13 (A) Two types of F-X curves observed for RuvA-HJ complex. Type I curve represents two-step unfolding whereas Type II curve represents one-step unfolding of HJ. (B) Plausible model for the RuvA-HJ interaction based on Type I and Type II unfolding events. In Type I, the refolding event occurs at a higher force than that of the HJ alone, suggesting RuvA-assisted refolding of the HJ (88% population). This observation also suggests that the protein RuvA remains bound to the mechanically stretched DNA at least up to ~39 pN. In contrast, Type II refolding occurs at a similar force level to the HJ alone, indicating the full dissociation of protein from the DNA in a small fraction of molecules (~8%). In addition, a small fraction (~4%) of molecules showed only the low-force (~20 pN) unfolding event consistent with HJs with no bound RuvA.

4.4   Conclusions

In summary, we present mechanical unfolding of the RuvA-HJ complex at the single molecule level revealing several mechanistic insights of this protein-DNA complex. First, we successfully implemented an autosticky PCR approach for a rapid and efficient preparation of DNA constructs for optical tweezers. The unfolding experiments showed that, upon RuvA binding and formation of the RuvA-HJ complex, the F_{unfold} of HJ increases significantly. The higher F_{unfold} of the complex shows that the HJ forms a stable complex

84

with RuvA. In addition, we observed a bi-modal unfolding of the HJ, which suggests that RuvA binds less strongly to the inner part of the HJ (cause for the lower-force unfolding event of ~10 nm step) but interacts strongly with the outer part possibly via a helix-pin-helix motif (Fig 4.13 B).[116] However, it is noteworthy that the *ΔL* distribution of these lower- and higher-force unfolding features may rely on the sequence composition of the HJ. The refolding data also showed very interesting insights that the RuvA remains bound to the DNA even after unfolding of the HJ and helps it refold back to the HJ structure at a much higher force than that of the unfolding force of the HJ itself. Analyses of free energy of unfolding (ΔG_{unfold}) suggests that the RuvA stabilizes the HJ by about 2-fold. The data together provided insights into the binding interaction of RuvA and HJ, highlighting the mechanochemical and thermodynamic properties of the critical HR complex responsible for initiating branch migration and HJ resolution. The formation of such a mechanically stable complex may be required to efficiently recruit other proteins such as RuvB and RuvC. These proteins together with RuvA are responsible for branch migration and HJ resolution during the repair of dsDNA breaks via a process called homologous recombination. The single-molecule platform that we employed here for studying the RuvA-HJ interaction can be easily adapted to investigate many other prokaryotic and eukaryotic HJ-binding proteins involved in the critical DNA repair process.

Reprint authorization

Chapter 5 : Conclusions and Summary

In the first project a single molecule total internal reflectance fluorescence microscope was assembled and characterized with a Holliday junction isomerization experiment. This process was detailed in a published paper to enable members of the scientific community who wish to build a TIRF to do so with relative ease.[141] In the second project that microscope and Holliday Junction system was utilized to study the effect that the binding of RuvA has on the HJ dynamics and conformation.

In the second project it was revealed that the Holliday junction's conformational dynamics was stalled upon binding of RuvA, and the FRET results suggest that the junction adopts an open cruciform conformation in the RuvA-HJ complex. The experiments with Mg^{2+} demonstrated that the RuvA-HJ interaction was highly dependent on the electrostatic interactions between the junction and protein. Further experiments with cisplatin indicated that the junction-RuvA interaction is tolerant of topological changes in the HJ. These molecular insights led to the third project - the direct unfolding of the HJ-RuvA complex at the single molecule level.

In the final (third) project, we revealed that upon binding of RuvA to the Holliday junction, the unfolding force required to rupture the junction-RuvA complex was much higher than that of the HJ alone. Further the dissociation of the RuvA tetramers from the HJ occurs in a two-step process. The calculated ΔG of the RuvA-HJ complex was twice that of the HJ alone, further confirming the high stability of the RuvA-HJ complex.

This work has opened a broad research path to study many other HJ-binding proteins and resolvases at the molecular level. A logical next step would be the single-

molecule analysis of the RuvA-RuvB-HJ complex using optical tweezers. This experiment would allow us to determine the stability of the RuvA-RuvB-HJ complex, which can lead to mechanistic insights such as stepwise formation and dissociation of the complex in addition to the protein-protein interactions (PPIs) between RuvA and RuvB. Another future direction would be to look into the binding of eukaryotic HJ-binding proteins such as Rad51B and Rad54 using both smFRET and optical tweezers. These experiments could reveal insights into the bound shape of the HJ as well as the stability of the HJ-protein complexes. For example, a HJ construct similar to ones used in the smFRET and optical tweezers projects above but with homology sequences so that they are suitable for studying branch migration (BM) kinetics with and without proteins. A DNA construct can be easily designed and used to study how HJ-binding proteins such as RuvA and Rad51B modulate the BM kinetics. The construct can also be used to study ATP-dependent BM motor - Rad54 alone or in conjunction with other Rad54 interacting proteins such as BLM. Further, the optical tweezers platform that we developed here to study HJ-RuvA interactions can also be used to screen ligands (such as HJ-binding peptides and small molecules). This could aid in the development of drugs that interfere with the HJ-protein complex. Overall this work has added significantly to the toolbox available to scientists to study Holliday junction resolvases and to explore its potential for therapeutics.

In summary, I have detailed the construction of a single molecule total internal reflectance fluorescence microscope and used that microscope to implement single molecule FRET to study the HJ-RuvA interaction. In doing so I was able to demonstrate the conformational manipulation of the HJ by RuvA. Through this study I also determined

the nature of RuvA-HJ interaction using an electrostatic shielding environment (Mg^{2+} ion), and the effect that DNA modifying drug cisplatin had on RuvA binding. Using optical tweezers I was able to measure the stabilizing energy of the RuvA-HJ complex. In doing so I was able to visualize the binding and probe the molecular-level details of this protein-DNA complex, which would be instrumental in studying larger complexes such as RuvAB and RuvABC in prokaryotes and eventually other HR complexes in eukaryotes.

References

(1) Alberts, B.; Bray, D.; Hopkin, K.; Johnson, A.; Lewis, J.; Raff, M.; Roberts, K.; Walter, P. *Essential Cell Biology*; Garland Science, 2010.

(2) Chatterjee, N.; Walker, G. C. Mechanisms of DNA Damage, Repair and Mutagenesis. *Environ Mol Mutagen* **2017**, *58* (5), 235–263. https://doi.org/10.1002/em.22087.

(3) Li, X.; Heyer, W.-D. Homologous Recombination in DNA Repair and DNA Damage Tolerance. *Cell Research* **2008**, *18* (1), 99–113. https://doi.org/10.1038/cr.2008.1.

(4) Aplan, P. D. Causes of Oncogenic Chromosomal Translocation. *Trends Genet* **2006**, *22* (1), 46–55. https://doi.org/10.1016/j.tig.2005.10.002.

(5) Ranjha, L.; Howard, S. M.; Cejka, P. Main Steps in DNA Double-Strand Break Repair: An Introduction to Homologous Recombination and Related Processes. *Chromosoma* **2018**, *127* (2), 187–214. https://doi.org/10.1007/s00412-017-0658-1.

(6) Carvalho, J. F.; Kanaar, R. Targeting Homologous Recombination-Mediated DNA Repair in Cancer. *Expert Opinion on Therapeutic Targets* **2014**, *18* (4), 427–458. https://doi.org/10.1517/14728222.2014.882900.

(7) Camerini-Otero, R. D.; Hsieh, P. Homologous Recombination Proteins in Prokaryotes and Eukaryotes. *Annual Review of Genetics* **1995**, *29* (1), 509–552. https://doi.org/10.1146/annurev.ge.29.120195.002453.

(8) Kaniecki, K.; Tullio, L. D.; Greene, E. C. A Change of View: Homologous Recombination at Single-Molecule Resolution. *Nature Reviews Genetics* **2018**, *19* (4), 191–207. https://doi.org/10.1038/nrg.2017.92.

(9) Gibbs, D. R.; Dhakal, S. Homologous Recombination under the Single-Molecule Fluorescence Microscope. *International Journal of Molecular Sciences* **2019**, *20* (23), 6102. https://doi.org/10.3390/ijms20236102.

(10) Parsons, C. A.; Tsaneva, I.; Lloyd, R. G.; West, S. C. Interaction of Escherichia Coli RuvA and RuvB Proteins with Synthetic Holliday Junctions. *Proc Natl Acad Sci U S A* **1992**, *89* (12), 5452–5456.

(11) West, S. C. PROCESSING OF RECOMBINATION INTERMEDIATES BY THE RuvABC PROTEINS. *Annu. Rev. Genet.* **1997**, *31* (1), 213–244. https://doi.org/10.1146/annurev.genet.31.1.213.

(12) Liu, Y.; Masson, J.-Y.; Shah, R.; O'Regan, P.; West, S. C. RAD51C Is Required for Holliday Junction Processing in Mammalian Cells. *Science* **2004**, *303* (5655), 243–246. https://doi.org/10.1126/science.1093037.

(13) Bradley, A. S.; Baharoglu, Z.; Niewiarowski, A.; Michel, B.; Tsaneva, I. R. Formation of a Stable RuvA Protein Double Tetramer Is Required for Efficient Branch Migration in Vitro and for Replication Fork Reversal in Vivo. *J Biol Chem* **2011**, *286* (25), 22372–22383. https://doi.org/10.1074/jbc.M111.233908.

(14) Yamada, K.; Miyata, T.; Tsuchiya, D.; Oyama, T.; Fujiwara, Y.; Ohnishi, T.; Iwasaki, H.; Shinagawa, H.; Ariyoshi, M.; Mayanagi, K.; Morikawa, K. Crystal Structure of the RuvA-RuvB Complex: A Structural Basis for the Holliday Junction Migrating Motor Machinery. *Molecular Cell* **2002**, *10* (3), 671–681. https://doi.org/10.1016/S1097-2765(02)00641-X.

(15) Roe, S. M.; Barlow, T.; Brown, T.; Oram, M.; Keeley, A.; Tsaneva, I. R.; Pearl, L. H. Crystal Structure of an Octameric RuvA–Holliday Junction Complex. *Molecular Cell* **1998**, *2* (3), 361–372. https://doi.org/10.1016/S1097-2765(00)80280-4.

(16) Aravind, L.; Anantharaman, V.; Balaji, S.; Babu, M. M.; Iyer, L. M. The Many Faces of the Helix-Turn-Helix Domain: Transcription Regulation and Beyond⋆. *FEMS Microbiology Reviews* **2005**, *29* (2), 231–262. https://doi.org/10.1016/j.fmrre.2004.12.008.

(17) Roy, R.; Hohng, S.; Ha, T. A Practical Guide to Single-Molecule FRET. *Nature Methods* **2008**, *5* (6), 507–516. https://doi.org/10.1038/nmeth.1208.

(18) Kim, S. H.; Ragunathan, K.; Park, J.; Joo, C.; Kim, D.; Ha, T. Cooperative Conformational Transitions Keep RecA Filament Active During ATPase Cycle. *Journal of the American Chemical Society* **2014**, *136* (42), 14796–14800. https://doi.org/10.1021/ja506363y.

(19) Galletto, R.; Amitani, I.; Baskin, R. J.; Kowalczykowski, S. C. Direct Observation of Individual RecA Filaments Assembling on Single DNA Molecules. *Nature* **2006**, *443* (7113), 875–878. https://doi.org/10.1038/nature05197.

(20) Lu, C.-H.; Yeh, H.-Y.; Su, G.-C.; Ito, K.; Kurokawa, Y.; Iwasaki, H.; Chi, P.; Li, H.-W. Swi5–Sfr1 Stimulates Rad51 Recombinase Filament Assembly by Modulating Rad51 Dissociation. *Proceedings of the National Academy of Sciences* **2018**, *115* (43), E10059–E10068. https://doi.org/10.1073/pnas.1812753115.

(21) Iwasa, T.; Han, Y.-W.; Hiramatsu, R.; Yokota, H.; Nakao, K.; Yokokawa, R.; Ono, T.; Harada, Y. Synergistic Effect of ATP for RuvA–RuvB–Holliday Junction DNA Complex Formation. *Scientific Reports* **2015**, *5*, 18177. https://doi.org/10.1038/srep18177.

(22) Zhou, R.; Yang, O.; Déclais, A.-C.; Jin, H.; Gwon, G. H.; Freeman, A. D. J.; Cho, Y.; Lilley, D. M. J.; Ha, T. Junction Resolving Enzymes Use Multivalency to Keep the Holliday Junction Dynamic. *Nat Chem Biol* **2019**, *15* (3), 269–275. https://doi.org/10.1038/s41589-018-0209-y.

(23) Gao, D.; Ding, W.; Nieto-Vesperinas, M.; Ding, X.; Rahman, M.; Zhang, T.; Lim, C.; Qiu, C.-W. Optical Manipulation from the Microscale to the Nanoscale: Fundamentals, Advances and Prospects. *Light: Science & Applications* **2017**, *6* (9), e17039–e17039. https://doi.org/10.1038/lsa.2017.39.

(24) Moffitt, J. R.; Chemla, Y. R.; Smith, S. B.; Bustamante, C. Recent Advances in Optical Tweezers. *Annu. Rev. Biochem.* **2008**, *77* (1), 205–228. https://doi.org/10.1146/annurev.biochem.77.043007.090225.

(25) Neuman, K. C.; Block, S. M. Optical Trapping. *Rev Sci Instrum* **2004**, *75* (9), 2787–2809. https://doi.org/10.1063/1.1785844.

(26) Ashkin, A. Optical Trapping and Manipulation of Neutral Particles Using Lasers. *PNAS* **1997**, *94* (10), 4853–4860. https://doi.org/10.1073/pnas.94.10.4853.

(27) Forth, S.; Deufel, C.; Patel, S. S.; Wang, M. D. Direct Measurements of Torque During Holliday Junction Migration. *Biophysical Journal* **2011**, *101* (2), L5–L7. https://doi.org/10.1016/j.bpj.2011.05.066.

(28) Bustamante, C.; Alexander, L.; Maciuba, K.; Kaiser, C. M. Single-Molecule Studies of Protein Folding with Optical Tweezers. *Annu. Rev. Biochem.* **2020**, *89* (1), 443–470. https://doi.org/10.1146/annurev-biochem-013118-111442.

(29) McKinney, S. A.; Déclais, A.-C.; Lilley, D. M. J.; Ha, T. Structural Dynamics of Individual Holliday Junctions. *Nature Structural Biology* **2003**, *10* (2), 93–97. https://doi.org/10.1038/nsb883.

(30) Long, X.; Parks, J. W.; Stone, M. D. Integrated Magnetic Tweezers and Single-Molecule FRET for Investigating the Mechanical Properties of Nucleic Acid. *Methods* **2016**, *105*, 16–25. https://doi.org/10.1016/j.ymeth.2016.06.009.

(31) Dawid, A.; Croquette, V.; Grigoriev, M.; Heslot, F. Single-Molecule Study of RuvAB-Mediated Holliday-Junction Migration. *PNAS* **2004**, *101* (32), 11611–11616. https://doi.org/10.1073/pnas.0404369101.

(32) Kozuka, J.; Yokota, H.; Arai, Y.; Ishii, Y.; Yanagida, T. Dynamic Polymorphism of Single Actin Molecules in the Actin Filament. *Nat Chem Biol* **2006**, *2* (2), 83–86. https://doi.org/10.1038/nchembio763.

(33) Ha, T.; Rasnik, I.; Cheng, W.; Babcock, H. P.; Gauss, G. H.; Lohman, T. M.; Chu, S. Initiation and Re-Initiation of DNA Unwinding by the *Escherichia Coli* Rep Helicase. *Nature* **2002**, *419* (6907), 638–641. https://doi.org/10.1038/nature01083.

(34) Poulter, N. S.; Pitkeathly, W. T. E.; Smith, P. J.; Rappoport, J. Z. The Physical Basis of Total Internal Reflection Fluorescence (TIRF) Microscopy and Its Cellular Applications. In *Advanced Fluorescence Microscopy: Methods and Protocols*; Verveer, P. J., Ed.; Methods in Molecular Biology; Springer New York: New York, NY, 2015; pp 1–23. https://doi.org/10.1007/978-1-4939-2080-8_1.

(35) Millis, B. A. Evanescent-Wave Field Imaging: An Introduction to Total Internal Reflection Fluorescence Microscopy. In *Molecular Profiling: Methods and Protocols*; Espina, V., Liotta, L. A., Eds.; Methods in Molecular Biology; Humana Press: Totowa, NJ, 2012; pp 295–309. https://doi.org/10.1007/978-1-60327-216-2_19.

(36) Axelrod, D.; Burghardt, T. P.; Thompson, N. L. Total Internal Reflection Fluorescence. *Annual Review of Biophysics and Bioengineering* **1984**, *13* (1), 247–268. https://doi.org/10.1146/annurev.bb.13.060184.001335.

(37) Yildiz, A.; Vale, R. D. Total Internal Reflection Fluorescence Microscopy. *Cold Spring Harb Protoc* **2015**, *2015* (9), pdb.top086348. https://doi.org/10.1101/pdb.top086348.

(38) Ma, H.; Fu, R.; Xu, J.; Liu, Y. A Simple and Cost-Effective Setup for Super-Resolution Localization Microscopy. *Scientific Reports* **2017**, *7* (1), 1542. https://doi.org/10.1038/s41598-017-01606-6.

(39) Fish, K. N. Total Internal Reflection Fluorescence (TIRF) Microscopy. *Curr Protoc Cytom* **2009**, *0 12*, Unit12.18. https://doi.org/10.1002/0471142956.cy1218s50.

(40) Walter, N. G.; Huang, C.-Y.; Manzo, A. J.; Sobhy, M. A. Do-It-Yourself Guide: How to Use the Modern Single Molecule Toolkit. *Nat Methods* **2008**, *5* (6), 475–489. https://doi.org/10.1038/nmeth.1215.

(41) Diao, J.; Ishitsuka, Y.; Lee, H.; Joo, C.; Su, Z.; Syed, S.; Shin, Y.-K.; Yoon, T.-Y.; Ha, T. A Single Vesicle-Vesicle Fusion Assay for in Vitro Studies of SNAREs and Accessory Proteins. *Nat Protoc* **2012**, *7* (5), 921–934.

(42) Martin-Fernandez, M.; Tynan, C.; Webb, S. A 'Pocket Guide' to Total Internal Reflection Fluorescence. *J Microsc* **2013**, *252* (1), 16–22. https://doi.org/10.1111/jmi.12070.

(43) Heintzmann, R. A Appendix: Practical Guide to Optical Alignment. In *Fluorescence Microscopy*; Wiley-Blackwell, 2013; pp 393–401. https://doi.org/10.1002/9783527671595.app1.

(44) Joo, C.; Ha, T. Preparing Sample Chambers for Single-Molecule FRET. *Cold Spring Harb Protoc* **2012**, *2012* (10), pdb.prot071530. https://doi.org/10.1101/pdb.prot071530.

(45) Ha, T.; Zhuang, X.; Kim, H. D.; Orr, J. W.; Williamson, J. R.; Chu, S. Ligand-Induced Conformational Changes Observed in Single RNA Molecules. *Proc Natl Acad Sci U S A* **1999**, *96* (16), 9077–9082.

(46) Deffeyes, K. S.; Deffeyes, S. E. *Nanoscale: Visualizing an Invisible World*; MIT Press: Cambridge, UNITED STATES, 2011.

(47) Hyeon, C.; Lee, J.; Yoon, J.; Hohng, S.; Thirumalai, D. Hidden Complexity in the Isomerization Dynamics of Holliday Junctions. *Nature Chemistry* **2012**, *4* (11), 907–914. https://doi.org/10.1038/nchem.1463.

(48) Joo, C.; McKinney, S. A.; Lilley, D. M. J.; Ha, T. Exploring Rare Conformational Species and Ionic Effects in DNA Holliday Junctions Using Single-Molecule Spectroscopy. *Journal of Molecular Biology* **2004**, *341* (3), 739–751. https://doi.org/10.1016/j.jmb.2004.06.024.

(49) Smith, G. R. Mechanism and Control of Homologous Recombination in Escherichia Coli. *Annual Review of Genetics* **1987**, *21* (1), 179–201. https://doi.org/10.1146/annurev.ge.21.120187.001143.

(50) Chernikova, S. B.; Game, J. C.; Brown, J. M. Inhibiting Homologous Recombination for Cancer Therapy. *Cancer Biology & Therapy* **2012**, *13* (2), 61–68. https://doi.org/10.4161/cbt.13.2.18872.

(51) van Gent, D. C.; Kanaar, R.; Kellogg, D. Exploiting DNA Repair Defects for Novel Cancer Therapies. *MBoC* **2016**, *27* (14), 2145–2148. https://doi.org/10.1091/mbc.e15-10-0698.

(52) Moynahan, M. E.; Jasin, M. Mitotic Homologous Recombination Maintains Genomic Stability and Suppresses Tumorigenesis. *Nature Reviews Molecular Cell Biology* **2010**, *11* (3), 196–207. https://doi.org/10.1038/nrm2851.

(53) Helleday, T.; Petermann, E.; Lundin, C.; Hodgson, B.; Sharma, R. A. DNA Repair Pathways as Targets for Cancer Therapy. *Nature Reviews Cancer* **2008**, *8* (3), 193–204. https://doi.org/10.1038/nrc2342.

(54) Dunham, M. A.; Neumann, A. A.; Fasching, C. L.; Reddel, R. R. Telomere Maintenance by Recombination in Human Cells. *Nature Genetics* **2000**, *26* (4), 447–450. https://doi.org/10.1038/82586.

(55) Dilley, R. L.; Greenberg, R. A. ALTernative Telomere Maintenance and Cancer. *Trends Cancer* **2015**, *1* (2), 145–156. https://doi.org/10.1016/j.trecan.2015.07.007.

(56) Bryan, T. M.; Englezou, A.; Gupta, J.; Bacchetti, S.; Reddel, R. R. Telomere Elongation in Immortal Human Cells without Detectable Telomerase Activity. *EMBO J.* **1995**, *14* (17), 4240–4248.

(57) Forster, Th. Energiewanderung und Fluoreszenz. *Naturwissenschaften* **1946**, *33* (6), 166–175. https://doi.org/10.1007/BF00585226.

(58) Gordon, G. W.; Berry, G.; Liang, X. H.; Levine, B.; Herman, B. Quantitative Fluorescence Resonance Energy Transfer Measurements Using Fluorescence Microscopy. *Biophys J* **1998**, *74* (5), 2702–2713.

(59) Wouters, F. S.; Verveer, P. J.; Bastiaens, P. I. Imaging Biochemistry inside Cells. *Trends Cell Biol.* **2001**, *11* (5), 203–211.

(60) Jalink, K.; van Rheenen, J. Chapter 7 FilterFRET: Quantitative Imaging of Sensitized Emission. In *Laboratory Techniques in Biochemistry and Molecular Biology*; Fret and Flim Techniques; Elsevier, 2009; Vol. 33, pp 289–349. https://doi.org/10.1016/S0075-7535(08)00007-7.

(61) Gibbs, D. R.; Dhakal, S. Single-Molecule Imaging Reveals Conformational Manipulation of Holliday Junction DNA by the Junction Processing Protein RuvA. *Biochemistry* **2018**, *57* (26), 3616–3624. https://doi.org/10.1021/acs.biochem.8b00404.

(62) Aitken, C. E.; Marshall, R. A.; Puglisi, J. D. An Oxygen Scavenging System for Improvement of Dye Stability in Single-Molecule Fluorescence Experiments. *Biophys. J.* **2008**, *94* (5), 1826–1835. https://doi.org/10.1529/biophysj.107.117689.

(63) Widom, J. R.; Dhakal, S.; Heinicke, L. A.; Walter, N. G. Single-Molecule Tools for Enzymology, Structural Biology, Systems Biology and Nanotechnology: An Update. *Arch Toxicol* **2014**, *88* (11), 1965–1985. https://doi.org/10.1007/s00204-014-1357-9.

(64) Shi, X.; Lim, J.; Ha, T. Acidification of the Oxygen Scavenging System in Single-Molecule Fluorescence Studies: In Situ Sensing with a Ratiometric Dual-Emission Probe. *Anal Chem* **2010**, *82* (14), 6132–6138. https://doi.org/10.1021/ac1008749.

(65) Swoboda, M.; Henig, J.; Cheng, H.-M.; Brugger, D.; Haltrich, D.; Plumeré, N.; Schlierf, M. Enzymatic Oxygen Scavenging for Photostability without PH Drop in Single-Molecule Experiments. *ACS Nano* **2012**, *6* (7), 6364–6369. https://doi.org/10.1021/nn301895c.

(66) Fu, J.; Yang, Y. R.; Dhakal, S.; Zhao, Z.; Liu, M.; Zhang, T.; Walter, N. G.; Yan, H. Assembly of Multienzyme Complexes on DNA Nanostructures. *Nature Protocols* **2016**, *11* (11), 2243–2273. https://doi.org/10.1038/nprot.2016.139.

(67) Suddala, K. C.; Cabello-Villegas, J.; Michnicka, M.; Marshall, C.; Nikonowicz, E. P.; Walter, N. G. Hierarchical Mechanism of Amino Acid Sensing by the T-Box Riboswitch. *Nat Commun* **2018**, *9* (1), 1896. https://doi.org/10.1038/s41467-018-04305-6.

(68) McKinney, S. A.; Joo, C.; Ha, T. Analysis of Single-Molecule FRET Trajectories Using Hidden Markov Modeling. *Biophys J* **2006**, *91* (5), 1941–1951. https://doi.org/10.1529/biophysj.106.082487.

(69) Dhakal, S.; Adendorff, M. R.; Liu, M.; Yan, H.; Bathe, M.; Walter, N. G. Rational Design of DNA-Actuated Enzyme Nanoreactors Guided by Single Molecule Analysis. *Nanoscale* **2016**, *8* (5), 3125–3137. https://doi.org/10.1039/C5NR07263H.

(70) Zhao, Z.; Fu, J.; Dhakal, S.; Johnson-Buck, A.; Liu, M.; Zhang, T.; Woodbury, N. W.; Liu, Y.; Walter, N. G.; Yan, H. Nanocaged Enzymes with Enhanced Catalytic Activity and Increased Stability against Protease Digestion. *Nature Communications* **2016**, *7*, 10619. https://doi.org/10.1038/ncomms10619.

(71) Smith, G. R. How RecBCD Enzyme and Chi Promote DNA Break Repair and Recombination: A Molecular Biologist's View. *Microbiol. Mol. Biol. Rev.* **2012**, *76* (2), 217–228. https://doi.org/10.1128/MMBR.05026-11.

(72) Handa, N.; Yang, L.; Dillingham, M. S.; Kobayashi, I.; Wigley, D. B.; Kowalczykowski, S. C. Molecular Determinants Responsible for Recognition of the Single-Stranded DNA Regulatory Sequence, χ, by RecBCD Enzyme. *PNAS* **2012**, *109* (23), 8901–8906. https://doi.org/10.1073/pnas.1206076109.

(73) Smith, G. R. Homologous Recombination in E. Coli: Multiple Pathways for Multiple Reasons. *Cell* **1989**, *58* (5), 807–809. https://doi.org/10.1016/0092-8674(89)90929-X.

(74) Perkins, T. T.; Li, H.-W.; Dalal, R. V.; Gelles, J.; Block, S. M. Forward and Reverse Motion of Single RecBCD Molecules on DNA. *Biophys J* **2004**, *86* (3), 1640–1648.

(75) Perkins, T. T.; Li, H.-W. Single-Molecule Studies of RecBCD. In *Helicases: Methods and Protocols*; Abdelhaleem, M. M., Ed.; Methods in Molecular Biology; Humana Press: Totowa, NJ, 2010; pp 155–172. https://doi.org/10.1007/978-1-60327-355-8_11.

(76) Brown, M. S.; Bishop, D. K. DNA Strand Exchange and RecA Homologs in Meiosis. *Cold Spring Harb Perspect Biol* **2014**, *7* (1), a016659. https://doi.org/10.1101/cshperspect.a016659.

(77) Heijden, T. van der; Modesti, M.; Hage, S.; Kanaar, R.; Wyman, C.; Dekker, C. Homologous Recombination in Real Time: DNA Strand Exchange by RecA. *Molecular Cell* **2008**, *30* (4), 530–538. https://doi.org/10.1016/j.molcel.2008.03.010.

(78) Forget, A. L.; Kowalczykowski, S. C. Single-Molecule Imaging of DNA Pairing by RecA Reveals a Three-Dimensional Homology Search. *Nature* **2012**, *482* (7385), 423–427. https://doi.org/10.1038/nature10782.

(79) van Gool, A. J.; Shah, R.; Mézard, C.; West, S. C. Functional Interactions between the Holliday Junction Resolvase and the Branch Migration Motor of Escherichia Coli. *EMBO J* **1998**, *17* (6), 1838–1845. https://doi.org/10.1093/emboj/17.6.1838.

(80) Benson, F. E.; Illing, G. T.; Sharples, G. J.; Lloyd, R. G. Nucleotide Sequencing of the Ruv Region of Escherichia Coli K-12 Reveals a LexA Regulated Operon Encoding Two Genes. *Nucleic Acids Res* **1988**, *16* (4), 1541–1549.

(81) Mitchell, A. H.; West, S. C. Hexameric Rings of Escherichia Coli RuvB Protein.: Cooperative Assembly, Processivity and ATPase Activity. *Journal of Molecular Biology* **1994**, *243* (2), 208–215. https://doi.org/10.1006/jmbi.1994.1648.

(82) Sha, R.; Liu, F.; Iwasaki, H.; Seeman, N. C. Parallel Symmetric Immobile DNA Junctions as Substrates for E. Coli RuvC Holliday Junction Resolvase. *Biochemistry* **2002**, *41* (36), 10985–10993. https://doi.org/10.1021/bi020319r.

(83) Bennett, R. J.; Dunderdale, H. J.; West, S. C. Resolution of Holliday Junctions by RuvC Resolvase: Cleavage Specificity and DNA Distortion. *Cell* **1993**, *74* (6), 1021–1031. https://doi.org/10.1016/0092-8674(93)90724-5.

(84) Shida, T.; Iwasaki, H.; Saito, A.; Kyogoku, Y.; Shinagawa, H. Analysis of Substrate Specificity of the RuvC Holliday Junction Resolvase with Synthetic Holliday Junctions *. *Journal of Biological Chemistry* **1996**, *271* (42), 26105–26109. https://doi.org/10.1074/jbc.271.42.26105.

(85) Swaminathan, R. Magnesium Metabolism and Its Disorders. *Clin Biochem Rev* **2003**, *24* (2), 47–66.

(86) Iwasaki, H.; Takahagi, M.; Nakata, A.; Shinagawa, H. Escherichia Coli RuvA and RuvB Proteins Specifically Interact with Holliday Junctions and Promote Branch

Migration. *Genes Dev.* **1992**, *6* (11), 2214–2220.
https://doi.org/10.1101/gad.6.11.2214.

(87) Nishino, T.; Iwasaki, H.; Kataoka, M.; Ariyoshi, M.; Fujita, T.; Shinagawa, H.; Morikawa, K. Modulation of RuvB Function by the Mobile Domain III of the Holliday Junction Recognition Protein RuvA11Edited by T. Richmond. *Journal of Molecular Biology* **2000**, *298* (3), 407–416. https://doi.org/10.1006/jmbi.2000.3675.

(88) Rafferty, J. B.; Sedelnikova, S. E.; Hargreaves, D.; Artymiuk, P. J.; Baker, P. J.; Sharples, G. J.; Mahdi, A. A.; Lloyd, R. G.; Rice, D. W. Crystal Structure of DNA Recombination Protein RuvA and a Model for Its Binding to the Holliday Junction. *Science* **1996**, *274* (5286), 415–421. https://doi.org/10.1126/science.274.5286.415.

(89) Dasari, S.; Tchounwou, P. B. Cisplatin in Cancer Therapy: Molecular Mechanisms of Action. *Eur J Pharmacol* **2014**, *740*, 364–378.
https://doi.org/10.1016/j.ejphar.2014.07.025.

(90) Mantri, Y.; Lippard, S. J.; Baik, M.-H. Bifunctional Binding of Cisplatin to DNA: Why Does Cisplatin Form 1,2-Intrastrand Cross-Links with AG, But Not with GA? *J Am Chem Soc* **2007**, *129* (16), 5023–5030. https://doi.org/10.1021/ja067631z.

(91) Wang, D.; Lippard, S. J. Cellular Processing of Platinum Anticancer Drugs. *Nat Rev Drug Discov* **2005**, *4* (4), 307–320. https://doi.org/10.1038/nrd1691.

(92) Rixe, O.; Ortuzar, W.; Alvarez, M.; Parker, R.; Reed, E.; Paull, K.; Fojo, T. Oxaliplatin, Tetraplatin, Cisplatin, and Carboplatin: Spectrum of Activity in Drug-Resistant Cell Lines and in the Cell Lines of the National Cancer Institute's Anticancer Drug Screen Panel. *Biochem Pharmacol* **1996**, *52* (12), 1855–1865.
https://doi.org/10.1016/s0006-2952(97)81490-6.

(93) Smith, I. E.; Talbot, D. C. Cisplatin and Its Analogues in the Treatment of Advanced Breast Cancer: A Review. *Br J Cancer* **1992**, *65* (6), 787–793.

(94) Fu, J.; Yang, Y. R.; Johnson-Buck, A.; Liu, M.; Liu, Y.; Walter, N. G.; Woodbury, N.; Yan, H. Multi-Enzyme Complexes on DNA Scaffolds Capable of Substrate Channelling with an Artificial Swinging Arm. *Nature nanotechnology* **2014**, *9* (7), 531–536. https://doi.org/10.1038/nnano.2014.100.

(95) Ingleston, S. M.; Dickman, M. J.; Grasby, J. A.; Hornby, D. P.; Sharples, G. J.; Lloyd, R. G. Holliday Junction Binding and Processing by the RuvA Protein of Mycoplasma Pneumoniae. *European Journal of Biochemistry 269* (5), 1525–1533.
https://doi.org/10.1046/j.1432-1033.2002.02805.x.

(96) Gibson, M. D.; Brehove, M.; Luo, Y.; North, J.; Poirier, M. G. Methods for Investigating DNA Accessibility with Single Nucleosomes. *Methods Enzymol* **2016**, *581*, 379–415. https://doi.org/10.1016/bs.mie.2016.08.014.

(97) Abelson, J.; Blanco, M.; Ditzler, M. A.; Fuller, F.; Aravamudhan, P.; Wood, M.; Villa, T.; Ryan, D. E.; Pleiss, J. A.; Maeder, C.; Guthrie, C.; Walter, N. G. Conformational Dynamics of Single Pre–MRNA Molecules during in Vitro Splicing. *Nat Struct Mol Biol* **2010**, *17* (4), 504–512. https://doi.org/10.1038/nsmb.1767.

(98) Eichman, B. F.; Vargason, J. M.; Mooers, B. H.; Ho, P. S. The Holliday Junction in an Inverted Repeat DNA Sequence: Sequence Effects on the Structure of Four-Way Junctions. *Proc Natl Acad Sci U S A* **2000**, *97* (8), 3971–3976.
https://doi.org/10.1073/pnas.97.8.3971.

(99) Nguyen, N.; Birktoft, J. J.; Sha, R.; Wang, T.; Zheng, J.; Constantinou, P. E.; Ginell, S. L.; Chen, Y.; Mao, C.; Seeman, N. C. The Absence of Tertiary Interactions in a

Self-Assembled DNA Crystal Structure. *J Mol Recognit* **2012**, *25* (4), 234–237. https://doi.org/10.1002/jmr.2183.

(100) Jahnen-Dechent, W.; Ketteler, M. Magnesium Basics. *Clinical Kidney Journal* **2012**, *5* (Suppl_1), i3–i14. https://doi.org/10.1093/ndtplus/sfr163.

(101) Hambley, T. W. Platinum Binding to DNA: Structural Controls and Consequences. *J. Chem. Soc., Dalton Trans.* **2001**, No. 19, 2711–2718. https://doi.org/10.1039/B105406F.

(102) *Platinum Coordination Complexes in Cancer Chemotherapy: Proceedings of the Fourth International Symposium on Platinum Coordination Complexes in Cancer Chemotherapy Convened in Burlington, Vermont by the Vermont Regional Cancer Center and the Norris Cotton Cancer Center, June 22–24, 1983*; Hacker, M., Douple, E. B., Krakoff, I. H., Eds.; Developments in Oncology; Springer US, 1984. https://doi.org/10.1007/978-1-4613-2837-7.

(103) Sancho-Martínez, S. M.; Piedrafita, F. J.; Cannata-Andía, J. B.; López-Novoa, J. M.; López-Hernández, F. J. Necrotic Concentrations of Cisplatin Activate the Apoptotic Machinery but Inhibit Effector Caspases and Interfere with the Execution of Apoptosis. *Toxicol Sci* **2011**, *122* (1), 73–85. https://doi.org/10.1093/toxsci/kfr098.

(104) Rn, B.; L, M.; Rj, M.; L, Y.; S, G.; Ws, G.; H, H.; T, S. Non-DNA-Binding Platinum Anticancer Agents: Cytotoxic Activities of Platinum-Phosphato Complexes towards Human Ovarian Cancer Cells. *Proc Natl Acad Sci U S A* **2008**, *105* (47), 18314–18319. https://doi.org/10.1073/pnas.0803094105.

(105) Bolivar, F.; Rodriguez, R. L.; Greene, P. J.; Betlach, M. C.; Heyneker, H. L.; Boyer, H. W.; Crosa, J. H.; Falkow, S. Construction and Characterization of New Cloning Vehicles. II. A Multipurpose Cloning System. *Gene* **1977**, *2* (2), 95–113.

(106) Watson, N. A New Revision of the Sequence of Plasmid PBR322. *Gene* **1988**, *70* (2), 399–403. https://doi.org/10.1016/0378-1119(88)90212-0.

(107) Kasparkova, J.; Fojta, M.; Farrell, N.; Brabec, V. Differential Recognition by the Tumor Suppressor Protein P53 of DNA Modified by the Novel Antitumor Trinuclear Platinum Drug BBR3464 and Cisplatin. *Nucleic Acids Res* **2004**, *32* (18), 5546–5552. https://doi.org/10.1093/nar/gkh896.

(108) Gümüş, F.; Eren, G.; Açık, L.; Çelebi, A.; Öztürk, F.; Yılmaz, Ş.; Sağkan, R. I.; Gür, S.; Özkul, A.; Elmalı, A.; Elerman, Y. Synthesis, Cytotoxicity, and DNA Interactions of New Cisplatin Analogues Containing Substituted Benzimidazole Ligands. *J. Med. Chem.* **2009**, *52* (5), 1345–1357. https://doi.org/10.1021/jm8000983.

(109) Wright, W. D.; Shah, S. S.; Heyer, W.-D. Homologous Recombination and the Repair of DNA Double-Strand Breaks. *J. Biol. Chem.* **2018**, *293* (27), 10524–10535. https://doi.org/10.1074/jbc.TM118.000372.

(110) Maizels, N.; Davis, L. Initiation of Homologous Recombination at DNA Nicks. *Nucleic Acids Res* **2018**, *46* (14), 6962–6973. https://doi.org/10.1093/nar/gky588.

(111) Amit, R.; Gileadi, O.; Stavans, J. Direct Observation of RuvAB-Catalyzed Branch Migration of Single Holliday Junctions. *PNAS* **2004**, *101* (32), 11605–11610. https://doi.org/10.1073/pnas.0404332101.

(112) Duckett, D. R.; Murchie, A. I. H.; Diekmann, S.; von Kitzing, E.; Kemper, B.; Lilley, D. M. J. The Structure of the Holliday Junction, and Its Resolution. *Cell* **1988**, *55* (1), 79–89. https://doi.org/10.1016/0092-8674(88)90011-6.

(113) Smith, G. R. RecBCD Enzyme and Pathway. In *Brenner's Encyclopedia of Genetics (Second Edition)*; Maloy, S., Hughes, K., Eds.; Academic Press: San Diego, 2013; pp 56–62. https://doi.org/10.1016/B978-0-12-374984-0.01264-X.

(114) Liu, B.; Baskin, R. J.; Kowalczykowski, S. C. DNA Unwinding Heterogeneity by RecBCD Results from Static Molecules Able to Equilibrate. *Nature* **2013**, *500* (7463), 482–485. https://doi.org/10.1038/nature12333.

(115) Singleton, M. R.; Dillingham, M. S.; Gaudier, M.; Kowalczykowski, S. C.; Wigley, D. B. Crystal Structure of RecBCD Enzyme Reveals a Machine for Processing DNA Breaks. *Nature* **2004**, *432* (7014), 187–193. https://doi.org/10.1038/nature02988.

(116) Ariyoshi, M.; Vassylyev, D. G.; Iwasaki, H.; Nakamura, H.; Shinagawa, H.; Morikawa, K. Atomic Structure of the RuvC Resolvase: A Holliday Junction-Specific Endonuclease from E. Coli. *Cell* **1994**, *78*, 1063–1072. https://doi.org/10.2210/pdb1hjr/pdb.

(117) van Gool, A. J.; Hajibagheri, N. M. A.; Stasiak, A.; West, S. C. Assembly of the Escherichia Coli RuvABC Resolvasome Directs the Orientation of Holliday Junction Resolution. *Genes Dev* **1999**, *13* (14), 1861–1870.

(118) Hohng, S.; Zhou, R.; Nahas, M. K.; Yu, J.; Schulten, K.; Lilley, D. M. J.; Ha, T. Fluorescence-Force Spectroscopy Maps Two-Dimensional Reaction Landscape of the Holliday Junction. *Science* **2007**, *318* (5848), 279–283. https://doi.org/10.1126/science.1146113.

(119) Yu, J.; Ha, T.; Schulten, K. Conformational Model of the Holliday Junction Transition Deduced from Molecular Dynamics Simulations. *Nucleic Acids Res* **2004**, *32* (22), 6683–6695. https://doi.org/10.1093/nar/gkh1006.

(120) Mandal, S.; Selvam, S.; Cui, Y.; Hoque, M. E.; Mao, H. Mechanical Cooperativity in DNA Cruciform Structures. *ChemPhysChem* **2018**, *19* (20), 2627–2634. https://doi.org/10.1002/cphc.201800480.

(121) Gál, J.; Kálmán, M. Autosticky PCR. In *PCR Cloning Protocols*; Chen, B.-Y., Janes, H. W., Eds.; Methods in Molecular Biology™; Humana Press: Totowa, NJ, 2002; pp 141–151. https://doi.org/10.1385/1-59259-177-9:141.

(122) Yang, L.; Zhong, Z.; Tong, C.; Jia, H.; Liu, Y.; Chen, G. Single-Molecule Mechanical Folding and Unfolding of RNA Hairpins: Effects of Single A-U to A·C Pair Substitutions and Single Proton Binding and Implications for MRNA Structure-Induced −1 Ribosomal Frameshifting. *Journal of the American Chemical Society* **2018**. https://doi.org/10.1021/jacs.8b02970.

(123) Hyeon, C.; Thirumalai, D. Mechanical Unfolding of RNA: From Hairpins to Structures with Internal Multiloops. *Biophysical Journal* **2007**, *92* (3), 731–743. https://doi.org/10.1529/biophysj.106.093062.

(124) Dame, R. T.; Hall, M. A.; Wang, M. D. Single-Molecule Unzipping Force Analysis of HU-DNA Complexes. *ChemBioChem* **2013**, *14* (15), 1954–1957. https://doi.org/10.1002/cbic.201300413.

(125) Hall, M. A.; Shundrovsky, A.; Bai, L.; Fulbright, R. M.; Lis, J. T.; Wang, M. D. High-Resolution Dynamic Mapping of Histone-DNA Interactions in a Nucleosome. *Nat Struct Mol Biol* **2009**, *16* (2), 124–129. https://doi.org/10.1038/nsmb.1526.

(126) Wenner, J. R.; Williams, M. C.; Rouzina, I.; Bloomfield, V. A. Salt Dependence of the Elasticity and Overstretching Transition of Single DNA Molecules. *Biophysical Journal* **2002**, *82* (6), 3160–3169. https://doi.org/10.1016/S0006-3495(02)75658-0.

(127) Chaurasiya, K. R.; Paramanathan, T.; McCauley, M. J.; Williams, M. C. Biophysical Characterization of DNA Binding from Single Molecule Force Measurements. *Phys Life Rev* **2010**, *7* (3), 299–341. https://doi.org/10.1016/j.plrev.2010.06.001.

(128) Wen, J.-D.; Manosas, M.; Li, P. T. X.; Smith, S. B.; Bustamante, C.; Ritort, F.; Tinoco, I. Force Unfolding Kinetics of RNA Using Optical Tweezers. I. Effects of Experimental Variables on Measured Results. *Biophys J* **2007**, *92* (9), 2996–3009. https://doi.org/10.1529/biophysj.106.094052.

(129) Ingleston, S. M.; Sharples, G. J.; Lloyd, R. G. The Acidic Pin of RuvA Modulates Holliday Junction Binding and Processing by the RuvABC Resolvasome. *EMBO J.* **2000**, *19* (22), 6266–6274. https://doi.org/10.1093/emboj/19.22.6266.

(130) Bolt, E. L.; Sharples, G. J.; Lloyd, R. G. Analysis of Conserved Basic Residues Associated with DNA Binding (Arg69) and Catalysis (Lys76) by the RusA Holliday Junction Resolvase11Edited by J. Karn. *Journal of Molecular Biology* **2000**, *304* (2), 165–176. https://doi.org/10.1006/jmbi.2000.4196.

(131) Yamada, K.; Ariyoshi, M.; Morikawa, K. Three-Dimensional Structural Views of Branch Migration and Resolution in DNA Homologous Recombination. *Current Opinion in Structural Biology* **2004**, *14* (2), 130–137. https://doi.org/10.1016/j.sbi.2004.03.005.

(132) Yu, Z.; Koirala, D.; Cui, Y.; Easterling, L. F.; Zhao, Y.; Mao, H. Click Chemistry Assisted Single-Molecule Fingerprinting Reveals a 3D Biomolecular Folding Funnel. *J. Am. Chem. Soc.* **2012**, *134* (30), 12338–12341. https://doi.org/10.1021/ja303218s.

(133) Dhakal, S.; Cui, Y.; Koirala, D.; Ghimire, C.; Kushwaha, S.; Yu, Z.; Yangyuoru, P. M.; Mao, H. Structural and Mechanical Properties of Individual Human Telomeric G-Quadruplexes in Molecularly Crowded Solutions. *Nucleic Acids Res* **2013**, *41* (6), 3915–3923. https://doi.org/10.1093/nar/gkt038.

(134) Baumann, C. G.; Smith, S. B.; Bloomfield, V. A.; Bustamante, C. Ionic Effects on the Elasticity of Single DNA Molecules. *PNAS* **1997**, *94* (12), 6185–6190. https://doi.org/10.1073/pnas.94.12.6185.

(135) Bao, L.; Zhang, X.; Jin, L.; Tan, Z.-J. Flexibility of Nucleic Acids: From DNA to RNA. *Chinese Phys. B* **2016**, *25* (1), 018703. https://doi.org/10.1088/1674-1056/25/1/018703.

(136) Cui, Y.; Tang, Y.; Liang, M.; Ji, Q.; Zeng, Y.; Chen, H.; Lan, J.; Jin, P.; Wang, L.; Song, G.; Lou, J. Direct Observation of the Formation of a CRISPR–Cas12a R-Loop Complex at the Single-Molecule Level. *Chem. Commun.* **2020**, *56* (14), 2123–2126. https://doi.org/10.1039/C9CC08325A.

(137) Tinoco, I.; Li, P. T. X.; Bustamante, C. Determination of Thermodynamics and Kinetics of RNA Reactions by Force. *Quarterly Reviews of Biophysics* **2006**, *39* (4), 325–360. https://doi.org/10.1017/S0033583506004446.

(138) Liphardt, J. Reversible Unfolding of Single RNA Molecules by Mechanical Force. *Science* **2001**, *292* (5517), 733–737. https://doi.org/10.1126/science.1058498.

(139) Tinoco, I. Force as a Useful Variable in Reactions: Unfolding RNA. *Annu Rev Biophys Biomol Struct* **2004**, *33*, 363–385. https://doi.org/10.1146/annurev.biophys.33.110502.140418.

(140) Oligo synthesis: Why IDT leads the oligo industry https://www.idtdna.com/pages/education/decoded/article/oligo-synthesis-why-idt-leads-the-oligo-industry (accessed Nov 7, 2018).

(141) Gibbs, D. R.; Kaur, A.; Megalathan, A.; Sapkota, K.; Dhakal, S. Build Your Own Microscope: Step-By-Step Guide for Building a Prism-Based TIRF Microscope. *Methods and Protocols* **2018**, *1* (4), 40. https://doi.org/10.3390/mps1040040.

Curriculum Vitae

Dalton R. Gibbs

(804)691-5948 · daltonrgibbs@gmail.com · 3505 Festival Park Plaza, #206, Chester, VA 23831

Education

Virginia Commonwealth University, Richmond, VA
Ph.D. in Chemistry
May 2021(Expected)

James Madison University, Harrisonburg, VA
B.S. in Chemistry with a minor in Biology
May 2016

Awards

Distinguished Chemist Fund, 2020-2021 academic year

Altria Fellowship, 2019-2020 academic year

Peer-Reviewed Publications

- **Gibbs, D. R.**, Mahmoud, R., Kaur, A. & Dhakal, S. Direct unfolding of RuvA-HJ complex at the single-molecule level. *Biophysical Journal,* In Press (2021)
- **Gibbs, D. R.** & Dhakal, S. Homologous Recombination under the Single-Molecule Fluorescence Microscope. *Int. J. Mol. Sci.,* 20 (23), 6102. (2019)
- **Gibbs, D. R.**, Kaur, A., Megalathan, A., Sapkota, K. & Dhakal, S. Build Your Own Microscope: Step-By-Step Guide for Building a Prism-Based TIRF Microscope. *Methods & Protoc.* 1, 40 (2018).
- **Gibbs, D. R.** & Dhakal, S. Single-Molecule Imaging Reveals Conformational Manipulation of Holliday Junction DNA by the Junction Processing Protein RuvA. *Biochemistry* 57, 3616–3624 (2018).
- Oweis, W., Padala,P., Hassouna, F., Cohen-Kfir, E., **Gibbs, D. R.,** Todd, E. A., Berndsen, C. E., Wiener, R. Trans -Binding Mechanism of Ubiquitin-like Protein Activation Revealed by a UBA5-UFM1 Complex. *Cell Reports* 16, 3113–3120 (2016).

Conference Presentations

- "Probing the interaction between protein and Holliday junction DNA at the molecular level"- ACS National Meeting 2020 (Selected for oral presentation).
- "Probing the Binding Activity of Holliday Junction Resolvases."-11/9/2019, 6th Annual Chesapeake Bay Area Single Molecule Biology Meeting.
- "Single molecule investigation of the behavior of Holliday junction processing proteins"-3/20/2019, Pittcon Conference 2019.
- "Single-molecule Investigation of Holliday Junction Binding Proteins" -9/22/2018, soundbite, Virginia Soft Matter Workshop 2018.
- "An Investigation of Holliday Junction DNA in Complex with Junction Processing Protein RuvA" - 5/18/2017, poster, Annual meeting of the Virginia Academy of Science 2017.

Research Experience

Graduate Research Assistant, VCU Dept. of Chemistry, PI: Soma Dhakal   2016-Present

- Designed and carried out single molecule florescence microscopy experiments to probe protein-DNA interactions.
- Executed single molecule force measurements on proteins, DNA, and RNA using optical tweezers.
- Supervised lab purchasing, safety, and waste disposal.
- Built and maintained single molecule TIRF microscope.
- Developed long term research plans and executed these plans while supervising undergraduate researchers.

Undergraduate Researcher, JMU Dept. of Chemistry, PI: Christopher Berndsen   2013-2016

- Expressed, purified, and quantified enzymes, conducted assays and other analyses of enzyme activity.
- Modeled enzyme systems in programs such as YASARA.
- Preformed and Interpreted comparative 2D NMR spectroscopy on mutated enzymes.

Professional Experience

Teaching Assistant, VCU Dept. of Chemistry   2016-Present

- Supervised safety and compliance for 30+ General Chemistry Labs.
- Taught short lessons in general chemistry and led students in group work.

Peer Tutor, JMU Learning Centers: Science & Math Learning Center   2013-2016

- Tutored students in general and organic chemistry in a drop-in environment.
- Facilitated remedial education and review of chemistry basics.